DOCTOR OF PHILOSOPHY

The plasmonics of a nanosphere on a mirror substrate

Katzen, Joel

Award date:
2019

Awarding institution:
Queen's University Belfast

The plasmonics of a nanosphere on a mirror substrate

Thesis submitted for the degree of

Doctor of Philosophy (PhD)

in the

Centre for Nanostructured Media

by

Joel Michael Katzen MSci

School of Mathematics and Physics

Queen's University Belfast

July 2018

Acknowledgements

I offer my sincere gratitude to my supervisor Dr. Fumin Huang, for his guidance, advice, and patience during my time as his student. Thank you also to past and present members of his group, who have given great assistance in sample fabrication and simulation, as well as being great friends through the good times and the bad. These include Dr. Matěj Velický, Dr. Stacey Drakeley, Gavin Donnelly, Mugahid Ali and Yuefeng Huang. Special mention also goes to Mike Hardy. Although not a member of our group, he gave great support when it came to learning new techniques and invaluable advice during my time at QUB, and I will always be grateful to him for his friendship.

I am also grateful to those who have collaborated with me during my studentship, namely Dr. Elton Santos and his group in QUB, Dr. Lu Hua Li and his group in Deakin University, and Dr. Christos Tserkezis in the University of Southern Denmark. Thanks also to my examiners: Dr. Amit Kumar and Professor David Richards.

I thank my family, who have provided support, as well as feedback for my work and prior to my exam. I also acknowledge my friends, especially those in Belfast's theatre and comedy scene, who have given me the opportunity to have a fantastic creative outlet, and my fellow volunteers in the charity shop where I work.

Finally, I would like to thank the department of employment and learning (DEL) of Northern Ireland, as well as the Institute of Physics who provided funds during my studentship.

"All that glisters is not gold…"

William Shakespeare – The Merchant of Venice

Abstract

The aim of this thesis is to systematically investigate the physics of coupling a spherical gold nanoparticle on a mirrored (NPoM) substrate. When this occurs, both the localised surface plasmons on the particle and propagating surface plasmons at both of the interfaces of the substrate can be excited. The reflectivity and permittivity of the substrate plays a key role in the plasmonics of a NPoM. As reflectivity increases, a vertical dipole plasmon modes develops, while increasingly negative permittivities give rise to surface plasmons in the film, which are sensitive to film thickness and hybridise with the particle's plasmons, causing them to shift. Furthermore, since much of the charge in a vertically polarised particle is localised to the gap region, large amounts of opposite charges are induced on the opposite side of the gap. This is vital in the implementation of NPoM in strong coupling between plasmons in the nanoparticle and excitons in carbon molecules inside the gap created by using single layer graphene as a spacing layer. This thesis demonstrates that optical spectroscopy is an effective method for characterising single layers of graphene. This is confirmed by comparing the experimental results to a theoretical method, which takes into account contributions from a wide range of incident angles and both TE and TM polarisations.

It is also shown that coupling strength can be collectively tuned within the visible spectrum using a low-powered incident laser. This works by photobleaching carbon molecules in the gap (grown under the influence of the intense gap mode in the NPoM) and reducing its oscillating strength. This is confirmed both experimentally and theoretically, and may help with the development of new optoelectronic and molecular devices.

List of figures

Figure 2.1 Diagram showing the collective oscillation of electrons on a metal nanoparticle's surface……..21

Figure 2.2 Diagram showing the parameters considered for the quasistatic approximation for a homogeneous particle in an electric field whose field lines are horizontally polarised …….. 22

Figure 2.3 (Blue) Real and (red) imaginary parts of the permittivity of gold according to the Drude free electron model …… 26

Figure 2.4 Extinction and the corresponding electron microscope images for silver nanoparticles of diameter (a) 46, (b) 59, (c) 86, (d) 128, (e) 160, (f) 194, and (g) 287 nm in water……...27

Figure 2.5 Optical responses calculated for silver (a) nanospheres, (b) nanocubes, (c) nanotriangles, and (d) nanobars in water. (Red) absorption, (blue) scattering, and (black) extinction spectra were calculated using (a) Mie theory and (b-d) the discrete dipole approximation. Note that the illumination angle was not provided in the original paper ……..28

Figure 2.6 Schematic diagram illustrating the plasmonic coupling between charges in two nanoparticles, forming a dimer geometry……..29

Figure 2.7 Graphs showing how the plasmonic resonance of a gold nanodisc dimer system changes with interparticle distance for (a) experiments and (b) DDA simulations…… 30

Figure 2.8 Diagram of the nanoparticle on mirror geometry……..32

Figure 2.9 Diagrams demonstrating plasmonic modes formed from a plasmonic particle inducing (a) horizontal and (b) vertical image dipoles in the substrate. When the particle is near the substrate, its horizontal dipole

decreases due to destructive interference with its image dipole, while the vertical mode increases due to constructive interference with its image dipole. Black arrows indicate the orientation of the dipole …….33

Figure 2.10 Dark-field images of Au NPs on (a) a thin Au film, (b) a Si wafer, and (c) a quartz wafer……..34

Figure 2.11 Diagram showing charges and induced charges around the NPoM's gap region forming strong plasmons (blue line). The red arrow indicates the orientation of the gap's dipole ……35

Figure 2.12 Schematic of the (a) bonding and (b) anti-bonding film plasmons……...36

Figure 2.13 Diagram showing the charge distributions for the (a) localised and (b) virtual modes. Through Coulombic interactions, the particle's plasmons align only with short wavelength film plasmons (shown in black), while the virtual mode arises from charges in the particle's near field align only with bonding film plasmons with wavelength greater than twice the particle's diameter (shown in blue)……37

Figure 2.14 Scattering spectra from individual NPoMs where the MB molecules are aligned (top) perpendicular and (bottom) parallel to the gap plasmon…….39

Figure 2.15 Scattering spectra for plexcitonic gold dimer J-aggregate nanostructures with nanodisks ranging in diameter from 60 to 115 nm measured for (a) longitudinal and (e) transverse polarisations. The corresponding calculated spectra are shown for (b) longitudinal and (e) transverse polarisations. The light blue line indicates the excitonic resonance of the molecule. Near-field enhancement maps calculated at the exciton resonance are shown for (c) longitudinal and (d) transverse polarisations…..40

Figure 2.16 Coupling between plasmons and excitons illustrated by mechanical oscillators……. 41

Figure 2.17 Eigenfrequencies of (a) uncoupled and (b) coupled oscillators…42

Figure 3.1 Diagram showing how magnetron sputtering works. Argon ions bombard the gold target and the resulting atoms form a thin film on the substrate……51

Figure 3.2 Diagram showing how x-rays are reflected and refracted when interacting with a stack of thin films ……52

Figure 3.3 XRR spectrum of a 50 nm Au film sputtered onto a bulk silicon substrate prepared for this thesis …….....53

Figure 3.4 TEM image of ultrasmooth, spherical 90 nm Au NP on a carbon grid at 97000x……54

Figure 3.5 Diagram demonstrating the process of dark-field microscopy……55

Figure 3.6 (a) Scattering spectra from five 90 nm Au NPs on 100 nm Au. (b) Optical dark-field image of 90 nm Au NPs on 100 nm. Particles measured are circled in the corresponding colours from (a). Scale bar represents 2 μm ……56

Figure 3.7 Raman spectrum measured from a suspended monolayer graphene measured with a 532 nm laser…….58

Figure 3.8 (a) First order G-band process and (b) two phonon second order for the double resonance 2D-band process. Resonance points are shown with open circles……... 59

Figure 3.9 Raman spectra for graphene of 1-4 layers on bulk gold substrates taken with a 532 nm laser of 0.8 mW power …….....60

Figure 3.10 Diagram showing the vibrations of the (a) E_{2g}^{1} and (b) A_{1g} Raman modes……61

Figure 3.11 Raman spectra of MoS_2 flakes of thickness 1-4 layers, as well as bulk. Data has been offset for clarity……..62

Figure 3.12 top: diagram showing the incident aperture of the objective lens (top view); bottom: schematic showing the focusing cone of light. The correspondence between the incident annular ring and the focusing cone is indicated by filled grey areas……..63

Figure 3.13 Contrast spectra for graphene sheets of different thicknesses, along with corresponding optical images. Samples a-f are more than 10 layers in thickness, with the thickness increasing from a to f…….66

Figure 4.1 Optical dark-field images of 90 nm Au NPs on Au films of thickness ranging from 0 to 100 nm on 93 nm SiO2/10 nm Ti/bulk Si substrates. Images were taken with a 100× magnification objective (NA=0.9). Scale bar represents 0.8 μm ….....73

Figure 4.2 (a) Scattering spectra measured for 90 nm Au particles on Au films of thickness 0, 4.3, 6.9, 9.4, 11.8, 14.9, 26.4 and 100 nm on SiO2. Measured data is given in red, while Lorentzian fitted data is given in black. (b) Graph showing how the (orange) transverse, (green) vertical, and (red) gap modes change with Au film thickness ……...74

Figure 4.3 Graph showing how the intensities of the (orange) transverse, (green) virtual, and (red) gap modes changes with Au film thickness……..77

Figure 4.4 Optical dark-field images of Au NPs on Au film of thickness ranging from 0 to 100 nm on Si substrates. Scale bar represents 0.8 μm……79

Figure 4.5 (a) Scattering spectra measured from 90 nm Au particles on Au films of 0, 5, 10, 20, 30, 40, 50 and 100 nm on Si. (b) Graph showing how the (orange) transverse, (green) virtual, and (red) gap modes change with increasing Au film thickness……...80

Figure 4.6 Colour quantum efficiency for an Infinity 2 CCD camera……81

Figure 4.7 Graphs showing how the absolute scattering intensities of the (orange) transverse, (green) virtual, (red) and gap modes changes with Au film thickness on a Si substrate……...82

Figure 4.8 Scattering spectrum of a 90 nm Au NP on a bare silicon substrate. Black line represents the Lorentzian fit……83

Figure 5.1 (a) Measured SERS spectra from Au nanoparticles on Au films with various Ta2O5 spacing layers ranging in thickness from 0-10 nm. (b) The peak intensities of the (red circles) D-peak and (blue circles) G-peaks as a function of the gap distance, and (green triangles) the simulated SERS enhancements within the gaps of an analogue dimer system ……..94

Figure 5.2 (a) Measured SERS spectra of 4-ATP molecules adsorbed on 150 nm Au particles on Au films with various thickness of Ta2O5 spacing layers. (b) The intensities of the 1085 cm-1 Raman peaks as a function of the gap distance. Inset: the fitted Lorentzian peaks of the 1085 cm-1 4-ATP Raman modes …...96

Figure 5.3 Calculated electric field enhancement distribution of a Au dimer system (150 nm in diameter, separated by a 1 nm air gap). The field is highly concentrated within the gap. A plane wave of 633 nm is incident along the direction indicated by the red arrow. The polarization of light is indicated by the double arrow. (b) Calculated SERS enhancement spectrum for the dimer system (red line) and the measured optical scattering spectrum of individual Au particles (150 nm) on Au films separated by 1 nm Ta_2O_5 film (blue line).....98

Figure 5.4 Experimental SERS spectra measured from 150 nm Au particles on Au films with various thicknesses of Ta_2O_5 spacing layers taken with a 594 nm laser. (b) Intensities of the (red) D-peak and (blue) G-peaks as a function of the gap distance …….....100

Figure 6.1 (a-b) Bright-field images of 1-5 layered graphene flakes without an optical filter, (c-d) with a 490 nm optical filter (10 nm bandwidth), and (e-f) grayscale images of (c-d). The contrast in (e) is enhanced by two times for a better view of the monolayer film. The inset of the 3L film was taken at a different location on the sample and superimposed here. Red dashed circles represent locations from where reflection measurements were taken ……...109

Figure 6.2 Calculated optical contrast and reflectivity of monolayer graphene on 100 nm Au, as functions of the incident angle and wavelength of light. (a-b) Reflectance, (c-d) contrast. The left and right panels are for TE- and TM-polarisations, respectively, presented with the same colour scale. Refractive index of graphene nG = 2.6-1.3i; thickness 0.335 nm ……110

Figure 6.3 (a) Measured (red) and simulated (blue) contrast spectra taken from 1-5 layers of clean graphene. (b) Graph showing how the maximum contrast changes with the number of layers ……..112

Figure 6.4 (a) AFM images and (b) smoothed step profiles of graphene flakes shown in figure 6.1. Height profiles are averaged within the boxes marked in the AFM images. Arrows indicate the directions of the height profiles. All scale bars correspond to 1 μm. (c) Raman spectra measured from 1-5 layers of graphene excited by a 532 nm laser. (d) Graph showing the ratio of the normalised intensity of the G and 2D peaks as a function of number of layers.....114

Figure 6.5 (a) Simulated contrast spectra of 0-2 nm (from bottom to top, 0.2 increment) amorphous carbon films adsorbed onto the graphene monolayer on a 100 nm bulk gold substrate. (b) Graph showing how the monolayer's contrast spectrum changes in peak wavelength and intensity as a function of the thickness of the amorphous carbon. The refractive index for amorphous carbon is taken from ref. 48 ……...116

Figure 6.6 (a) Measured maximum optical contrast of freshly prepared graphene flakes before and after they were exposed to ambient conditions for 2, 7 and 21 days. (b) Increments of the optical contrast of the optical contrast of graphene flakes after exposure to the air. Dashed lines are for guidance. Standard errors are presented ……..117

Figure 7.1 Tapping mode AFM images taken of graphene on bulk gold substrates. Images courtesy of Dr. Lu Hua Li's group in Deakin University, Australia ……128

Figure 7.2 (a) SERS measured from Au NPs on 1-4L graphene films on a bulk Au substrate. Spectra taken from 2-4L are multiplied by factors shown on the graph. Inset shows Raman intensity against number of layers plotted in the natural log scale for (red pentagons) D-peaks and (blue hexagons) G-peaks. (b) Successively measured from a Au NP on monolayer MoS_2 spacing layer. No Raman signals were detected on (red) the first measurement, but strong D-peaks and G-peaks appear in subsequent measurements (blue and black). Raman was measured with 633 nm laser of 0.93 mW ……...130

Figure 7.3 (a) Photoluminescence spectra measured from a Au NP on monolayer graphene excited at (red) 543 nm, (blue) 532 nm and (green) 594 nm. This demonstrates the wavelength dependent behaviour of the GQDs. Data has been normalised with respect to laser power and offset for clarity. Fitted data is shown in black. (b) Measured photoluminescence of the Au NP with the 543 nm laser composed of three emission modes (dashed lines) ….131

Figure 7.4 (a) Dark-field optical images of Au NPs on (red circle) monolayer graphene and (green square) on bare Au. Scale bar represents 2 μm. (b) Scattering spectra from Au NPs on 1-3L graphene. (c) Scattering spectra from Au NP on monolayer MoS_2. (d) Scattering spectra from various Au NPs on monolayer graphene ……132

Figure 7.5 (a) Scattering spectra from a Au NP on monolayer graphene, irradiated by a 532 nm laser (75 μW) for ten second intervals starting from 0 seconds at the bottom and 90 seconds at the top. (b) Dispersion diagram showing the dependence of the energy of the split peaks (ω+ and ω-) on the exciton energy. Filled symbols represent measured data from the NP in (a) and 7.4d, while the empty circles represent simulated data ……134

Figure 7.6 (a) Simulated near-field distribution inside the NPoM gap, excited by a 685 nm laser. The NP's shape is indicated by the white dashed line. (b) The profile of the enhancing field inside the nanogap. This is fitted with a Lorentzian profile (solid line). (c) Scattering spectra of NP on monolayer graphene as a function of exciton energy. The top spectrum represents no coupling (ωexc = 0) at the top, indicating a plasmonic mode of 1.82 eV (shown by the dashed line). Dashed lines represent the split peaks which result from strong coupling. The energies of the modes are shown in 7.5b. Courtesy of Dr. Tserkezis ……136

Figure 7.7 Scattering spectra of a NP on monolayer graphene measured (purple) before laser irradiation, (red) directly after, (orange) 1 hour, (yellow) 2 hours, (green) 28 hours, and (blue) 72 hours after laser irradiation …….137

Contents

Abstract……...…4

List of figures…….5

1. **Introduction…….. 16**

1.1 Prologue……....16

1.2 Structure of this thesis……... 17

1.3 References…… 19

2. **Background theory……....21**

2.1 Plasmonic theory…… 21

2.1.1 Localised surface plasmon resonance (LSPR)…... 21

2.1.2 Effect of particle size and shape on resonance…...27

2.1.3 Interparticle distance…….29

2.1.4 Nanoparticle on mirror geometry……31

2.2 Plexciton strong coupling…….. 38

2.3 References……42

3. Materials and techniques…….. 50

3.1 Introduction……. 50

3.2 Sample preparation and characterisation……... 50

3.2.1 Magnetron sputtering……... 50

3.2.2 X-ray reflectivity (XRR)…….51

3.3 Gold nanoparticle preparation……..53

3.4 Optical dark-field microscopy and spectroscopy…….. 55

3.5 2D material preparation and characterisation……56

3.5.1 Raman scattering……57

3.5.2 Optical contrast spectroscopy…….. 62

3.6 References……67

4. Tuning plasmonic response through optical properties of the substrate…….... 70

4.1 Introduction……. 70

4.2 Sample preparation……72

4.3 Results……...72

4.3.1 Silicon oxide substrate……..72

4.3.2 P-type boron-doped silicon substrate ……78

4.4 Conclusions……..84

4.5 References……85

5. Optimising SERS with precisely controlled nanometre-scale gaps…….... 90

5.1 Introduction……. 90

5.2 Materials and methods…….....92

5.3 Results and discussion……... 93

5.4 Conclusions……101

5.5 References……...102

6. Characterising graphene flakes on bulk gold through optical contrast spectroscopy.....106

6.1 Introduction……... 106

6.2 Sample characterisation……...108

6.3 Results and discussion……. 108

6.3.1 Optical contrast spectroscopy……...108

6.3.2 Raman and AFM characterisation…….113

6.3.3 Molecule adsorption detection……..115

6.4 Conclusions……119

6.5 References……...119

7. Tuning strong coupling of plexcitons at room temperature...125

7.1 Introduction……... 125

7.2 Experimental……. 127

7.2.1 Sample preparation……. 127

7.2.2 Photoluminescence……..128

7.3 Results…… 128

7.4 Conclusions……....138

7.5 References……...138

8. Conclusions and future prospects……..145

List of publications……148

Chapter 1

Introduction

1.1 Prologue

Nanotechnology is a field which actively plays a role in our daily lives, such as in electronics[1], materials[2], and medicine[3] through use of nanostructures.

One important aspect of nanotechnology is the interaction of incident radiation with nanoparticles made of noble metals, such as gold or silver. This causes collective oscillations of free electrons on their surface with frequencies in the visible range. These oscillations are called plasmons. This phenomenon has been seen throughout history even before the physics was understood, such as in stained glass windows, or in ancient artefacts like the Lycurgus cup.

The plasmonic resonance (and therefore the colour) of the nanoparticle is very sensitive to many different factors including the refractive index of its surrounding medium[4], the particle's size and shape[5,6], and the influence of other nearby particles[7]. By varying the separation from other particles, not only can the plasmonic resonance be tuned, but the strength of the electric field in the gap between the two nanoparticles can also be controlled. This is important because this electric field has an enhancing effect on incident radiation and the signal of any molecule inside the gap, and is therefore vital for processes such as surface-enhanced Raman spectroscopy (SERS)[8] and optical sensing[9].

The problem with investigating interparticle coupling is that it is difficult to bring two particles close together at a specific separation in a way that is accurate and repeatable. One method of overcoming this is to use the

nanoparticle-on-mirror (NPoM) geometry. This works by placing the nanoparticle on a reflective substrate, where instead of coupling to another particle, it couples to image charges induced in the film. Then, by depositing a dielectric spacing layer on top of the mirror, many nanoparticles with robust interparticle distances can be examined. Furthermore, if a 2D material such as graphene, hexagonal boron nitride (hBN), or molybdenum disulfide (MoS_2) is used as the spacing layer, subnanometre separations can be investigated, where phenomena such as quantum tunnelling and non-local effects can impact the plasmonic resonance.

The aim of this thesis is firstly to study the fundamentals of the coupling of a nanoparticle to its image in a reflective substrate. This is investigated through scattering spectra, whose resonant peaks are studied systematically in order to find their physical origin. This is important because the NPoM geometry is now used frequently, both in research projects and in practical applications[10-12]. By understanding its fundamentals, it can be fully exploited. This thesis also aims to show that the plasmonic and enhancing field of a NPoM can be precisely tuned so that its hotspot is intense enough that strong coupling can be achieved between plasmons in the particle and excitons in molecules inside the gap, thereby forming plexciton quasiparticles.

1.2 Structure of this thesis

This thesis is divided into two parts. In the first part, general information is given about the theory and methods used in these experiments. Details of the background theory of localised surface plasmonics, strong coupling and optical contrast spectroscopy are discussed in chapter 2, while details of the techniques to fabricate and characterise the samples are given in chapter 3.

In the second part, specific results from this thesis are examined. In chapter 4, gold nanoparticles are deposited onto gold films of different thicknesses, which in turn affect their optical properties. The scattered light is then collected and analysed. As the film thickness changes, different resonant modes are affected in different ways, which gives detailed information about what each of the modes represents; an important aspect if this method is to be used to characterise a nanoparticle's coupling with its substrate.

The plasmonic enhancement is then examined in chapter 5. Here, gold nanoparticles are drop cast onto bulk gold substrates with layers of dielectric tantalum pentoxide sputtered on top. These layers range in thickness from 0 to 10 nm. Particles are then probed with lasers to analyse their Raman spectroscopy. By changing the thickness of tantalum pentoxide, the interparticle distance between the particle and its image in the substrate is tuned, and information can be gained about the how this affects the enhancement of the NPoM gap mode. This is important because enhancement often plays a key role in applications from plasmonic technology.

Chapter 6 used contrast spectroscopy to identify the number of layers of graphene in a flake on a bulk gold substrate. This is achieved by measuring the reflected light from the flake and comparing it to that from the gold substrate. These results are then compared to simulations based on the Fresnel equations, taking into account contributions from every incident angle, as well as both TM and TE light polarisations. The results are also compared to the conventional characterising methods of graphene flakes, including AFM and Raman, which are not always accurate. Finally, it is demonstrated that contrast spectroscopy can detect atomic layers of contamination on the graphene flakes, which has important implications for electronic devices integrated with graphene flakes.

This also plays a role in chapter 7, where gold nanoparticles are drop-cast onto layers of graphene, to examine how angstrom changes in interparticle distance affect the plasmonic resonance. It is also demonstrated through scattering that enhancement inside the gap can be precisely tuned so that strong coupling between the plasmons in the particle and excitons in carbon molecules inside the nanogap can be achieved. Moreover, the coupling strength can be actively tuned within the visible region through laser irradiation of the carbon molecules. This is useful in designing new plexcitonic devices.

Finally, a conclusion of this work is presented and an outlook is discussed about how this study could be extended to look at other types of nanostructures.

1.3 References

1. Thukral et al., *Soft ultrathin silicon electronics for soft interfaces: a review of recent advances of soft neutral interfaces based on ultrathin silicon*, IEEE Nanotechnology Magazine 12, no. 1 (2018): 21-34
2. Wang et al., *Electrical control of charged carriers and excitons in atomically thin materials*, Nature Nanotechnology 13 (2018): 128-132
3. Mitri, Ingle & Rai, *Nanotechnology in the management of bone diseases and as regenerative medicine*, Current Nanoscience 14, no. 2 (2018): 95-103
4. Lu, Wan & Zhang, *Metal-dielectric-metal based narrow band absorber for sensing applications*, Optics Express 23, no. 23 (2015): 29842-29847
5. Amendola, Bakr & Stellacci, *A study of the surface plasmon resonance of silver nanoparticles by the discrete dipole approximation method: effect of shape, size, structure, and assembly*, Plasmonics 5, no. 1 (2010): 85-97

6. Lee & El-Sayed, *Gold and silver nanoparticles in sensing and imaging: sensitivity of plasmon response to size, shape, and metal composition*, The Journal of Physical Chemistry B 110, no. 39 (2006): 19220-19225
7. Whitney et al., *Localised surface plasmon resonance nanosensor: A high-resolution distance-dependence study using atomic layer deposition*, Journal of Physical Chemistry B 109, no. 43 (2005): 20522-20528
8. Hardy et al., *Detection of low-concentration contaminants in solution by exploiting chemical derivatization in surface-enhanced Raman spectroscopy*, Analytical Chemistry 86, no. 18 (2014): 9006-9012
9. Thongrattanasiri & de Abajo, *Optical field enhancement by strong plasmon interaction in graphene nanostructures*, Physical Review Letters 110, no. 18 (2013): 187401
10. Cormier, Ding, Turek & Baumberg, *Actuating single nano-oscillators with light*, Advanced Optical Materials 6, no. 6 (2018): 1701281
11. Sigle et al., *Ultrathin CdSe in plasmonic nanogaps for enhanced photocatalytic water splitting*, The Journal of Physical Chemistry Letters 6, no. 7 (2015): 1099-1103
12. Wirth et al., *Tuning of spectral and angular distribution of scattering from single gold nanoparticles by subwavelength interference layers*, Nano Letters 14, no. 2 (2014): 570-577

Chapter 2

Background Theory

2.1 Plasmonic theory

2.1.1 Localised surface plasmon resonance (LSPR)

The experiments in this thesis investigate phenomena that rely on plasmons localised on nanoparticles. These are collective oscillations of free electrons on the surface of the nanoparticle which are bound to fixed positive ions in the metal[1] (figure 2.1). Since they are confined to the particle, they are referred to as localised surface plasmons (LSP). One way in which they arise is from an oscillating electric field from an incident electromagnetic wave, which induces a dipole in the nanoparticle[2,3].

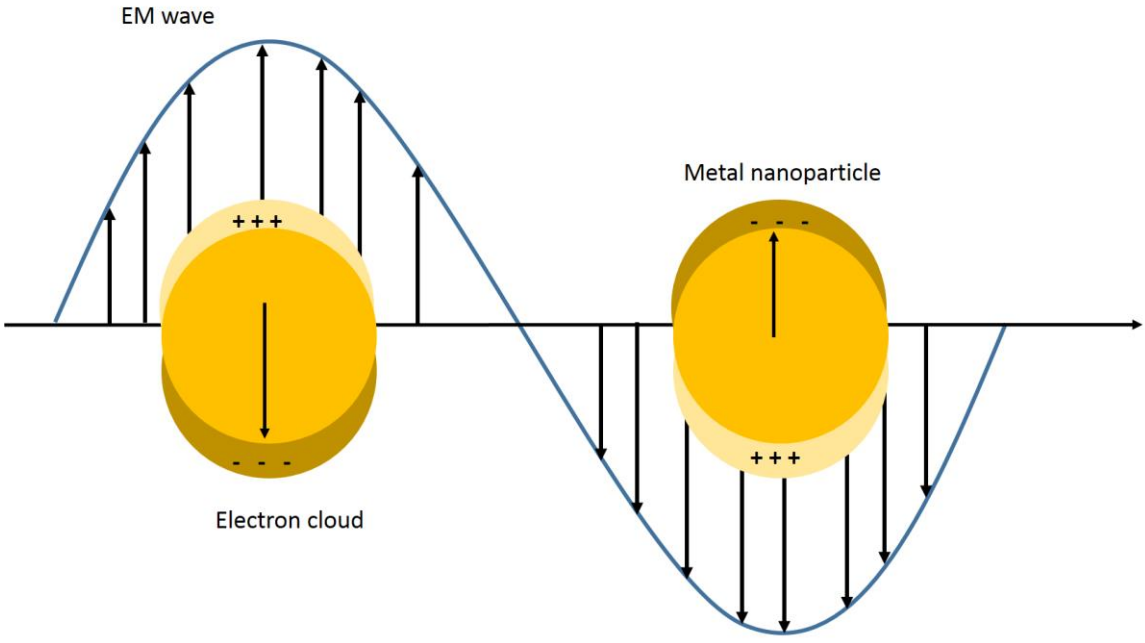

Figure 2.1 Diagram showing the collective oscillation of electrons on a metal nanoparticle's surface[1]

Plasmonic particles are able to generate strong enhancement of incident light, by localising it to subwavelength regions. This enhancement is especially strong when the incident light's wavelength matches the plasmonic resonance of the particle. As a result, researchers have carried out many investigations into understanding plasmonics in nanoparticles so that their resonance and enhancement can be controlled and used in a variety of applications[4-6].

It is possible to carry out an approximation of the plasmonic resonance[2] for the case when a nanosphere is much smaller than the wavelength of the incident electric field. This is because the electric field can be assumed to be uniform throughout the particle, and the problem can be treated electrostatically instead of electromagnetically. Furthermore, it is assumed that the particle is homogeneous and isotropic, with a radius *a*, which is set at the origin of a uniform, static electric field $\boldsymbol{E} = E_0\hat{\boldsymbol{z}}$ (figure 2.2). The surrounding medium is also assumed to be isotropic, non-absorbing and with a dielectric constant ε_m. The incident electric field lines are parallel to the z-direction. The particle's dielectric response is given by a complex dielectric function $\varepsilon(\omega)$.

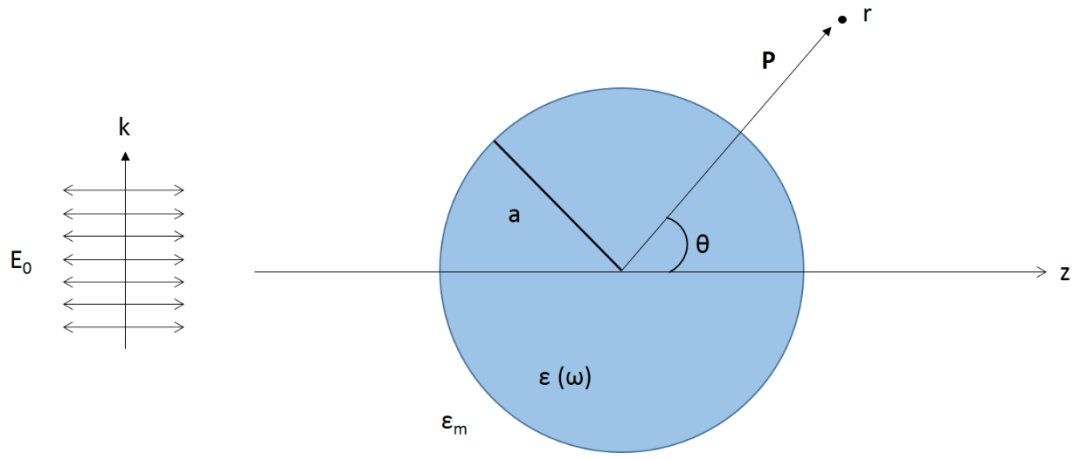

Figure 2.2 Diagram showing the parameters considered for the quasistatic approximation for a homogeneous particle in an electric field whose field lines are horizontally polarised[2]

The way the electromagnetic field interacts with the nanoparticle can be understood by considering the Laplace potential equation, which states:

$$\nabla^2 \phi = 0 \tag{2.1}$$

where ϕ is the electric potential. This relates to the electric field such that:

$$\mathbf{E} = -\nabla \phi \tag{2.2}$$

The azimuthal symmetry of the problem gives the general solution as:

$$\phi(\mathrm{r},\theta) = \sum_{l=0}^{\infty} \left[A_l r^l + B_l r^{-(l+1)} \right] P_l(\cos\theta) \tag{2.3}$$

where $P_l(\cos\theta)$ are the Legendre Polynomials of order l, and θ is the angle between the position vector **P** at point r and the z-axis.

A condition for solving equation 2.3 is that the potential at the origin of the geometry (r = 0) is finite. Therefore, the potential inside and outside the nanoparticle is given by:

$$\phi_{In}(r,\theta) = \sum_{l=0}^{\infty} A_l r^l P_l(\cos\theta) \tag{2.4}$$

$$\phi_{Out}(r,\theta) = \sum_{l=0}^{\infty} \left[B_l r^l + C_l r^{-(l+1)} \right] P_l(\cos\theta) \tag{2.5}$$

Coefficients A_l, B_l, and C_l can be solved at boundary conditions at $r \to \infty$ and at the particle's surface $r = a$. As $r \to \infty$, $\phi_{out} \to -E_0 z = -E_0 r \cos\theta$. This is because the nanoparticle no longer has any influence on the electric field, and so it matches the excitation field[7]. This gives values for B_l as $-E_0$ for $l = 1$ and 0 for $l \neq 1$. The other coefficients are solved at the particle's surface r = a. The

tangential elements of the electric field must be continuous at the surface of the nanoparticle. This gives the condition:

$$-\frac{1}{a}\frac{\delta\phi_{In}}{\delta\theta}\Big|_{r=a} = -\frac{1}{a}\frac{\delta\phi_{Out}}{\delta\theta}\Big|_{r=a} \tag{2.6}$$

The normal components of the displacement field must also be equal, such that:

$$-\varepsilon_0\varepsilon\frac{\delta\phi_{In}}{\delta r}\Big|_{r=a} = -\varepsilon_0\varepsilon_m\frac{\delta\phi_{Out}}{\delta r}\Big|_{r=a} \tag{2.7}$$

These boundary conditions give results of $A_l = C_l = 0$ for $l \neq 1$. When the other A_l and C_l results are calculated[2,8,9], equations for the potential are evaluated as:

$$\phi_{In} = -\frac{3\varepsilon_m}{\varepsilon+2\varepsilon_m}E_0 r\cos\theta \tag{2.8}$$

$$\phi_{Out} = -E_0 r\cos\theta + \frac{\varepsilon-\varepsilon_m}{\varepsilon+2\varepsilon_m}E_0 a^3\frac{\cos\theta}{r^2} \tag{2.9}$$

The potential on the outside can be rewritten if a dipole moment is introduced:

$$\phi_{Out} = -E_0 r\cos\theta + \frac{\boldsymbol{p}.\boldsymbol{r}}{4\pi\varepsilon_0\varepsilon_m r^3} \tag{2.10}$$

$$\boldsymbol{p} = 4\pi\varepsilon_0\varepsilon_m a^3\frac{\varepsilon-\varepsilon_m}{\varepsilon+2\varepsilon_m}\boldsymbol{E}_0 \tag{2.11}$$

The applied field induces the dipole moment inside the particle, which is proportional to the electric field. Polarisability can be extracted from equation 2.11, giving the result:

$$\alpha = 4\pi a^3\frac{\varepsilon-\varepsilon_m}{\varepsilon+2\varepsilon_m} \tag{2.12}$$

From equation 2.12, polarisability will become maximum when $|\varepsilon + 2\varepsilon_m|$ approaches zero. This gives a resonance condition of:

$$Re[\varepsilon(\omega)] = -2\varepsilon_m \tag{2.13}$$

This result is called the Fröhlich condition[2,10,11].

Since plasmonics require that the particle's material must have free electrons, it is assumed that the particle has a permittivity that follows the Drude model such that:

$$\varepsilon(\omega) = \varepsilon_\infty\left(1 - \frac{{\omega_p}^2}{\omega^2 + i\gamma_0\omega}\right) \tag{2.14}$$

where $\omega_p = \sqrt{\frac{ne^2}{\varepsilon_0 m}}$ is the plasma frequency of the free electron gas (i.e. the plasmon on the particle's surface), n is the number density of electrons in the gas, m is an electron's effective mass, $\gamma_0 = 1/\tau$ is the damping term which relates to the characteristic collision frequency of oscillating electrons due to an external electric field (it is small compared to ω), and ε_∞ is the background dielectric function. As a result of the collisions occurring, there is a damping force on the motion of the electrons, with a relaxation time of τ.

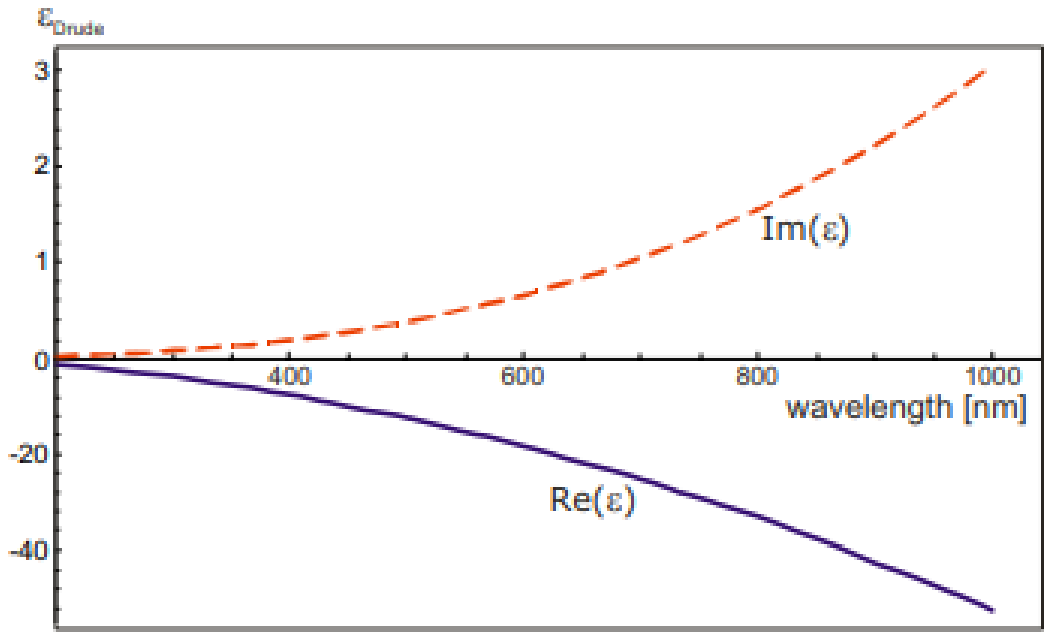

Figure 2.3 (Blue) Real and (red) imaginary parts of the permittivity of gold according to the Drude free electron model[12]

From equation 2.14, it is possible to separate the real and imaginary parts of the dielectric function such that[13]:

$$Re\big(\varepsilon(\omega)\big) = \varepsilon_\infty \left(1 - \frac{{\omega_p}^2}{\omega^2 + {\gamma_0}^2}\right) \tag{2.15}$$

$$Im\big(\varepsilon(\omega)\big) = \left(\frac{\varepsilon_\infty {\omega_p}^2 \gamma_0}{\omega(\omega^2 + {\gamma_0}^2)}\right) \tag{2.16}$$

Both the real and imaginary parts can be plotted, to produce a Drude-Lorentz model (figure 2.3). It can be seen in the visible region (400-825 nm) that the real part of the permittivity has a negative value (which consequently increases the metal's reflectivity and thus prevents the light from deeply penetrating the substrate) and the imaginary part is positive, but small. Since the imaginary part correlates with absorption, this will also be small, which allows phenomena like plasmonics to take place. These conditions are satisfied for materials such as gold, silver and copper. Furthermore, since these metals

have plasma frequencies in the UV range, their resonance wavelengths occur in the visible regime. This makes them ideal for sensing technology.

It is clear from equations 2.12 and 2.13 that the plasmonic resonance is very sensitive both to the material of which the particle is made[14] and its surrounding medium[15-17]. Any change to its environment will result in a shift in the resonance condition, thereby shifting the resonant wavelength[18].

2.1.2 Effect of particle size and shape on resonance

In addition, it is also important to consider how other aspects affect plasmonic resonance. The size of the particle, for example, will have an important effect on the plasmonic resonance. When the particles start to get closer in size to the reduced wavelength ($\frac{\lambda}{2\pi}$) of the incident light (>60 nm diameter), it will no longer be homogeneously polarised. This leads to a retardation effect in the electric field phase over the particle, which causes shifts in the resonance, as well as a broadening in the resonant modes, due to interband damping where the localised plasmon overlaps with the interband transitions[19] (figure 2.4). Furthermore, a larger particle size, combined with the phase retardation, means that higher order modes can now be excited in the particle[20-22].

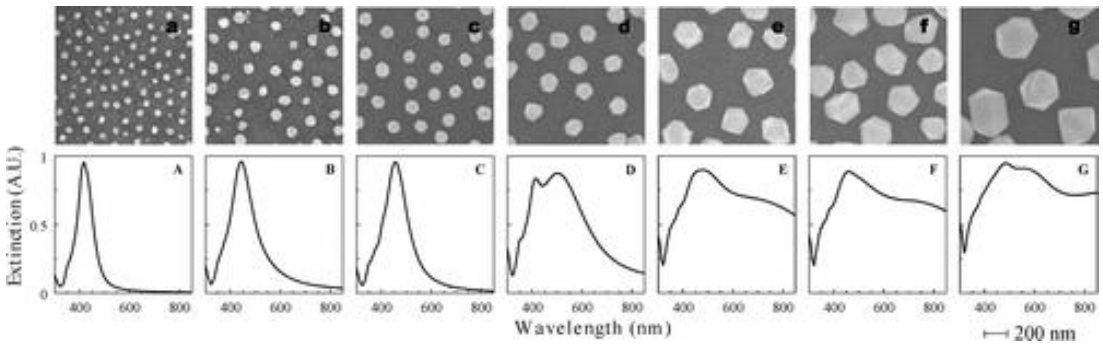

Figure 2.4 Extinction spectra and the corresponding electron microscope images for silver nanoparticles of diameter (a) 46, (b) 59, (c) 86, (d) 128, (e) 160, (f) 194, and (g) 287 nm in water[19]

It is also important to consider the effect of the nanoparticle's shape on the plasmonic resonance. This is because it will change the polarisability of the particle, and therefore the way in which the electrons oscillate and their resonant frequency[23-25]. For example, the resonance in a nanocube (figure 2.5b) is redshifted[23] compared to that of a sphere (figure 2.5a). This is because a cube has sharp corners where charges tend to concentrate, in a phenomenon called the lightening rod effect[23,26]. Since there is now more separation between the charges, there is a smaller Coulombic restoring force which increases the oscillation time and reduces the plasmon frequency. Furthermore, additional resonant modes arise from the reduced symmetry in the nanocube compared to the sphere. This means that there are more ways in which the electrons can be polarised in the cube, which is observed as additional plasmonic modes.

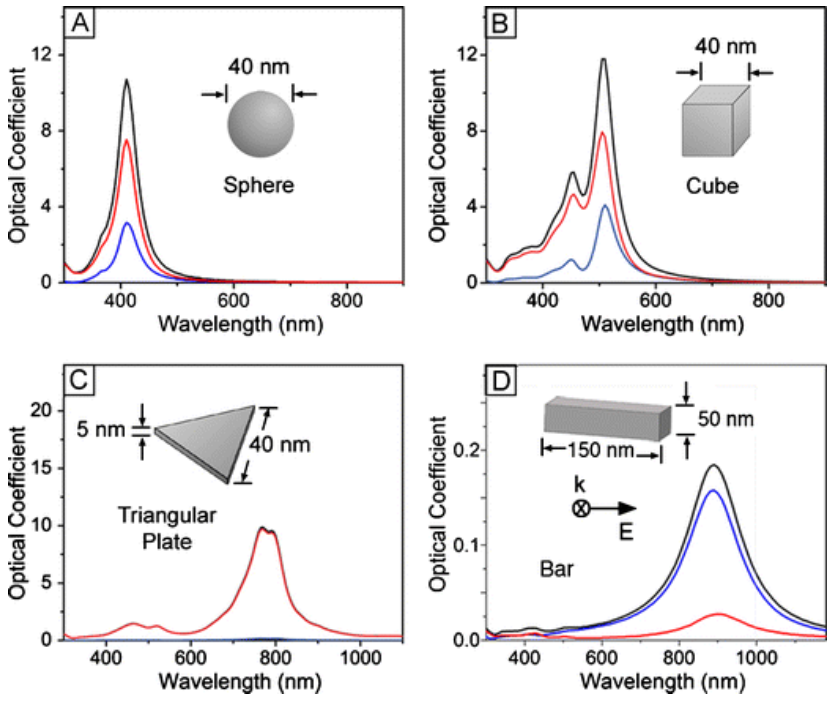

Figure 2.5 Optical responses calculated for silver (a) nanospheres, (b) nanocubes, (c) nanotriangles, and (d) nanobars in water. (Red) absorption, (blue) scattering, and (black) extinction spectra were calculated using (a) Mie theory and (b-d) the discrete dipole approximation. Note that the illumination angle was not provided in the original paper[27]

This is supported by examining nanotriangles which have less symmetry and more charge separation, which results in the main plasmonic resonance being further redshifted (figure 2.5c). In the case of nanobars, plasmonic resonance is achieved along the transverse and longitudinal axes. Since the transverse axis is small, its resonant mode appears at low wavelengths, while the longitudinal axis is further redshifted than the other shapes (figure 2.5d).

2.1.3 Interparticle distance

Another effect that has been shown to be interesting is when plasmons in one particle couple to plasmons in another, such as in a dimer system (figure 2.6). Such systems are interesting because they can be tuned by changing the separation.

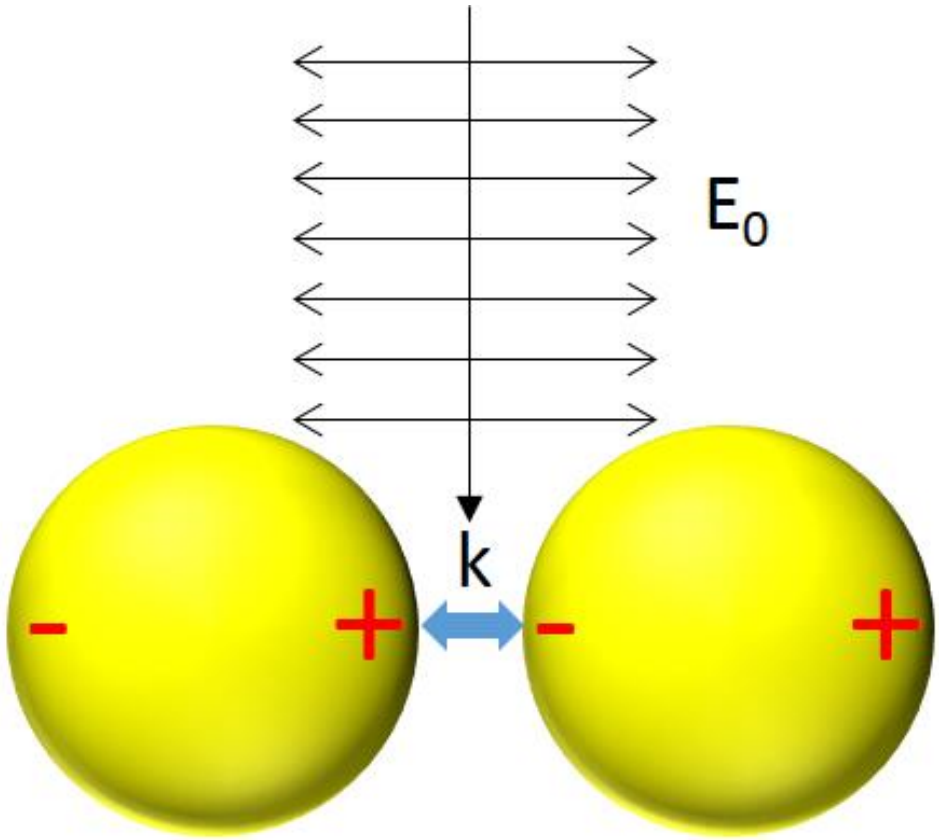

Figure 2.6 Schematic diagram illustrating a horizontally polarised electric field inducing plasmonic coupling between charges in two nanoparticles, forming a dimer geometry[28]

Resonance shifts occur due to the near-field of one particle affecting the field distribution of the other. Generally, it has been shown that the resonant wavelength redshifts as the particles get closer and coupling becomes stronger, following almost an exponential relation (figure 2.7)[29-31].

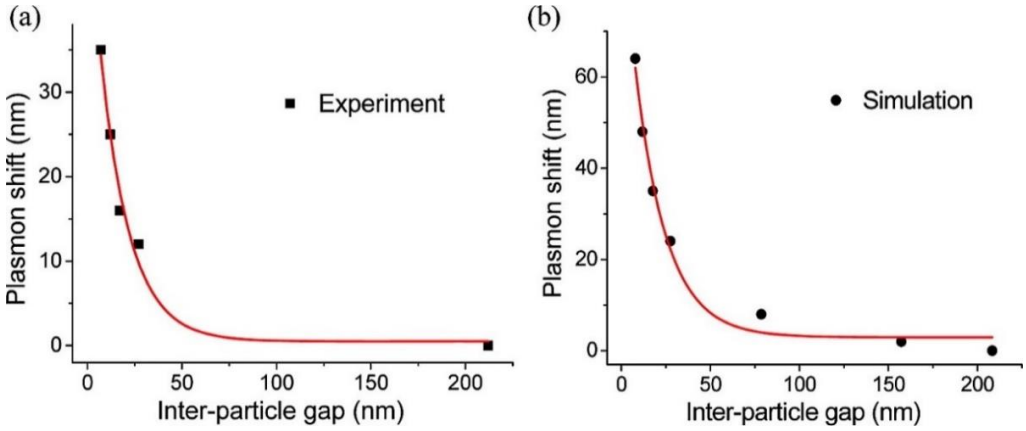

Figure 2.7 Graphs showing how the plasmonic resonance of a gold nanodisc dimer system changes with interparticle distance for (a) experiments and (b) DDA simulations[31]

An analogy has previously been drawn[32,33] between coupled nanoparticles in a dimer geometry and two parallel LC circuits coupled by a capacitor, where redshifts are observed when the circuits are moved closer together and the coupling strength increases.

The spheres in dimers act like nanoantennas, focusing incident light into the nanogap and creating a large electric field there. This makes dimers very useful for phenomena such as surface-enhanced Raman scattering[34]. Classically, it was predicted that the enhancement should increase as the particles get closer together. However, at very close separations (usually <1 nm), electrons can tunnel from one particle to the other. This neutralises positive charge on the other side of the junction and reduces the built up electric field[35]. Furthermore, at slightly larger separations (>1 nm) additional screening of the hotspot occurs due to electrons in the nanoparticle repelling charges in the plasmons. This is called Thomas-Fermi screening[36]. However, it

cannot be assumed that the electrons on the particle's surface are point charges. Instead, they must be considered to be spread over the volume of the particle, penetrating it to a depth on the order of the Thomas-Fermi screen length (1 Å)[37,38]. This gives it a continuous charge density. Because of this, the nanoparticle's permittivity is not constant, but becomes spatially dispersive. Such a spread leads to a spread in the plasmonic resonance and therefore a broadening in the spectrum. This is called the non-local effect. If the charge was assumed to be localised, the nanoparticle would need to have a singularity at the contact point with the other particle where a large amount of the charge resides. As the plasmons are focused into the singularity, their group velocity and effective wavelength acutely decrease[39]. In other words, the plasmon gets compressed as it is forced into the tiny area of the singularity. This subsequently increases the intensity of the plasmon inside the gap. When the non-local effect is considered, the charge is spread over a wider area, which prevents compression and so the field enhancement decreases[38].

2.1.4 Nanoparticle on mirror geometry

Although the dimer geometry is a useful way of tuning plasmonic resonance and enhancement, it is difficult to bring two nanoparticles together with a specific interparticle spacing in a way that is precise and repeatable. One way to overcome this is to place the particles on top of a reflective substrate (figure 2.8). When a nanoparticle is drop-cast onto a reflective film, charges in the particle induce image charges in the substrate (which satisfy the electromagnetic boundary conditions of the geometry) from which dipoles are created[40]. Thus, virtual dimers are formed with plasmons between the particle

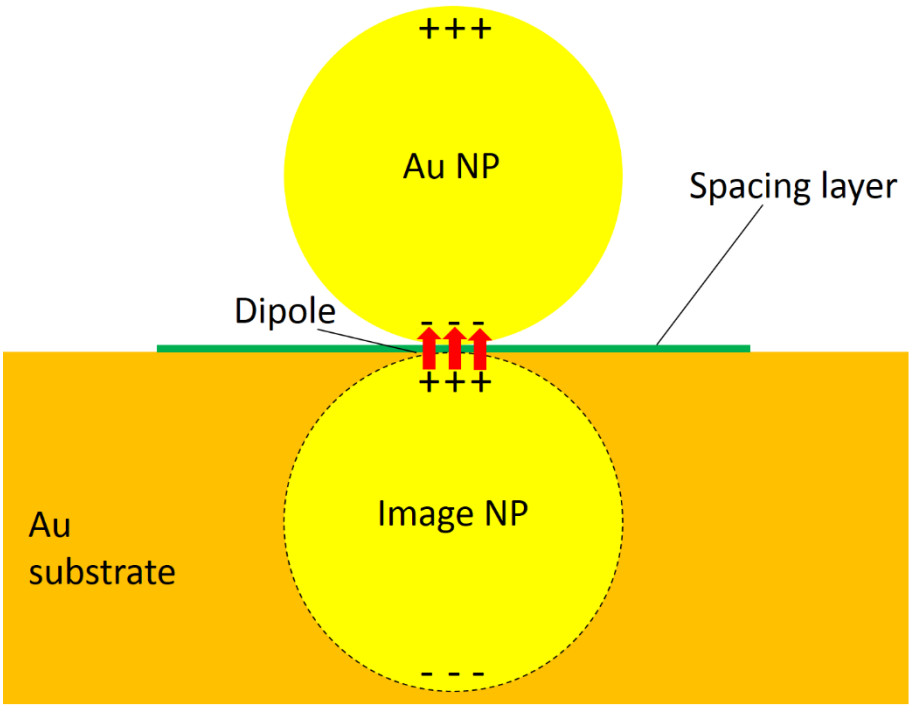

Figure 2.8 Diagram of the nanoparticle on mirror geometry

and its image charges. This is called the nanoparticle on mirror (NPoM) geometry. Charge induced in the substrate depend on the reflective properties of the substrate and whether there is a dielectric spacing layer on top of it. When a thick spacing layer is used, the charges in the particle induce much less image charge. This can be used to precisely separate the particle from its image to investigate how interparticle separation affects plasmonic resonance, in particular on the nanometre scale[38]. This method, which was predicted theoretically by Aravind & Metiu (1982)[41], is often used because it is analogous to the dimer geometry, but allows investigations of such systems in a way that is easy, precise and reproducible[42-44].

The interaction with the image charges, and the plasmonic properties of the NPoM depends on the properties of the film. On reflective substrates which are polarisable[45,46] (i.e. films with a sufficiently large relative permittivity ε_s to support image charges), the particle is able to induce two principal image charges in the film. These charges are screened by a factor $\frac{\varepsilon_s - 1}{\varepsilon_s + 1}$, which goes to

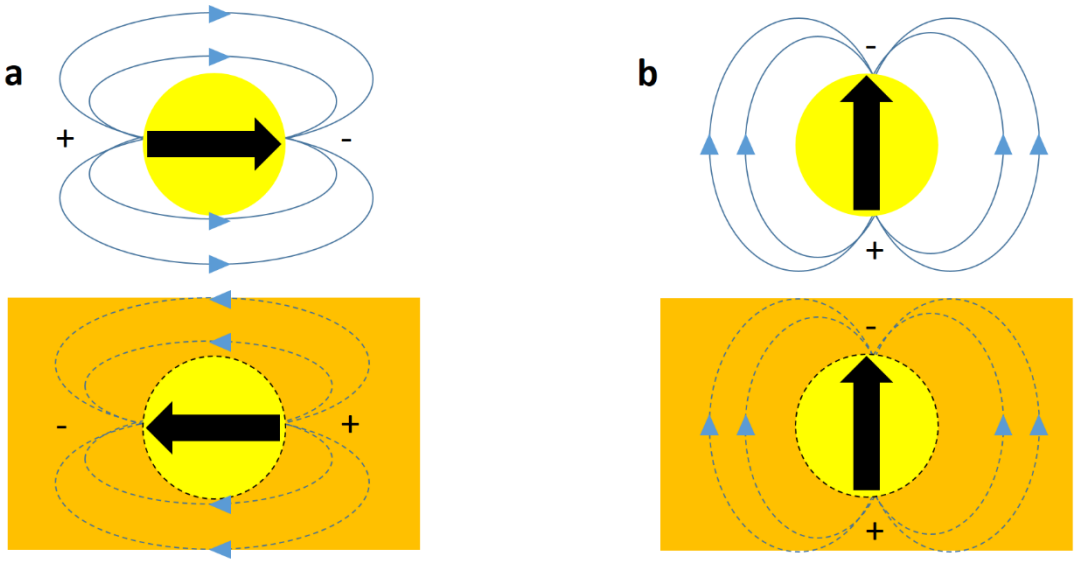

Figure 2.9 Diagrams demonstrating plasmonic modes formed from a plasmonic particle inducing (a) horizontal and (b) vertical image dipoles in the substrate. When the particle is near the substrate, its horizontal dipole decreases due to destructive interference with its image dipole, while the vertical mode increases due to constructive interference with its image dipole. Black arrows indicate the orientation of the dipole[47]

1 (a perfectly reflected image) as ε_s increases. These image charges form two dipoles in the substrate. One acts parallel to the substrate's surface, forming the transverse resonance mode (figure 2.9a), while the other acts perpendicular to the substrate's surface, forming the vertical dipole resonance mode[47] (figure 2.9b). These image dipoles will also have an effect on the scattering of incident light. It has been observed that when the nanoparticle is deposited on some substrates that the particles show a distinctive doughnut shape (a void surrounded by a bright spot) in dark-field microscopy[45] (figure 2.10). This is indicative of a strong vertical dipole, and can be understood when figure 2.9 is examined. Near the substrate, the transverse mode in the

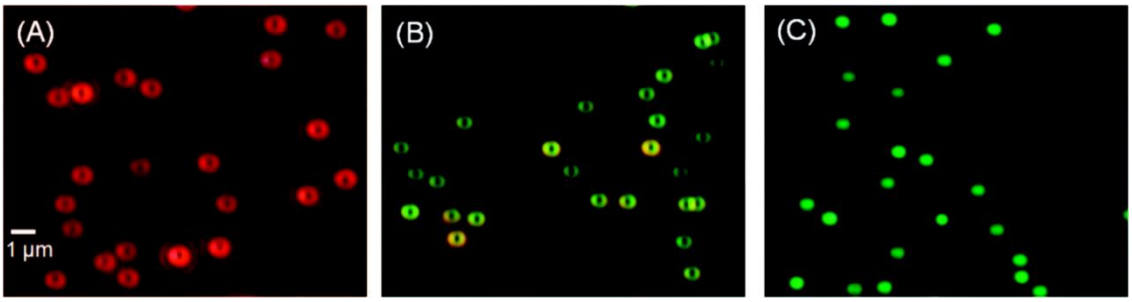

Figure 2.10 Dark-field images of Au NPs on (a) a thin Au film, (b) a Si wafer, and (c) a quartz wafer[45]

particle is out of phase with the induced dipole in the substrate, resulting in destructive interference and a much weaker scattering intensity in the far-field. Conversely, the vertical mode is in-phase with the induced dipole, leading to constructive interference. Since an electric dipole radiates strongly perpendicular to the dipole axis and weakly along the dipole axis in the far field, the emission of the vertical dipole results in a void surrounded by a bright spot in dark-field images.

Furthermore, when incident light (with a component that is vertically polarised) is shined at a NPoM, the particle is able to focus much of its energy to the gap region between the bottom of the particle and the film's surface[48,49]. This leads to a large amount of charge being built up in the gap region, which in turn induces charge on the opposite side of the gap. When interaction between these charges is strong, vertical dipoles are induced inside the gap, which redshift as the gap gets smaller and coupling with the image charges gets stronger[49] (figure 2.11). These modes can also result in doughnut shapes

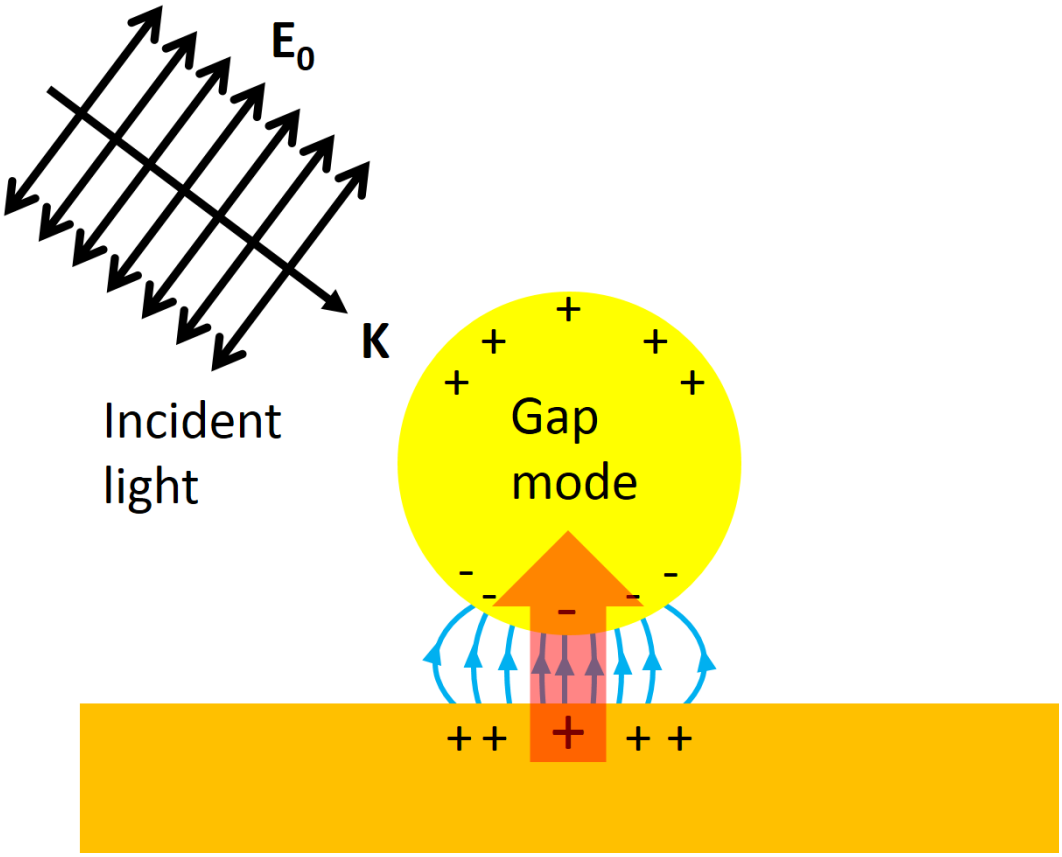

Figure 2.11 Diagram showing charges and induced charges around the NPoM's gap region forming strong plasmons (blue lines). The red arrow indicates the orientation of the gap's dipole[48]

which can be seen in the microscope, although it is much less noticeable than the doughnut shape from the vertical mode.

Further changes can occur when the particle is brought close to a substrate that is plasmonic[46,50,51]. This is because, in addition to interaction with image dipoles, the particle will also experience hybridisation with the film's plasmons, depending on the particle's separation from the film, and the film's thickness. To describe plasmon hybridisation, the conduction electrons are modelled as an incompressible electron gas[52]. When such a gas is deformed, a charge distribution will appear around the metal, i.e. a primitive (unhybridised) plasmon. In the case of film plasmons, it is important to examine how primitive plasmons on the top gold-air boundary interact with

those on the bottom boundary, especially when the film is thin. It has been observed that charges that form the plasmons on the top boundary induce opposite charges at the bottom boundary, called secondary charges[53]. The same is true of the bottom plasmons inducing secondary charges on the top boundary. Coulomb interaction between the primitive plasmons and secondary charges results in the formation of two modes. One is a high-energy anti-bonding mode where like-charges align symmetrically on each side of the substrate (figure 2.12b). This is counterintuitive, since like-charges should normally repel. However, it has been observed the attractive nature between plasmons and secondary charges is stronger than the repulsion, thus allowing the symmetric alignment of charges[53,54]. A second mode at low energies conversely arises in the film from alignment from bonding between positive and negative charges on opposite boundaries (figure 2.12a).

When a particle is placed on top of a plasmonic substrate, it interacts strongly with the bonding film plasmons, whose energies are similar to those in the particle. However, the anti-bonding mode has much higher energies than the particle plasmons, and so there is much less interaction between these modes. It is also important to understand that the film is made of a continuum of plasmons with energies ranging from 0 to the bulk plasmon frequency of the metal ω_B, with a density of states that peaks around the surface plasmon energy $\frac{\omega_B}{\sqrt{2}}$. As the film gets thicker, the interaction between the plasmons on opposite boundaries gets weaker, which blueshifts the film's effective

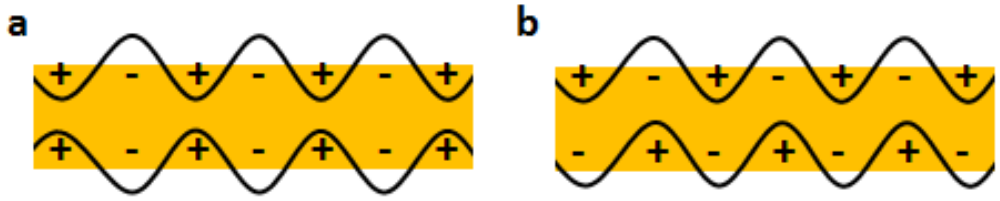

Figure 2.12 Schematic of the (a) bonding and (b) anti-bonding film plasmons[54]

plasmon band and narrows its plasmonic density of states. As the continuum shifts with film thickness, it starts to overlap with the plasmons of the nanoparticle, thus allowing hybridisation to take place[55].

Two modes form when a particle is deposited onto a plasmonic film (figure 2.13)[51,56]. The first is called the localised mode. It is mainly composed of particle plasmons since its localised states are above the film continuum. It nevertheless experiences some interference from the film as plasmons align their charge with those of the particle. This predominantly happens with short wavelength plasmons in the film's continuum (to which the particle plasmons can most easily couple), which do not shift much with film thickness. The localised mode is therefore analogous with the horizontal transverse mode. The presence of the nanoparticle also allows direct coupling between the incident field and long wavelength plasmons in the film's bonding mode through Coulomb interaction with the near-field of the particle. This happens most efficiently with long wavelength bonding surface plasmons. These are sensitive to the film thickness such that $\omega_{-} = \omega_{SP}\sqrt{1 - e^{-kT}}$ (where k is the wavenumber of the plasmon and T is the film's thickness), which

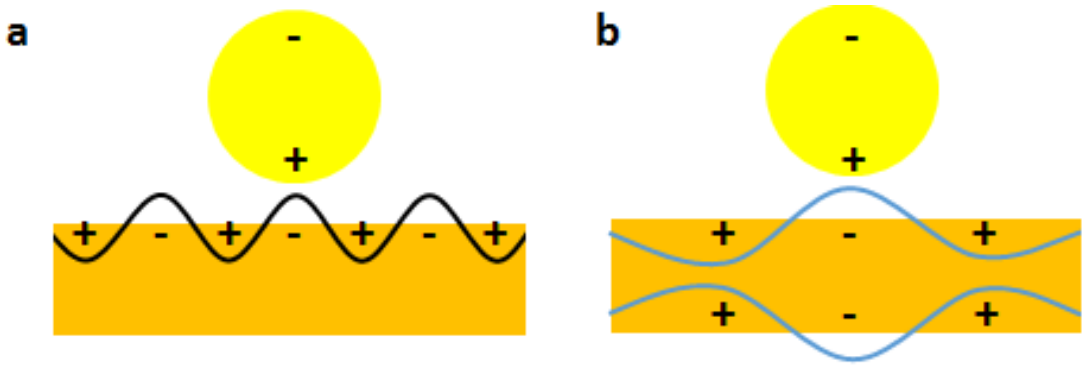

Figure 2.13 Diagram showing the charge distributions for the (a) localised and (b) virtual modes. Through Coulombic interactions, the particle's plasmons align only with short wavelength film plasmons (shown in black), while the virtual mode arises from charges in the particle's near field align only with bonding film plasmons with wavelength greater than twice the particle's diameter (shown in blue)[56]

means that factors such as the particle's proximity to the substrate and the substrate's thickness will change the plasmonic resonance of this mode. The result is a virtual resonance in the film's continuum composed mainly of film plasmons, and is analogous to the vertical dipole mode.

As with dimers, the plasmonic resonance of the NPoM blueshifts by 100-200 nm as the particle is moved further from the film[57,58].

2.2 Plexciton strong coupling

So far, plasmons have only been examined in the context of interacting individually or with other plasmons. However, they can also interact and couple with other quantum systems. For example, a molecule can be placed inside the gap of a NPoM. When incident radiation strikes a molecule, an electron in it can be excited from a molecular orbit to a higher energy level, leaving behind a positively charged hole. A bound state between the two charges forms called an exciton[59]. When placed near a metal particle, the exciton can couple to its plasmons through the exchange of energy.

If the two systems couple together, but damping dominates one or both of them, they are described as being weakly coupled. However, if energy transfer between the two is stronger than the damping, the two are said to be strongly coupled. In this case, the plasmon and exciton can no longer be treated as individual systems, but act as a single hybridised quasiparticle called a plexciton[60].

In order for strong coupling to occur, a number of conditions have to be met. Firstly, there must be alignment in the direction of the transition dipole of the exciton with the polarisation of the plasmon, otherwise the two will not interact[61,62]. This was demonstrated recently by Chikkaraddy et al. (2016)[61], who looked at methylene blue (MB) molecules inside cucurbit[7]uril molecules in the NPoM. Results showed (figure 2.14) that when the MB was

aligned perpendicularly to the gap plasmon, strong coupling (represented by a split in resonant mode) is not observed. But, when the MB is aligned parallel to the plasmon, the split does occur.

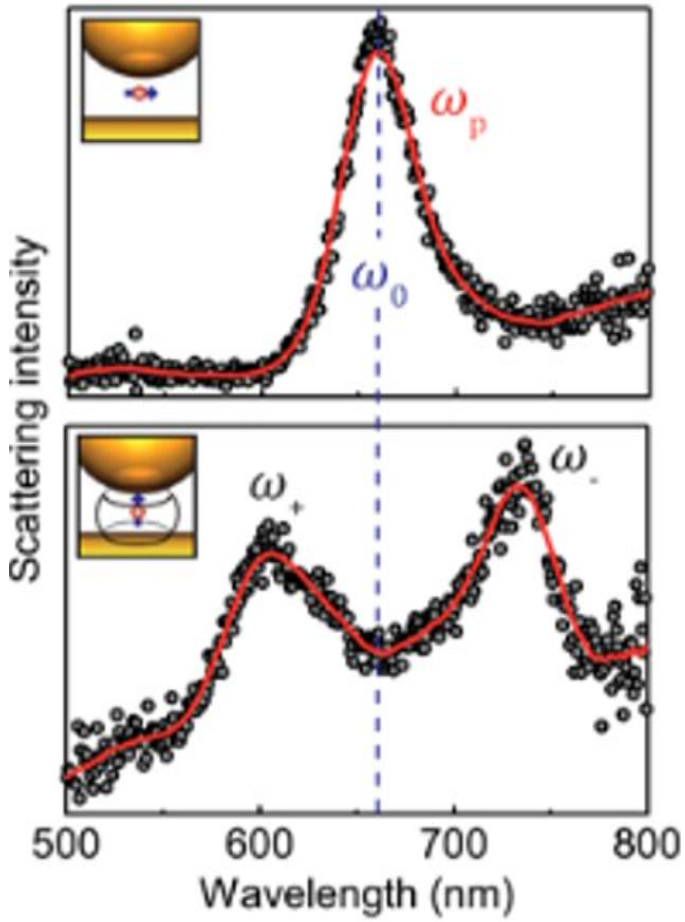

Figure 2.14 Scattering spectra from individual NPoMs where the MB molecules are aligned (top) perpendicular and (bottom) parallel to the gap plasmon[62]

The other condition required for strong coupling is an enhancement to increase the emission rate of the molecule and reduce losses in the system[63] (figure 2.15). It is important that the polarisation is along the right direction, otherwise no coupling is achieved (figure 2.15e-f).

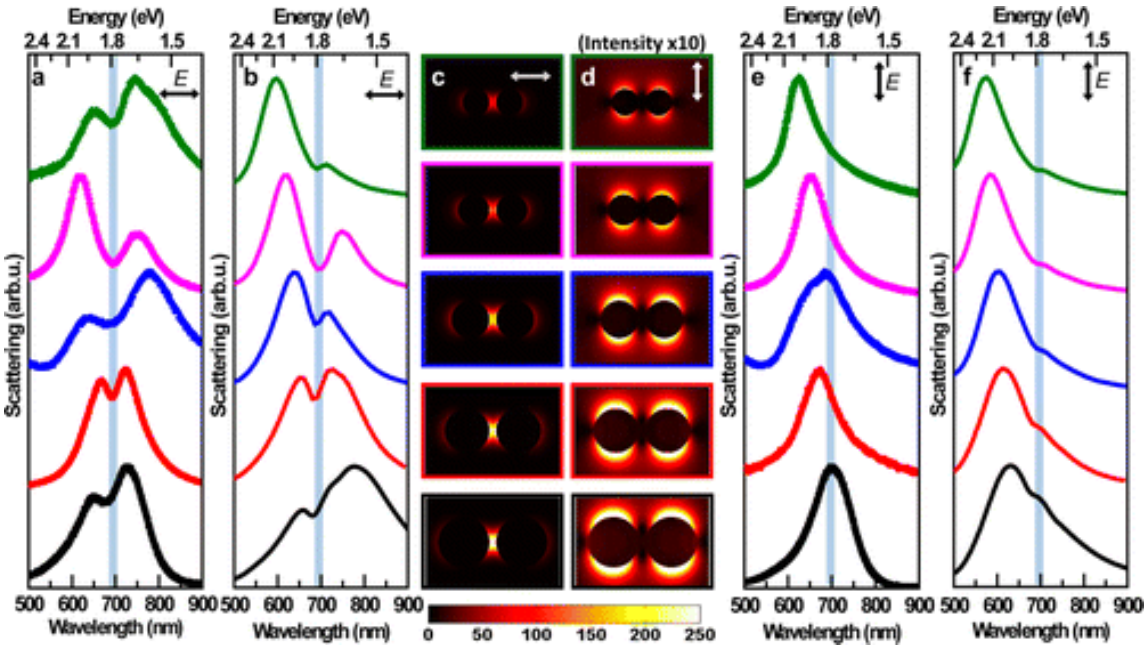

Figure 2.15 Scattering spectra for plexcitonic gold dimer J-aggregate nanostructures with nanodisks ranging in diameter from 60 to 115 nm measured for (a) longitudinal and (e) transverse polarisations. The corresponding calculated spectra are shown for (b) longitudinal and (e) transverse polarisations. The light blue line indicates the excitonic resonance of the molecule. Near-field enhancement maps calculated at the exciton resonance are shown for (c) longitudinal and (d) transverse polarisations[63]

The effect of the coupling between the two can be visualised by considering the excitations as two oscillators[63,65]. Here, two masses of m_a and m_b are coupled by two springs with spring constants k_a and k_b. In addition, the masses are bound together by a spring with a spring constant κ (figure 2.16):

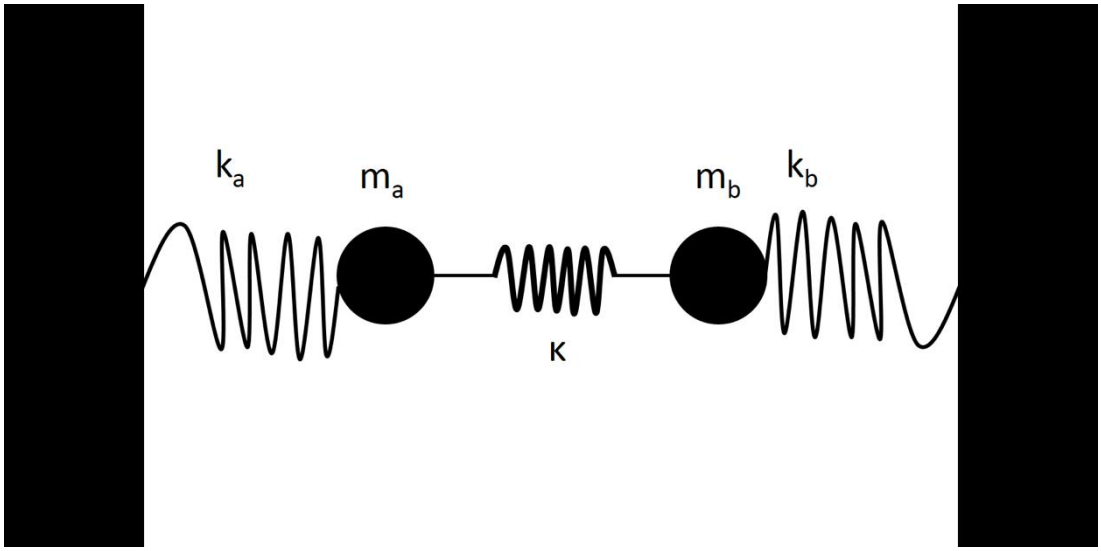

Figure 2.16 Coupling between plasmons and excitons illustrated by mechanical oscillators[64,65]

The equations of motions for the coupled masses are given as[65]:

$$m_a\ddot{x} + k_a x_a + \kappa(x_a - x_b) = 0 \tag{2.22}$$

$$m_b\ddot{x} + k_b x_b - \kappa(x_a - x_b) = 0 \tag{2.23}$$

Here, x gives the position of the masses, and solutions are given in the form of $x_i(t) = x_i^0 exp[-i\omega_{\pm}t]$, where $\omega_{\pm}$ are the eigenfrequencies. The solutions to these eigenfrequencies are:

$$\omega_{\pm}^2 = \frac{1}{2}\left[\omega_a^2 + \omega_b^2 \pm \sqrt{(\omega_a^2 - \omega_b^2)^2 + 4\Gamma^2\omega_a\omega_b}\right] \tag{2.24}$$

where $\omega_a = \sqrt{(k_a + \kappa)/m_a}$, $\omega_b = \sqrt{(k_b + \kappa)/m_b}$ and $\Gamma = \frac{\sqrt{\kappa/\omega_a}\sqrt{\kappa/\omega_b}}{\sqrt{\omega_a\omega_b}}$

The solutions can be illustrated (figure 2.17) by taking $k_a = k_0$, $k_b = k_0 + \Delta k$ and all masses to be equal (for simplicity).

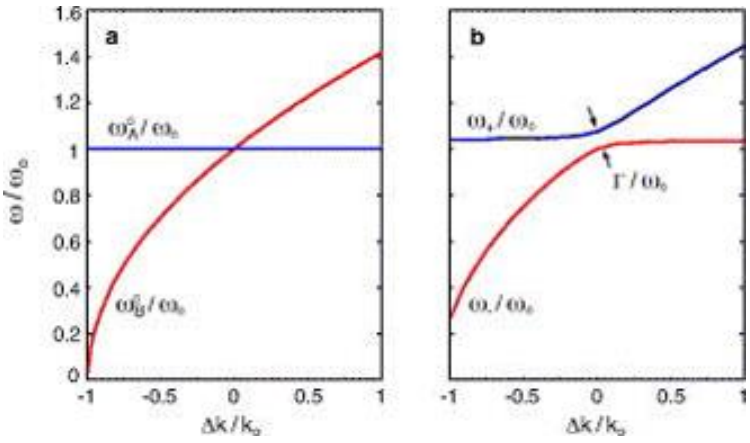

Figure 2.17 Eigenfrequencies of (a) uncoupled and (b) coupled oscillators[64]

Oscillator A's spring constant and frequency are kept constant, while oscillator B's values are gradually increased as Δk increases from $-k_0$ to $+k_0$. An intersection between the two oscillators is observed in uncoupled oscillators when their spring constants match, but not for the coupled pair. In this case, an anticrossing (characteristic of strong coupling) is observed instead, which has a frequency splitting of $\Gamma = \omega_+ - \omega_-$. Since Γ is proportional to the coupling spring constant, the anti-crossing increases with coupling strength. If damping is taken into account, the eigenfrequencies become complex, with their imaginary parts representing the linewidth, thereby smearing out the curves in figure 2.17. Plexcitons have been observed in quantum dots[66] and many types of molecules[67,68].

2.3 References

1. Hong, Y., Huh, Y.M., Yoon, D.S. & Yang, J., *Nanobiosensors based on localised surface plasmon resonance for biomarker detection*, Journal of Nanomaterials 2012 (2012): 111
2. Maier, S.A., *Nanoparticle plasmon waveguides*, Plasmonic Nanoguides and Circuits (2009): 63

3. Ma, X.C., Dai, Y., Yu, L. & Huang, B.B., *Energy transfer in plasmonic photocatalytic composites*, Light: Science & Applications 5, no. 2 (2016): e16017
4. Uchida, H. et al., *Large enhancement of Faraday rotation by localised surface plasmon resonance in Au nanoparticles embedded in Bi: YIG film*, Journal of Magnetism and Magnetic Materials 321, no. 7 (2009): 843-845
5. Jeong, N.C., Prasittichai, C. & Hupp, J.T., *Photocurrent enhancement by surface plasmon resonance of silver nanoparticles in highly porous dye-sensitised solar cells*, Langmuir 27, no. 23 (2011): 14609-14614
6. Kim, H.M. et al., *Detection of biomolecular binding through enhancement of localised surface plasmon resonance (LSPR) by gold nanoparticles*, Sensors 9, no. 4 (2009): 2334-2344
7. Louis, C. & Pluchery, O. *Gold Nanoparticles for Physics, Chemistry and Biology* (2nd ed.), chapter 3, pages 60-62, World Scientific Publishing Europe Ltd., London (2017)
8. Nasser, H., *Development of hybrid photonic and plasmonic light management interfaces for thin film semiconductor devices*, PhD thesis, Middle East Technical University (2015)
9. Jackson, J.D., *Classical Electrodynamics* (3rd ed.), John Wiley & Sons, Inc., New York (1999)
10. Rivera, V.A.G. et al., *Tunable plasmon resonance modes on gold nanoparticles in Er 3+-doped germanium-tellurite glass*, Journal of Non-Crystalline Solids 378 (2013): 126-134
11. Zhang, H. et al., *Controlled chainlike agglomeration of charged gold nanoparticles via a deliberate interaction balance*, The Journal of Physical Chemistry C 112, no. 43 (2008): 16830-16839
12. Li, Y., *Plasmonic Optics: Theory and Applications*, chapter 12, page 409, SPIE Press (2017)

13. Greco, S., *Nanooptomechanical silicon devices for sensing applications*, PhD thesis, Università Degli Studi Di Trieste (2018)
14. Lee, K.S. & El-Sayed, M.A., *Gold and silver nanoparticles in sensing and imaging: sensitivity of plasmon response to size, shape, and metal composition*, The Journal of Physical Chemistry B 110, no. 39 (2006): 19220-19225
15. Hövel, H., et al., *Width of cluster plasmon resonance: bulk dielectric functions and chemical interface damping*, Physical Review B 48, no. 24 (1993): 18178
16. Haiss, W., Thanh, N.T., Aveyard, J. & Fernig, D.G., *Determination of size and concentration of gold nanoparticles from UV-Vis spectra*, Analytical Chemistry 79, no. 11 (2007): 4215-4221
17. Link, S., Mohamed, M.B. & El-Sayed, M.A., *Simulation of the optical absorption spectra of gold nanorods as a function of their aspect ratio and the effect of the medium dielectric constant*, The Journal of Physical Chemistry B 103, no. 16 (1999): 3073-3077
18. Willets, K.A. & Van Duyne, R.P., *Localised surface plasmon resonance spectroscopy and sensing*, Annual Review of Physical Chemistry 58 (2007): 267-297
19. Juvé, V. et al., *Size-dependent surface plasmon resonance broadening in nonspherical nanoparticles: single gold nanorods*, Nano Letters 13, no. 5 (2013): 2234-2240
20. Kinnan, M.K. & Chumanov, G., *Plasmon coupling in two-dimensional arrays of silver nanoparticles: II. Effect of particle size and interparticle distance*, The Journal of Physical Chemistry C 114, no. 16 (2010): 7496-7501
21. Westcott, S.L., Jackson, J.B., Radloff, C. & Halas, N.J., *Relative contributions to the plasmon line shape of metal nanoshells*, Physical Review B 66, no. 15 (2002): 155431

22. Mati, A. et al., *Efficient excitation of higher order modes in the plasmonic response of individual concave gold nanocubes*, The Journal of Physical Chemistry C 121, no. 1 (2017): 731-740
23. Cobley, C.M., Skrabalak, S.E., Campbell, D.J. & Xia, Y., *Shape-controlled synthesis of silver nanoparticles for sensing applications*, Plasmonics 4, no. 2 (2009): 171-179
24. Grand, J. et al., *Role of localized surface plasmons in surface-enhanced Raman scattering of shape-controlled metallic particles in regular arrays*, Physical Review B 72, no. 3 (2005): 033407
25. Coronado, E.A. & Schatz, G.C., *Surface plasmon broadening for arbitrary shape nanoparticles: a geometrical probability approach*, The Journal of Chemical Physics 119, no. 7 (2003): 3926-3934
26. Kottmann, J.P., Martin, O.J., Smith, D.R. & Schultz, S., *Plasmon resonances of silver nanowires with a nonregular cross section*, Physical Review B 64, no. 23 (2001): 1096-1098
27. Wiley, B.J. et al., *Maneuvering the surface plasmon resonance of silver nanostructures through shape-controlled synthesis*, Journal of Physical Chemistry B 110, no. 32 (2006): 15666-15675
28. Miljkovic, V.D. et al., *Optical forces in plasmonic nanoparticle dimers*, The Journal of Physical Chemistry C 114, no. 16 (2010): 7472-7479
29. Huang, F. & Baumberg, J.J. *Actively tuned plasmons on elastomerically driven Au nanoparticle dimers*, Nano Letters 10, no. 5 (2010): 1787-1792
30. Acimovic, S.S., Kreuzer, M.P., González, M.U. & Quidant, R., *Plasmon near-field coupling in metal dimers as a step toward single-molecule sensing*, ACS Nano 3, no. 5 (2009): 1231-1237
31. Jain, P.K., Huang, W. & El-Sayed, M.A., *On the universal scaling behaviour of the distance decay of plasmon coupling in metal nanoparticle pairs: a plasmon ruler equation,* Nano Letters 7, no. 7 (2007): 2080-2088

32. Kadkhodazadeh, S. et al., *Scaling of the surface plasmon resonance in gold and silver dimers probed by EELS*, The Journal of Physical Chemistry C 118, no. 10 (2014): 5478-5485
33. Alù, A. & Engheta, N. *Hertzian plasmonic nanodimer as an efficient optical nanoantenna*, Physical Review B 78, no. 19 (2008): 195111
34. Talley, C.E. et al., *Surface-enhanced Raman scattering from individual Au nanoparticles and nanoparticle dimer substrates*, Nano Letters 5, no. 8 (2005): 1569-1574
35. Cha, H, Yoon, J.H. & Yoon, S., *Probing quantum plasmon coupling using gold nanoparticle dimers with tunable interparticle distances down to the subnanometre range*, ACS Nano 8, no. 8 (2014): 8554-8563
36. Jamell, C.R., *Lattice and momentum space approach to bound states and excitonic condensation via user friendly interfaces*, PhD thesis, Perdue University (2010)
37. Luo, Y. et al., *Surface plasmons and nonlocality: a simple model*, Physical Review Letters 111, no. 9 (2013): 093901
38. Ciraci, C. et al., *Probing the ultimate limits of plasmonic enhancement*, Science 337, no. 6098 (2012): 1072-1074
39. Fernández-Domínguez, A.I., Maier, S.A. & Pendry, J.B., *Collection and concentration of light by touching spheres: a transformation optics approach*, Physical Review Letters 105, no. 26 (2010): 266807
40. Maradudin, A.A., Sambles, J.R. & Barnes, W.L., *Handbook of Surface Science, Volume 4: Modern Plasmonics*, chapter 13, page 394, Elsevier B.V. (2014)
41. Aravind, P.K. & Metiu, H., *Use of a perfectly conducting sphere to excite the plasmon of a flat surface. 1. Calculation of the local field with applications to surface-enhanced spectroscopy*, The Journal of Physical Chemistry 86, no. 26 (1982): 5076-5084

42. Benz, F. et al., *SERS of individual nanoparticles on a mirror: size does matter, but so does shape*, The Journal of Physical Chemistry Letters 7, no.12 (2016): 2264-2269
43. Sigle, D.O. et al., *Observing single molecules complexing with Cucurbit [7] uril through nanogap surface-enhanced Raman spectroscopy*, The Journal of Physical Chemistry Letters 7, no. 4 (2016): 704-710
44. Sigle, D.O. et al., *Probing confined phonon modes in individual CdSe nanoplatelets using surface-enhanced Raman scattering*, Physical Review Letters 113, no. 8 (2014): 087402
45. Chen, S.Y. et al., *Gold nanoparticles on polarisable surfaces as Raman scattering antennas*, ACS Nano 4, no. 11 (2010): 6535-6546
46. Swanglap, P. et al., *Seeing double: coupling between substrate image charges and collective plasmon modes in self-assembled nanoparticle superstructures*, ACS Nano 5, no. 6 (2011): 4892-4901
47. Yu, B., Woo, J., Kong, M. & O'Carroll, D.M., *Mode-specific study of nanoparticle-mediated optical interactions in an absorber/metal thin film system*, Nanoscale 7, no. 31 (2015): 13196-13206
48. Alvarez-Puebla, R., Liz-Marzán, L.M. & García de Abajo, F.J., *Light concentration at the nanometre scale*, The Journal of Physical Chemistry Letters 1, no. 16 (2010): 2428-2434
49. Yamamoto, N., Ohtani, S. & García de Abajo, F.J., *Gap and Mie plasmons in individual silver nanospheres near a silver surface*, Nano Letters 11, no. 1 (2010): 91-95
50. Halas, N.J. et al., *Plasmons in strongly coupled metallic structures*, Chemical Reviews 111, no. 6 (2011): 3913-3961
51. Uetsuki, K., Verma, P., Nordlander, P. & Kawata, S., *Tunable plasmon resonances in a metallic nanotip-film system*, Nanoscale 4, no. 19 (2012): 5931-5935

52. Prodan, E. & Nordlander, P.J.C.P., *Plasmon hybridisation in spherical nanoparticles*, The Journal of Chemical Physics 120, no. 11 (2004): 5444-5454
53. Park, T.H. & Nordlander, P., *On the nature of the bonding and antibonding metallic film and nanoshell plasmons*, Chemical Physics Letters 472, no. 4-6 (2009): 228-231
54. Halas, N.J. et al., *Plasmons in strongly coupled metallic structures*, Chemical Reviews 111, no. 6 (2011): 3913-3961
55. Le, F. et al., *Plasmons in the metallic nanoparticle-film system as a tunable impurity problem*, Nano Letters 5, no. 10 (2005): 2009-2013
56. Uetsuki, K., *Plasmon hybridisation for tip-enhanced Raman analysis of nanomaterials*, PhD Thesis, Osaka University (2012)
57. Li, L., Hutter, T., Li, W. & Mahajan, S., *Single-nanoparticle-based heteronanojunction as a plasmon ruler for measuring dielectric thin films*, The Journal of Physical Chemistry Letters 6, no. 12 (2015): 2282-2286
58. Okamoto, T. & Yamaguchi, I. *Optical absorption study of the surface plasmon resonance in gold nanoparticles immobilised onto a gold substrate by self-assembly technique*, The Journal of Physical Chemistry B 107, no. 38 (2003): 10321-10324
59. Borisenko, V.E. & Ossicini, S., *What is What in the Nanoworld: A Handbook on Nanoscience and Nanotechnology*, chapter E, page 94, Wiley-VCH Verlag GmbH & Co. KGaA. Weinheim, 2004
60. Fofang, N.T. et al., *Plexciton dynamics: exciton-plasmons coupling in a J-aggregate-Au nanoshell complex provides a mechanism for nonlinearity*, Nano Letters 11, no. 4 (2011): 1556-1560
61. Chikkaraddy, R. et al., *Single-molecule strong coupling at room temperature in plasmonic nanocavities*, Nature 535, no. 7610 (2016): 127
62. Yuen-Zhou, J. et al., *Plexciton Dirac points and topological modes*, Nature Communications 7 (2016): 11783

63. Schlather, A.E. et al., *Near-field mediated plexcitonic coupling and giant Rabi splitting in individual metallic dimers*, Nano Letters 13, no. 7 (2013): 3281-3286
64. Novotny, L., *Strong coupling, energy splitting, and level crossings: A classical perspective*, American Journal of Physics 78, no. 11 (2010): 1199-1202
65. Stete, F., *Single particle spectroscopy using a scattering scanning near field optical microscope*, PhD thesis, Universität Potsdam, 2014
66. Ozel, T. et al., *Observation of selective plasmon-exciton coupling in nonradiative energy transfer: donor-selective versus acceptor-selective plexcitons*, Nano Letters 13, no. 7 (2013): 3065-3072
67. Balci, S. & Kocabas, C., *Ultra hybrid plasmonics: strong coupling of plexcitons with plasmons polaritons*, Optics Letters 40, no. 14 (2015): 3424-3427
68. Liu, B. et al., *Modelling plexcitons of periodic gold nanorod arrays with molecular components*, Nanotechnology 28, no. 19 (2017): 195201

Chapter 3

Materials and techniques

3.1 Introduction

In this chapter, the methods used to prepare the NPoM samples will be discussed, as well as exfoliation of 2D material spacing layers. Details will also be given about how the substrates were characterised and analysed experimentally. These techniques include optical dark-field microscopy, contrast spectroscopy, and Raman scattering.

3.2 Sample preparation and characterisation

3.2.1 Magnetron sputtering

The substrates are prepared using magnetron sputtering[1-3]. This deposition method works by assailing a target with energetic ions from a plasma, causing the removal of atoms from the target which form a thin film onto a substrate. The plasma is typically formed with an inert gas such as argon. Secondary electrons can also be produced when the ions strike the target. Using a magnetron behind the target ensures that the electrons are kept around the target, thereby forming a plasma near the target and increasing its bombardment[1] (figure 3.1).

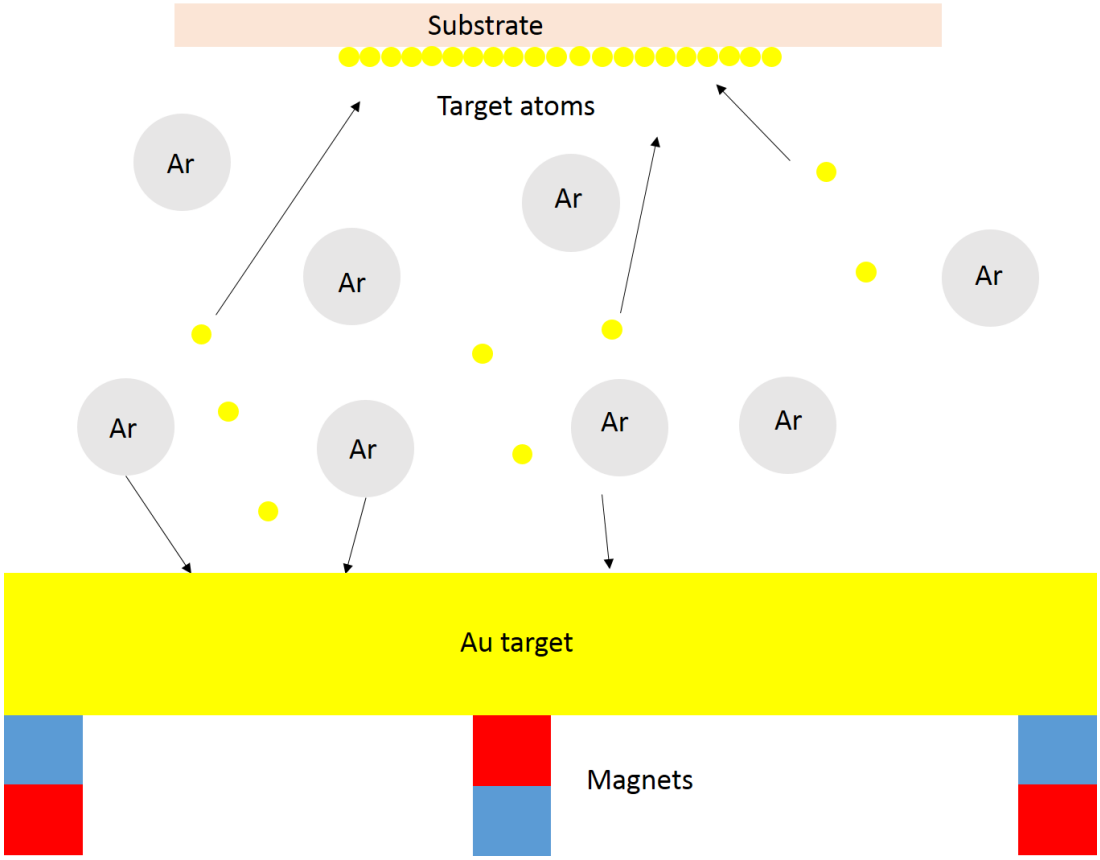

Figure 3.1 Diagram showing how magnetron sputtering works. Argon ions bombard the gold target and the resulting atoms form a thin film on the substrate[4]

3.2.2 X-ray reflectivity (XRR)

Having prepared the substrates, it was necessary to characterise the thickness of the stack of thin films. X-ray reflectometry (XRR) was used for this purpose, wherein x-rays are shined onto the surface of a sample[5]. When the x-rays meet an interface, some will refract through it while others will be reflected from its surface, depending on their incident angle with respect to the critical angle Θ_c and the density of the film (figure 3.2). Interference then occurs between the x-rays reflected at different interfaces in the stack, leading to intensity oscillations called Kiessig fringes[6] (figure 3.3). Information about the interference fringes is given by Bragg's law, which states:

$$n\lambda = \Delta = 2t \sin \Theta_t \qquad (3.1)$$

where n is an integer, λ is the wavelength of the x-rays (nm), Δ is the path difference (nm), t is the film thickness (nm) and Θ_t is the refracted angle (°), given by Snell's law.

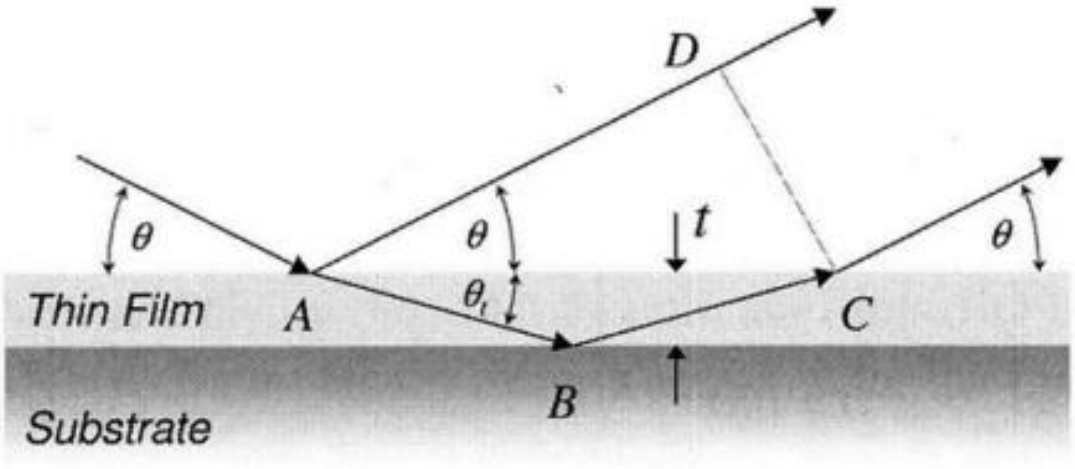

Figure 3.2 Diagram showing how x-rays are reflected and refracted when interacting with a stack of thin films[5,7]

Once the reflected x-rays are collected and analysed, the spectra are then fitted with a model constructed from a pattern from a modelled sample so that information about the film thickness, density and roughness can be gathered.

For this thesis, XRR was carried out using a Bruker D8 Discover diffractometer, DIFFRAC Measurement Centre, and Leptos 7.8 software.

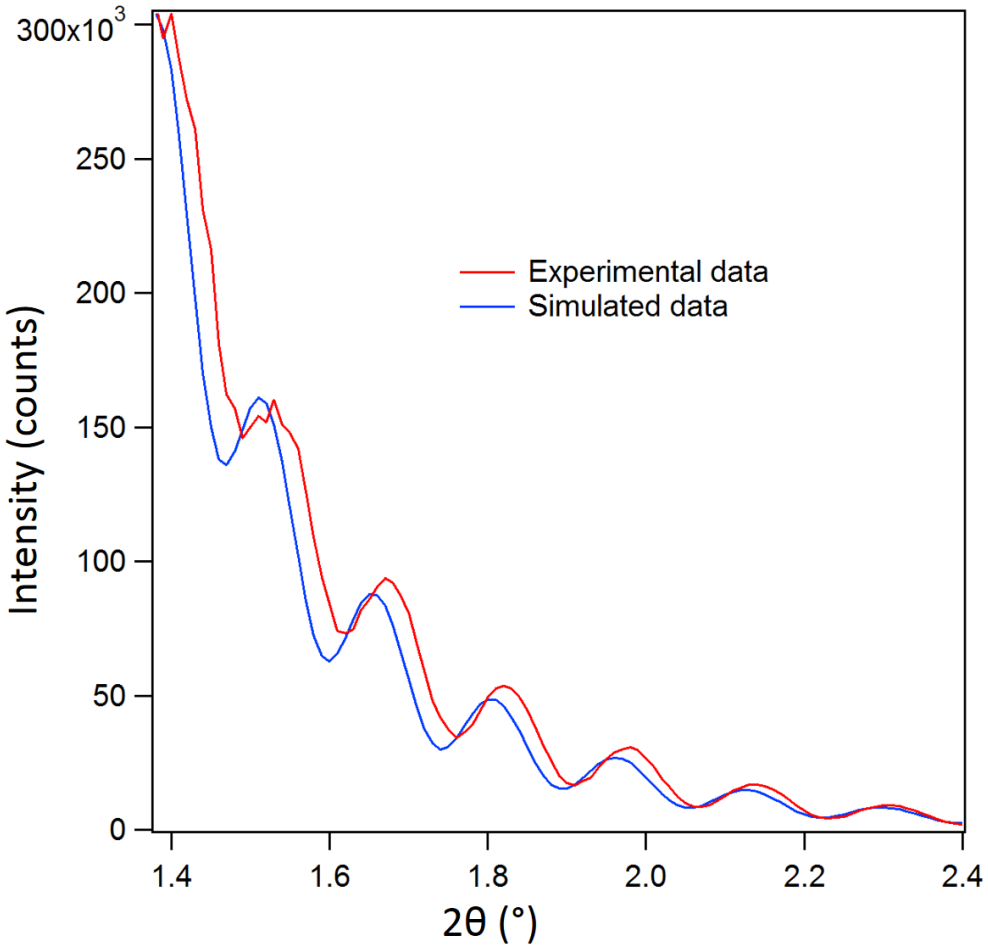

Figure 3.3 XRR spectrum of a 50 nm Au film sputtered onto a bulk silicon substrate prepared for this thesis

3.3 Gold nanoparticle preparation

Gold nanoparticles (provided by collaborators from Sungkyunkwan University, South Korea) are prepared by slow reduction of chloroauric acid in ethylene glycol. PolyDADMAC stabilises the particles, while the reduction rate is maintained by phosphoric acid. An oxidising agent (chloroauric acid) is then added to the resulting solution, which favours oxidation of gold atoms around vertices and edges, forming ultrasmooth, spherical particles[8] (figure 3.4).

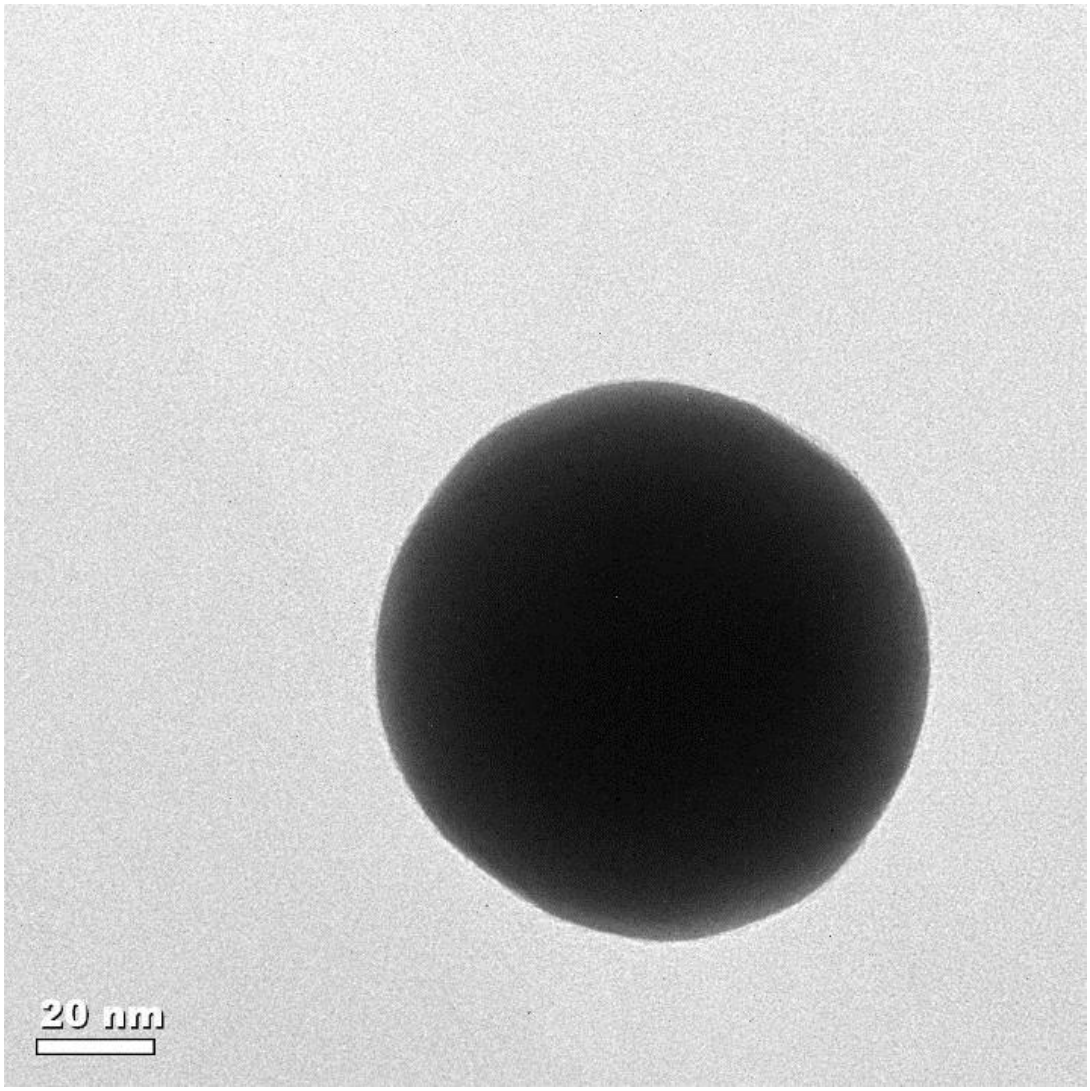

Figure 3.4 TEM image of an ultrasmooth, spherical 90 nm Au NP on a carbon grid at 97000x

The particle solution was diluted by ten times in deionised water and 1-10 μL was drop cast onto the substrate from a pipette. After the solution was allowed to dry in ambient conditions, the sample was rinsed in deionised water and dried with compressed air.

3.4 Optical dark-field microscopy and spectroscopy

After the samples were prepared, they were examined with an optical microscope. It is usually very difficult to observe nanoparticles with conventional optical microscopy because the diffraction limit means that no object below ~$\lambda/2$ can be resolved. However, dark-field microscopy can provide better contrast, which allows characterisation of the particles to take place. This works by blocking the central part of the light source with an opaque disc. As a result, the sample is only illuminated at large angles with respect to the optical axis (figure 3.5). Scattered light from the sample is then collected back through the central part of the objective lens. However, the collection angle of collected light by the objective lens is very small because of the light stop. This means that reflected light is blocked, while scattered light is collected. Since the substrate is strongly reflective (due to it being flat), it appears black in dark-field mode.

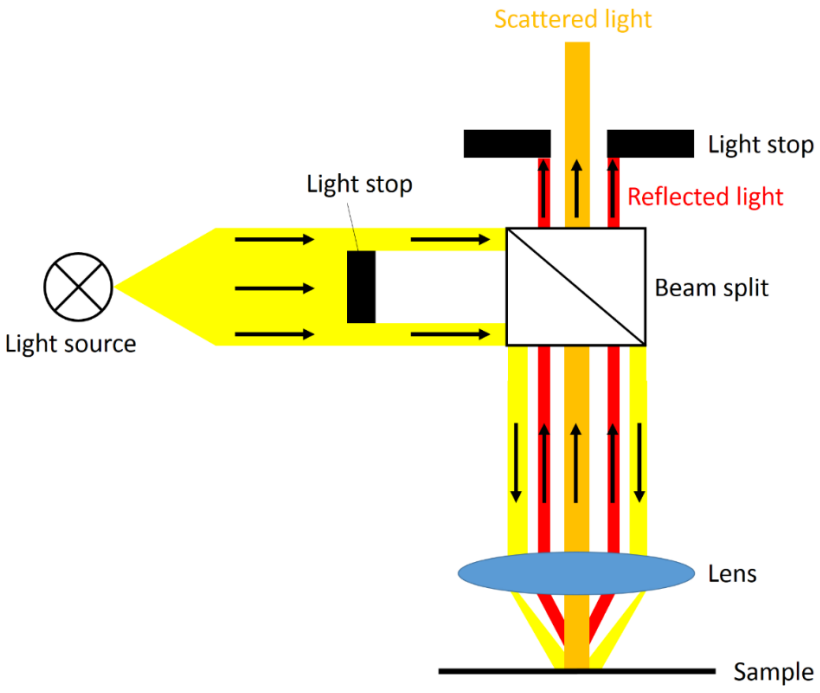

Figure 3.5 Diagram demonstrating the process of dark-field microscopy[9]

But, when light strikes a nanoparticle, it will scatter strongly in all directions, meaning it can easily be collected by the objective lens and observed with this method[9]. The nanoparticle can then be characterised both by its colour (figure 3.6b), and by measuring its scattering spectra (figure 3.8a) through an optical spectrometer coupled to the microscope with a fibre optic cable.

For this thesis, an Olympus BX-51 microscope was used, with a 12 V, 100 W halogen light source. The optical spectra were measured with a QE65 Ocean Optics spectrometer, which was coupled to the microscope through a 100 μm fibre optic cable.

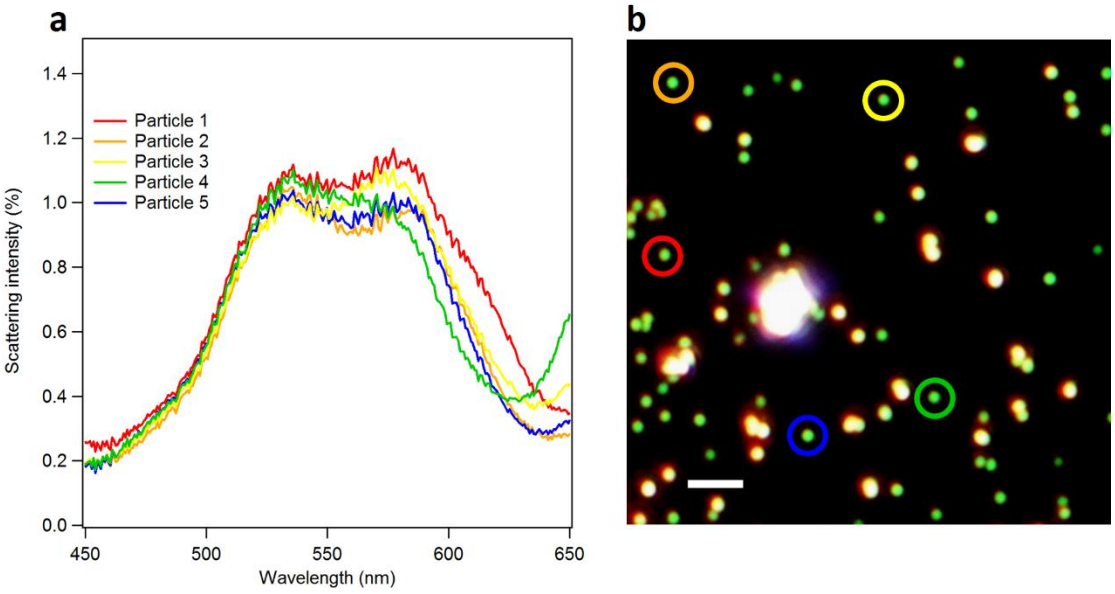

Figure 3.6 (a) Scattering spectra from five 90 nm Au NPs on 100 nm Au. (b) Optical dark-field image of 90 nm Au NPs on 100 nm. Particles measured are circled in the corresponding colours from (a). Scale bar represents 2 μm

3.5 2D material preparation and characterisation

2D materials were used throughout this project, generally as spacing layers for gold nanoparticles in the NPoM geometry. They were chosen for this purpose because they are atomically flat, electrically insulating along the out-of-plane direction, and provide robust sub-nanometre spacing between the

particle and its image, thus allowing for experiments to be carried out into quantum and other non-local effects in plasmonic dimer systems.

The 2D materials were mechanically exfoliated from natural crystals (purchased from NGS Natur-graphit GmbH) with high-tack low-stain cellotape[10]. The tape was then pressed onto the gold substrates as soon as they were removed from the sputtering chamber to avoid contamination. This produced few-layered clean flakes, onto which the nanoparticles were dropped. For this thesis, graphene and molybdenum disulphide (MoS_2) were used in several experiments.

3.5.1 Raman scattering

A fast method of characterising the thickness of 2D material flakes is to use Raman scattering. This is when a photon inelastically scatters from a molecule in a coherent process, either losing energy to the molecule (Stokes scattering) or gaining energy (anti-Stokes scattering). For these experiments, 532 nm and 633 nm lasers were used (under a 100x lens with numerical aperture 0.9) and then back scattered into a Jobin Yvon HR640 Raman spectrometer for analysis. In the case of graphene, the Raman spectrum (figure 3.7) will display peaks at ≈ 1580 cm^{-1} (the G-peak) and ≈ 2700 cm^{-1} (the 2D-peak). The G-peak relates to the vibrational mode between two neighbouring carbon atoms in the flake. When the graphene absorbs an incident photon, an electron is excited to a higher energy state, creating an electron-hole pair.

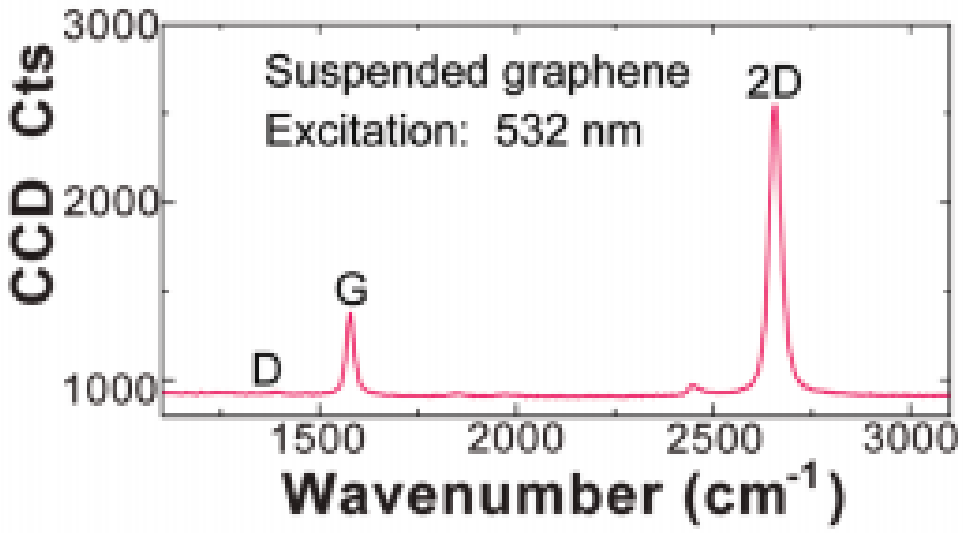

Figure 3.7 Raman spectrum measured from a suspended monolayer graphene measured with a 532 nm laser[11]

The electron then scatters from a phonon, losing some of its energy before it recombines with its hole and emits a photon (figure 3.8a). The 2D peak occurs due to a double resonance process. Here, the excited electron is scattered inelastically by two different phonons before recombining with its hole and emitting a photon (figure 3.8b)[12]

Upon measuring the Raman spectra of the graphene flake, the number of layers can be determined by taking the ratio of the intensities of the G and 2D peaks. As the number of layers increases, the ratio will also increase, since there are more carbon molecules which all contribute to the G peak[13]. Furthermore, the size and shape of the 2D peak will change. On a monolayer, it will be very narrow, but will broaden on thicker flakes, such that more than one peak could be fitted inside it (figure 3.9). This is due to the changing electronic structure of the graphene flake and increased resonances at similar frequencies[14].

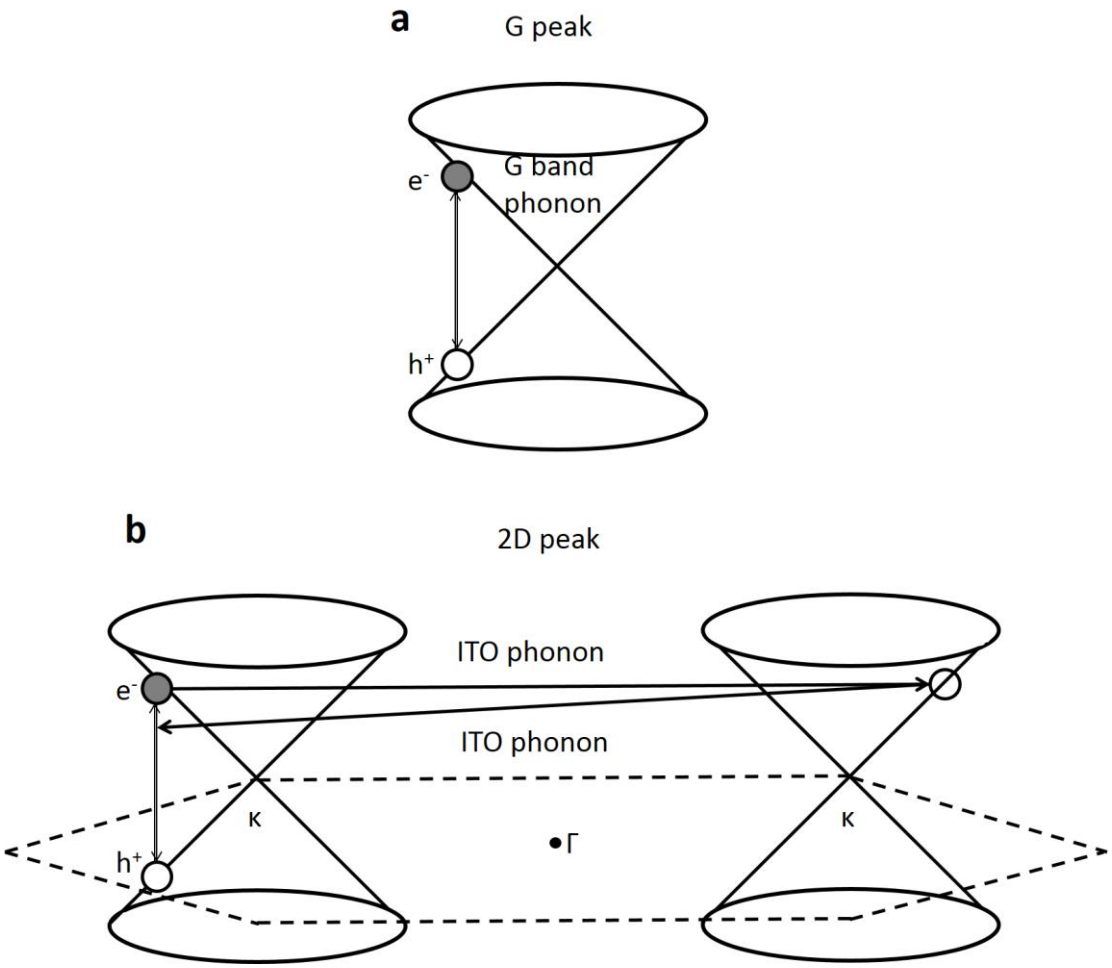

Figure 3.8 (a) First order G-band process and (b) two phonon second order for the double resonance 2D-band process. Resonance points are shown with open circles[12]

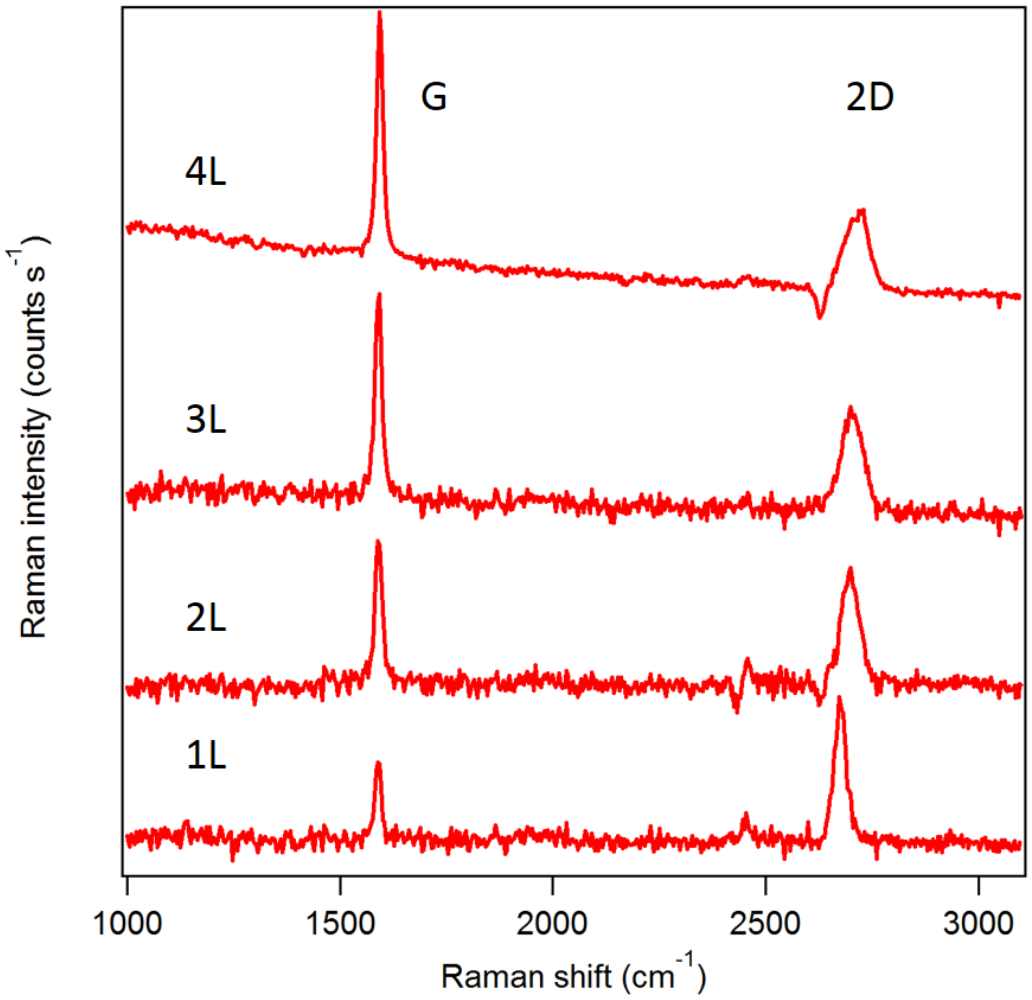

Figure 3.9 Raman spectra for graphene of 1-4 layers on bulk gold substrates taken with a 532 nm laser of 0.8 mW power

For MoS_2, two vibrational modes are observed. One (E^1_{2g} ≈ 380 cm^{-1}) comes from the two sulphur atoms vibrating antiparallel with respect to the molybdenum atom in the basal plane (figure 3.10a). The other (A_{1g} ≈ 410 cm^{-1}) comes from the sulphur atoms vibrating antiparallel to one another out of plane (figure 3.10b)[15].

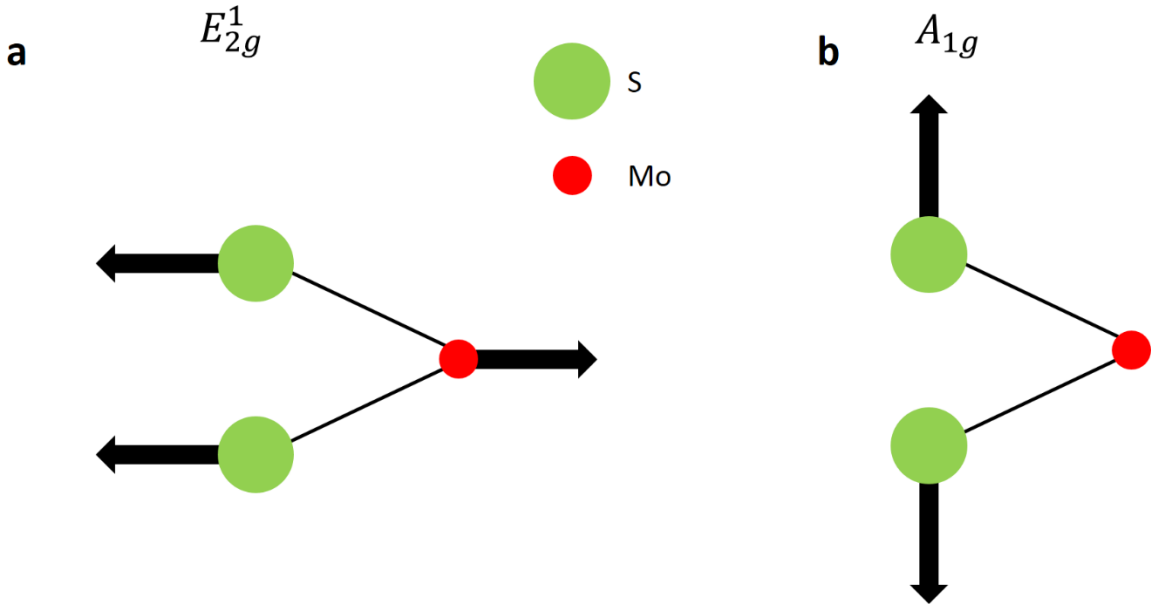

Figure 3.10 Diagram showing the vibrations of the (a) E^1_{2g} and (b) A_{1g} Raman modes[16]

It has previously been shown that increasing thickness of few layer MoS_2 causes not only an increase in the intensities of the modes, but also a shift in the E^1_{2g} and A_{1g} modes (figure 3.11).

It is principally the difference in frequency which is considered to be a more reliable indicator of the number of layers. As the number of layers increases, Van der Waals forces between the layers grows larger, suppressing atomic vibrations. This should cause each of the modes to blueshift with increasing flake thickness. However, the spectra show that the modes redshift instead. This suggests that the dominating mechanism here is Coulombic interlayer interactions, which increases the in-plane vibrations[17,18].

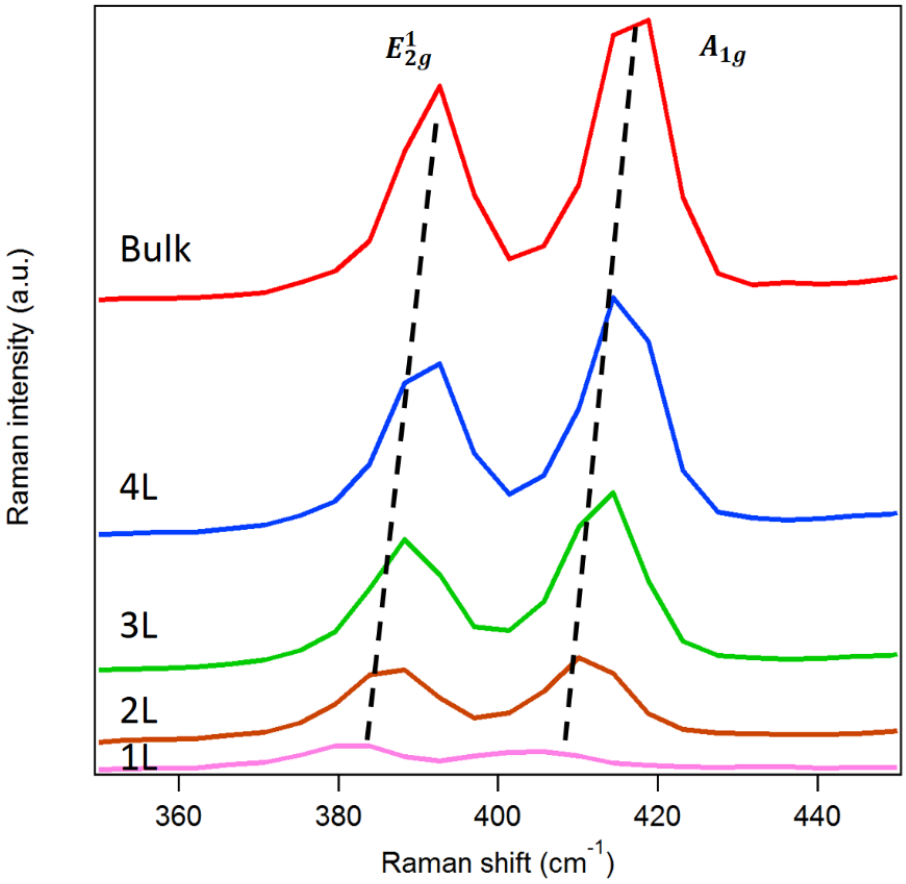

Figure 3.11 Raman spectra of MoS_2 flakes of thickness 1-4 layers, as well as bulk. Data has been offset for clarity

It should be noted, however, that although this method can give quick and useful analysis, the Raman spectra of the 2D material can easily be altered due to doping from the substrate, thereby sometimes giving false information[19].

The same instrumentation was used to carry out SERS measurements on gold nanoparticles to help to determine the source of molecular contamination.

3.5.2 Optical contrast spectra

Optical contrast spectroscopy was used as an alternative method for determining the number of layers of 2D material flakes on a gold substrate.

Contrast spectroscopy works by measuring the reflection spectrum of the white light source of the microscope on bare substrate and on 2D material flakes. Contrast is then calculated using the equation:

$$C = 1 - \frac{R_{Gr}}{R_{Au}} \tag{3.3}$$

where C is the optical contrast, R_{Au} is the reflectance of light on the bare gold substrates, and R_{Gr} is the reflectance of light on the gold substrate covered with

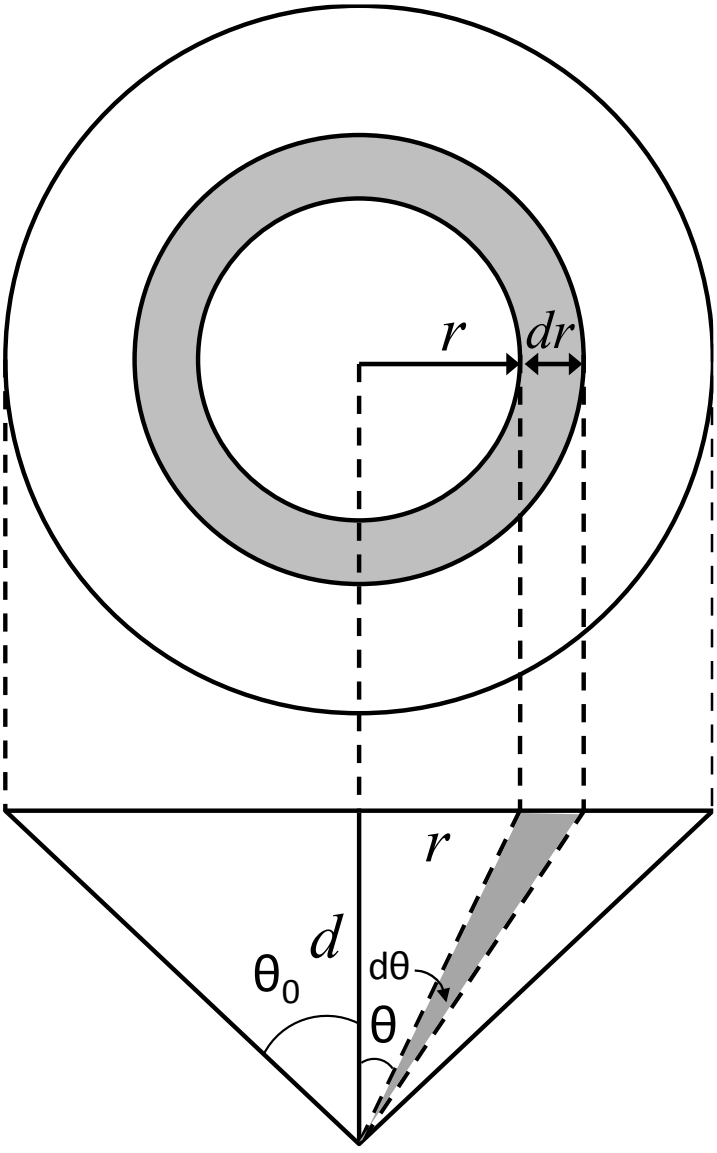

Figure 3.12 top: diagram showing the incident aperture of the objective lens (top view); bottom: schematic showing the focusing cone of light. The correspondence between the incident annular ring and the focusing cone is indicated by filled grey areas

a graphene flake. The measured spectra are then compared to calculations based on a revised theoretical model, which takes into account proportional contributions from different incident angles of light. In order to work out the proportion of light at an incident angle θ, it is assumed that the light passing through the top aperture is uniform (figure 3.12 top). This is reasonable because the incident light is much wider than the aperture. It is also assumed that the objective acts as an effective lens, with a numerical aperture of 0.9. This gives a simplified picture of light passing though the aperture between r and $r + dr$ being focused onto the sample through a range of angles between θ and $\theta + d\theta$. The amount of light here will be proportional to the area of the annular ring which is given by:

$$dA = 2\pi r dr \tag{3.4}$$

$$r = d\tan\theta \tag{3.5}$$

where d is the focusing distance. When equation 3.4 and 3.5 are combined, the result gives:

$$dA = 2\pi d^2 \tan\theta(\sec\theta)^2\, d\theta \tag{3.6}$$

The reflectivity of singularly polarised light (either TE or TM) is calculated by:

$$\bar{R} = \frac{\int_0^{\theta_0} R(\theta) 2\pi d^2 \tan\theta(\sec\theta)^2 d\theta}{A_0} \tag{3.7}$$

where $R(\theta)$ is the reflectivity at an angle θ, and A_0 is the total area of the incident aperture of the objective lens (top circle of figure 3.12) given by:

$$A_0 = \pi d^2 (\tan \theta_0)^2 \tag{3.8}$$

where θ_0 is the maximum incident angle, which is decided by the numerical aperture of the objective lens ($\sin \theta_0 = NA$). This gives a value of 64° for the 100x objective lens used in these experiments. Inserting equation 3.8 into equation 3.6 gives:

$$\bar{R} = \frac{2 \int_0^{\theta_0} R(\theta) \tan \theta (\sec \theta)^2 d\theta}{(\tan \theta_0)^2} \tag{3.9}$$

Non-polarised light was used during the experiments, so if it's assumed there was an equal contribution from both the transverse-electric (TE) and transverse-magnetic (TM) polarisations, the averaged calculated reflectivity is then given by:

$$R_{av} = \frac{1}{2} (\bar{R}_{TE} + \bar{R}_{TM}) \tag{3.10}$$

where $\bar{R}_{TE}$ and $\bar{R}_{TM}$ are given by equation 3.9.

For the simulations, the thickness of graphene is given by d = 0.335N nm, where N is the number of layers. The refractive index of graphene was taken as 2.6-1.3*i*, the same as that of graphite, which has been shown to produce consistent simulation results with experiments[20,21]. This assumption is not accurate in reality since graphene's refractive index varies with wavelength. This difference is however more pronounced in the short wavelength range[22,23], and so the assumption is sufficient for the range used in these experiments. The refractive index of Au is adopted from literature[24].

Contrast spectroscopy has been previously used to measure graphene flake thickness on Si/SiO_2 substrates[25]. It was observed that the contrast was positive (negative) when the graphene reduces (increases) the reflectance of light on the gold substrate. Positive contrast was observed on flakes up to ten layers, while it is negative on thicker flakes (figure 3.13):

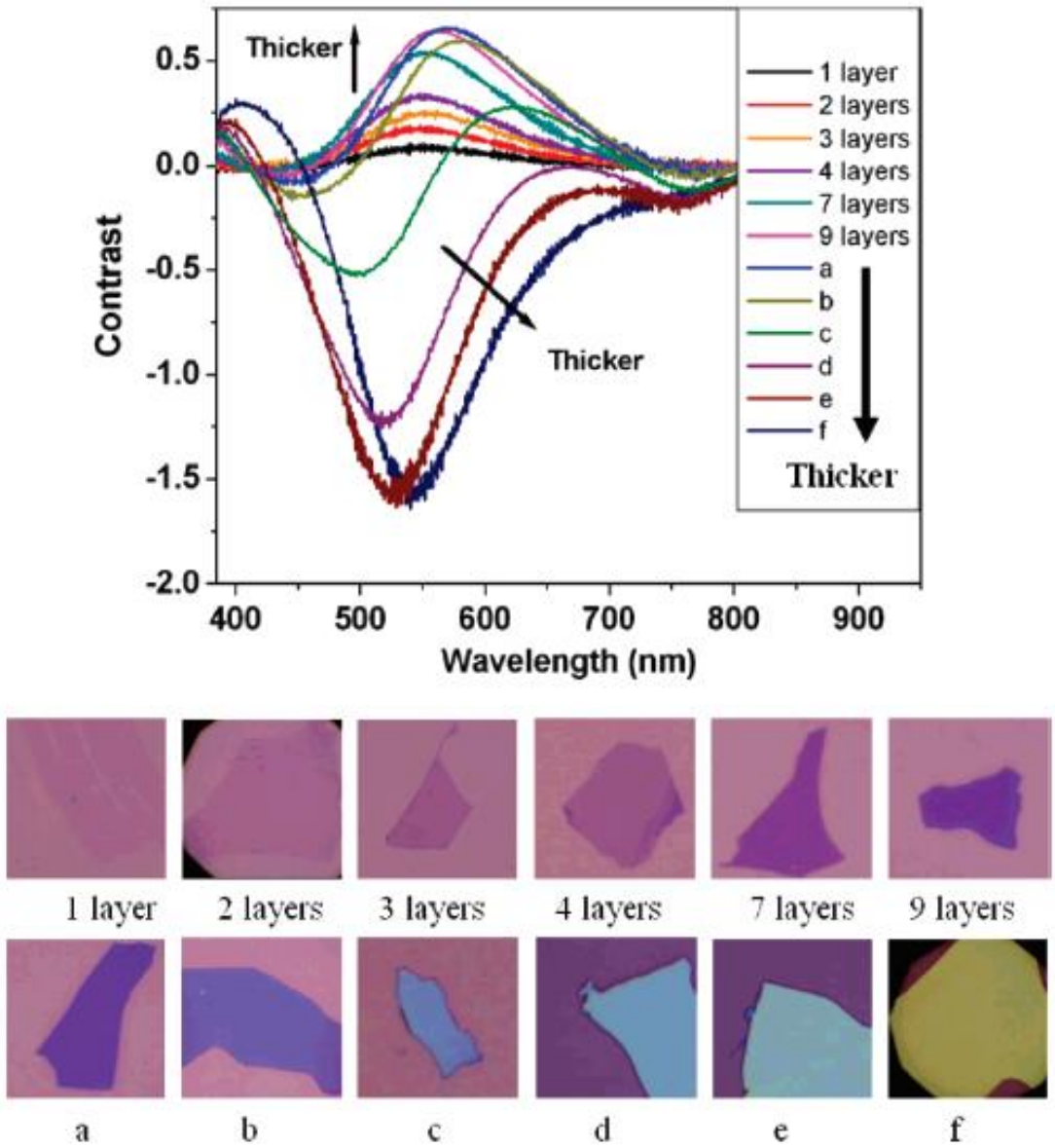

Figure 3.13 Contrast spectra for graphene sheets of different thicknesses, along with corresponding optical images. Samples a-f are more than 10 layers in thickness, with the thickness increasing from a to f[25]

3.6 References

1. Kelly, P.J. & Arnell, R.D., *Magnetron sputtering: a review of recent developments and applications*, Vacuum 56, no. 3 (2000): 159-172
2. Yang, T.L. et al., *Transparent conducting ZnO: Al films deposited on organic substrates deposited by rf magnetron-sputtering*, Thin Solid Films 326, no. 1-2 (1998): 60-62
3. Pierson, J.F., Wiederkehr, D. & Billard, A., *Reactive magnetron sputtering of copper, silver, and gold*, Thin Solid Films 478, no. 1-2 (2005): 196-205
4. Maurya, D., Sardarinejad, A. & Alameh, K., *Recent developments in RF magnetron sputtered thin films in pH sensing applications – an overview*, Coatings 4, no. 4 (2014): 756-771
5. Jaeger, D.A., *Interface investigations on titanium nitride bilayer systems*, PhD thesis, École Polytechnique Fédérale de Lausanne (2012)
6. Longrie, D., *Atomic layer deposition for surface engineering of powders*, PhD thesis, Ghent University (2013)
7. Birkholz, M., *Thin Film Analysis by X-Ray Scattering*, chapter 4, page 170, Wiley-VCH, 2006
8. Lee, Y.J. et al., *Ultrasmooth, highly spherical monocrystalline gold particles for precision plasmonics*, ACS Nano 7, no. 12 (2013): 11064-11070
9. Dietrich, H.R.C. et al., *Tethered particle motion mediated by scattering from gold particles and darkfield microscopy*, Journal of Nanophotonics 3, no. 1 (2009): 031795
10. Zou, J. et al., *In situ study of Li intercalation into highly crystalline graphitic flakes of varying thickness*, The Journal of Physical Chemistry Letters 7, no. 21 (2016): 4291-4296
11. Chen, S. et al., *Raman measurements of thermal transport in suspended monolayer graphene of variable sizes in vacuum in gaseous environments*, ACS Nano 5, no. 1 (2010): 321-328

12. Malard, L.M., Pimenta, M.A.A., Dresselhaus, G. & Dresselhaus, M.S., *Raman spectroscopy in graphene*, Physics Reports 473, no. 5 (2009): 51-87
13. Hao, Y. et al., *Probing layer number and stacking order and few-layer graphene by Raman spectroscopy*, Small 6, no. 2 (2010): 195-200
14. Das, A., Chakraborty, B. & Sood, A.K., *Raman spectroscopy of graphene on different substrates and influence of defects*, Bulletin of Materials Science 31, no. 3 (2008): 579-584
15. Bertrand, P.A., *Surface-phonon dispersion of MoS_2*, Physical Review B 44, no. 11 (1991): 5745
16. Wang, Y., Cong, C., Qiu, C. & Yu, T., *Raman spectroscopy study of lattice vibration and crystallographic orientation of monolayer MoS_2 under uniaxial strain*, Small 9, no. 17 (2013): 2857-2861
17. Li, H. et al., *From bulk to monolayer MoS_2: evolution of Raman scattering*, Advanced Functional Materials 22, no. 7 (2012): 1385-1390
18. Lee, C. et al., *Anomalous lattice vibrations of single- and few-layer MoS_2*, ACS Nano 4, no. 5 (2010): 2695-2700
19. Matković, A. et al., *Influence of a gold substrate on the optical properties of graphene*, Journal of Applied Physics 117, no. 1 (2015): 015305
20. Wlasny, I., Dabrowski, P. & Klusek, Z., *Optical contrast of single- and multi-layer graphene deposited on a gold substrate*, arXiv:1102.4953
21. Blake, P. et al., *Making graphene visible*, Applied Physics Letters 91, no. 6 (2007): 63124-63127
22. Wang, X., Chen, Y.P. & Nolte, D.D., *Strong anomalous optical dispersion of graphene: complex refractive index measured by Picometrology*, Optics Express 16, no. 26 (2008): 22105-22112
23. Falkovsky, L.A., *Optical properties of graphene*, Journal of Physics: Conference Series 129, no. 1 (2008): 012004

24. Rakić, A.D., Djurišic, A.B., Elazer, J.M. & Majewski, M.L., *Optical properties of metallic films for vertical-cavity optoelectronic devices*, Applied Optics 37, no. 22 (1998): 5271-5283
25. Ni, Z.H. et al., *Graphene thickness determination using reflection and contrast spectroscopy*, Nano Letters 7, no. 9 (2007): 2758-2763

Chapter 4

Tuning plasmonic response through optical properties of the substrate

4.1 Introduction

The interaction of light with plasmonic nanoparticles has been studied in some detail[1-3]. The NPoM geometry, which is used for many applications such as photocatalysis, sensors and antennas[4-8], is of particular interest. This is because a particle near a mirrored substrate is able to induce strong image charges to which the particle couples. This gives rise to strong plasmons in the gap between the particle and substrate, thereby creating a well-defined hotspot that provides the large enhancement required for applications. It is important to understand the fundamentals of such a system so that it can be used to its full potential. One way that this can be investigated is to change the thickness of the underlying film. This is because a changing thickness in thin films will affect their optical properties (reflectivity and permittivity)[9-11]. These properties determine the strength of image charges induced in the film and can influence the plasmonic mode's intensity, as well as its resonance by up to hundreds of nanometres[12-14].

In this chapter, the coupling interaction between light and a particle on a substrate is examined by measuring the dark-field scattering of 90 nm gold particles on gold films which vary in thickness from 0 to 100 nm. It is determined how the transverse, vertical dipole (sometimes called the "virtual" mode since it principally arises from hybridisation between film and particle plasmons when the supporting films are very thin[15]) and gap dipole plasmon

modes are affected. The influence from the underlying substrate was also investigated by examining nanoparticles on gold films supported by bulk dielectric (SiO_2) or semiconductive (p-type boron doped Si) substrates. It is demonstrated that on SiO_2, the vertical dipole mode can actively be tuned by changing the gold film thickness, while the transverse mode also shifts due to interaction with the increasingly thick film. Conversely, neither peak shifts much on increasing Au thickness on the Si substrates, except due to hybridisation with plasmons in the substrate. It is expected that as the particle is moved further from its image charges, the plasmonic resonance should blue shift[16]. However, in the visible spectrum silicon has a strong permittivity and reflectivity, and so can support strong image charges, giving rise to a vertical dipole. Since the image charges remain sufficiently strong as the gold film gets thicker, there is little shift in the resonance wavelength of either mode, except on the 5 nm Au film as compared to bulk Si. Furthermore, a small gap plasmon mode can be seen on Si samples since its reflectivity sufficiently strong interaction between charges in the particle and image charges in the substrate.

In addition to changes in the resonant wavelengths, the intensity is also investigated. This is due to the substrate's reflectivity being sensitive to its thickness[17]. The higher the reflectivity, the stronger the image charges induced in the substrate, which leads to stronger vertical coupling. This is especially relevant to the particles examined on SiO_2, which is transparent. Conversely, substrate reflectivity can also lead to interactions between charges that interfere destructively in the horizontal orientation, thereby causing a decrease of the intensity.

This aspect of the plasmonic response has been investigated previously, using geometries such as nanodisk-film interactions[18], tip-film interactions[15], and several times theoretically with gold nanospheres on substrates[19,20]. However, no studies have examined experimentally perfectly spherical gold

nanoparticles, which gives an opportunity to rigorously compare theory to real situations. Furthermore, this experiment unambiguously identifies the origin of each of the scattering resonant modes from a NPoM, and gives another way of tuning their plasmonic resonance and intensity, thereby optimising it for use in applications.

4.2 Sample preparation

Samples were prepared with magneton sputtering as described in chapter 3. Samples of 4.3, 6.9, 9.4, 11.8, 14.9 and 26.4 nm Au on 93 nm SiO_2/10 nm Ti/bulk Si, and 0, 5, 10, 20, 30, 40 and 50 nm Au on 10 nm Ti/0.2 nm native SiO_2/bulk p-type boron doped Si were prepared. The thicknesses of these films were verified using XRR measurements. 90 nm Au ultrasmooth particles were drop cast on top, then rinsed with deionised water and dried with compressed air.

The samples were examined with an optical microscope (Olympus BX51) and had their dark-field scattering spectra measured through an optical spectrometer. Ten particles were selected and had three spectra measured each. The results were then averaged.

4.3 Results

4.3.1 Silicon oxide substrate

Initially, once the particles were deposited onto the substrates, they were examined optically in dark-field mode (figure 4.1). Although the particles do not change much in colour, a slight red halo can be seen around the particle on 100 nm gold where vertical image dipoles are supported. It appears as a

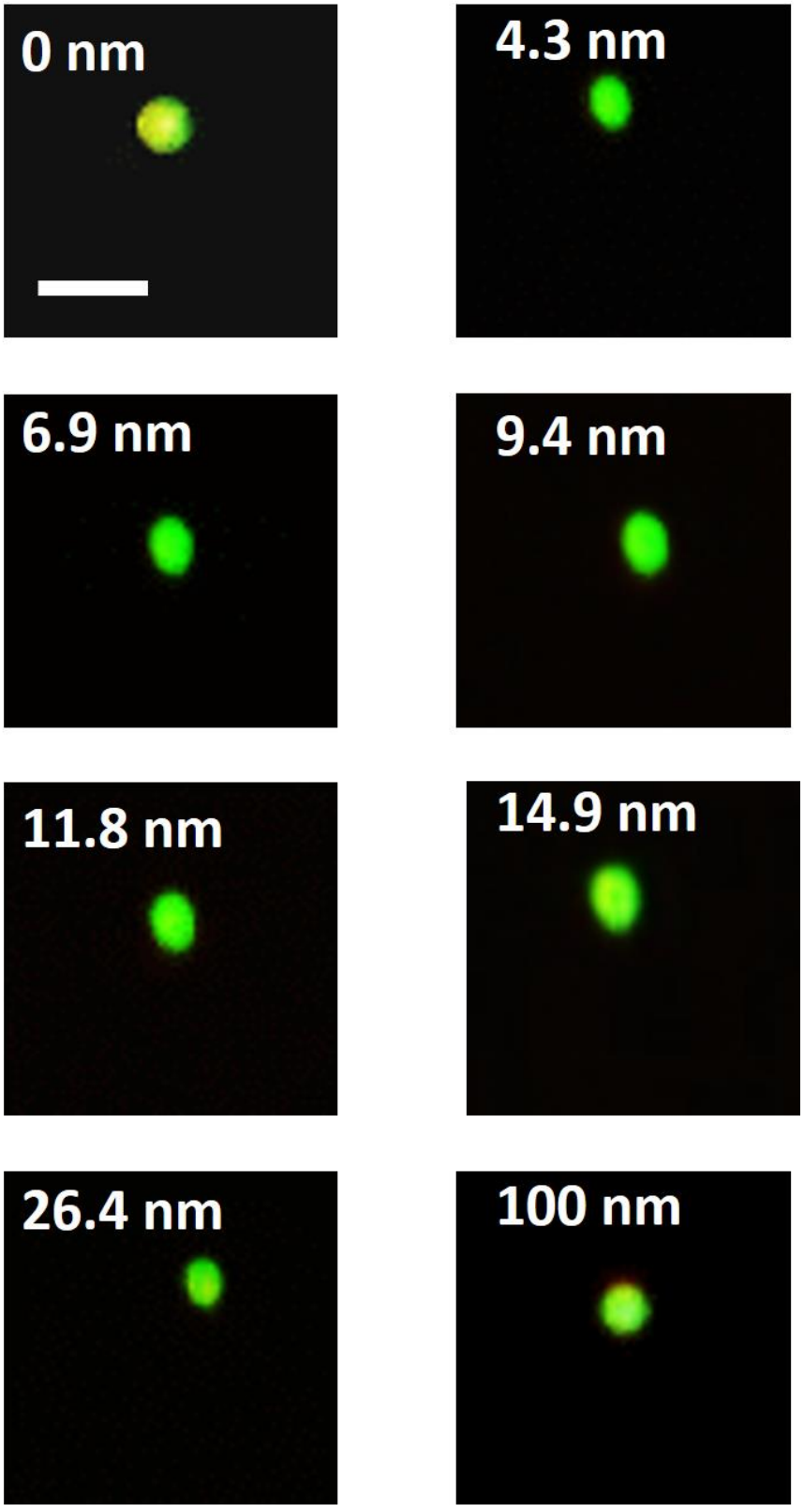

Figure 4.1 Optical dark-field images of 90 nm Au NPs on Au films of thickness ranging from 0 to 100 nm on 93 nm SiO_2/10 nm Ti/bulk Si substrates. Images were taken with a 100× magnification objective (NA=0.9). Scale bar represents 0.8 μm

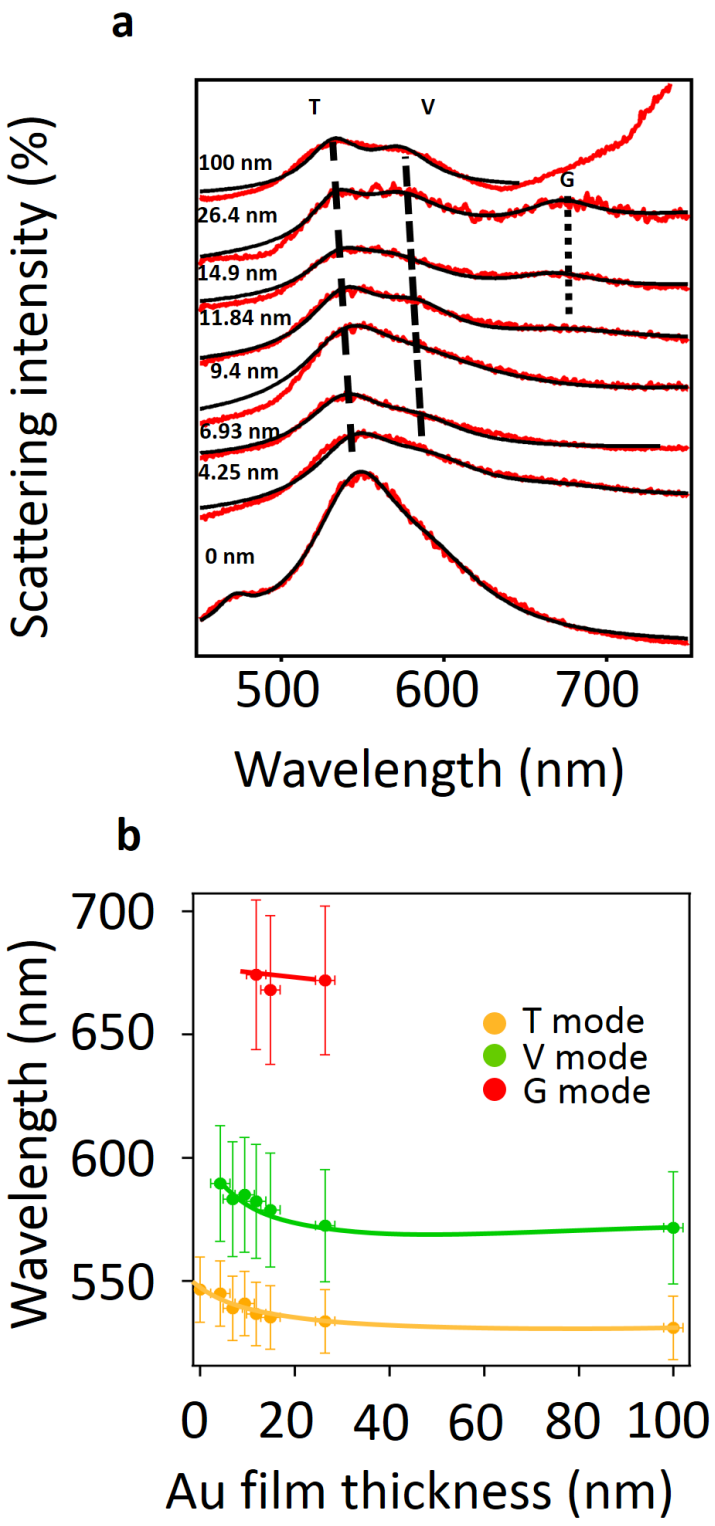

Figure 4.2 (a) Scattering spectra measured for 90 nm Au particles on Au films of thickness 0, 4.3, 6.9, 9.4, 11.8, 14.9, 26.4 and 100 nm on SiO_2. Measured data is given in red while Lorentzian fitted data is given in black. (b) Graph showing how the (orange) transverse, (green) vertical, and (red) gap modes change with Au film thickness

weak halo because it cannot be effectively picked up by the CCD camera[21] and the transverse mode is strong. For further analysis, the scattering spectra of the corresponding optical images were measured (figure 4.2a). This revealed a number of resonant modes, which vary with the optical properties of the substrate. In order to help identify all of the resonant modes, the spectra were fitted with Lorentzian peaks. Not only do these peaks give good estimates about the resonant wavelength positions, but they also give estimates about their peak intensities and FWHMs. The spectra show only one peak on the bare SiO_2 at around 550 nm. This must therefore be the horizontal transverse mode, since SiO_2 is transparent and cannot support image charges or surface plasmons. There is, however, a breaking of the dielectric environment around the particle, which causes a shift in the particle's resonance from if it was free standing in free space[22]. Then, as the Au film gets thicker, a second weak mode starts to grow. This is because the reflectivity of the substrate increases with thickness, since thicker metals have more electrons which reflect the light rather than let it transmit through[23]. This stronger reflectivity leads to stronger image charges to which the particle can couple more efficiently.

Furthermore, since gold is plasmonic, there is also hybridisation between plasmons in the particle and the substrate[24,25]. Although stronger interaction with image charges results in red shifting of the resonance (in an analogous way to coupled dipoles[26]), hybridisation can either blue or red shift the resonance, depending on the wavelength of the bonding film plasmons. It is the combination of image charges and hybridisation from which the vertical mode is formed. Previous results[20] have shown that the film continuum band of plasmons shifts to higher energies as the film gets thicker, resulting in a blue shift in the vertical mode. It is also notable that the transverse mode slightly blueshifts, which is unexpected since it is principally due to nanoparticle plasmons and should not be affected by substrate thickness. This results from

two hybridisation effects. Firstly, the particle's plasmons hybridise with short-wavelength film plasmons (which do not depend much on film thickness[19]), thereby weakly shifting the plasmonic resonance. Secondly, on thin gold films, plasmons at the gold/air boundary strongly interact with plasmons at the gold/SiO_2 boundary, leading to strong repulsion between the transverse and vertical modes. Then, as the gold film gets thicker, interaction between the plasmons at the two boundaries decreases, resulting in less repulsion and therefore a blueshift in both modes[20].

An additional mode is starts to emerge on 11.84 - 26.4 nm gold films, at around 670 nm. This is the gap mode, so called because the plasmon is localised to the region between the particle and the film's planar surface. It arises from charges accumulating at the bottom of the nanoparticle, which induce opposite charges in the film[27-29]. However, its resonance does not shift with changing film thickness. This is because the gap mode is sensitive to the coupling strength between charges in the particle and its images in the film[30], which does not change much at the thicknesses examined here, so no resonant shift is observed.

It is also interesting to note how the intensity of the modes changes as the gold film gets thicker (figure 4.3). There is a decrease in intensity of the transverse mode as the gold film increases, because the dipole produced from the induced image charges is aligned in the opposite direction and causes destructive interference (see figure 2.9a). Meanwhile, the vertical mode

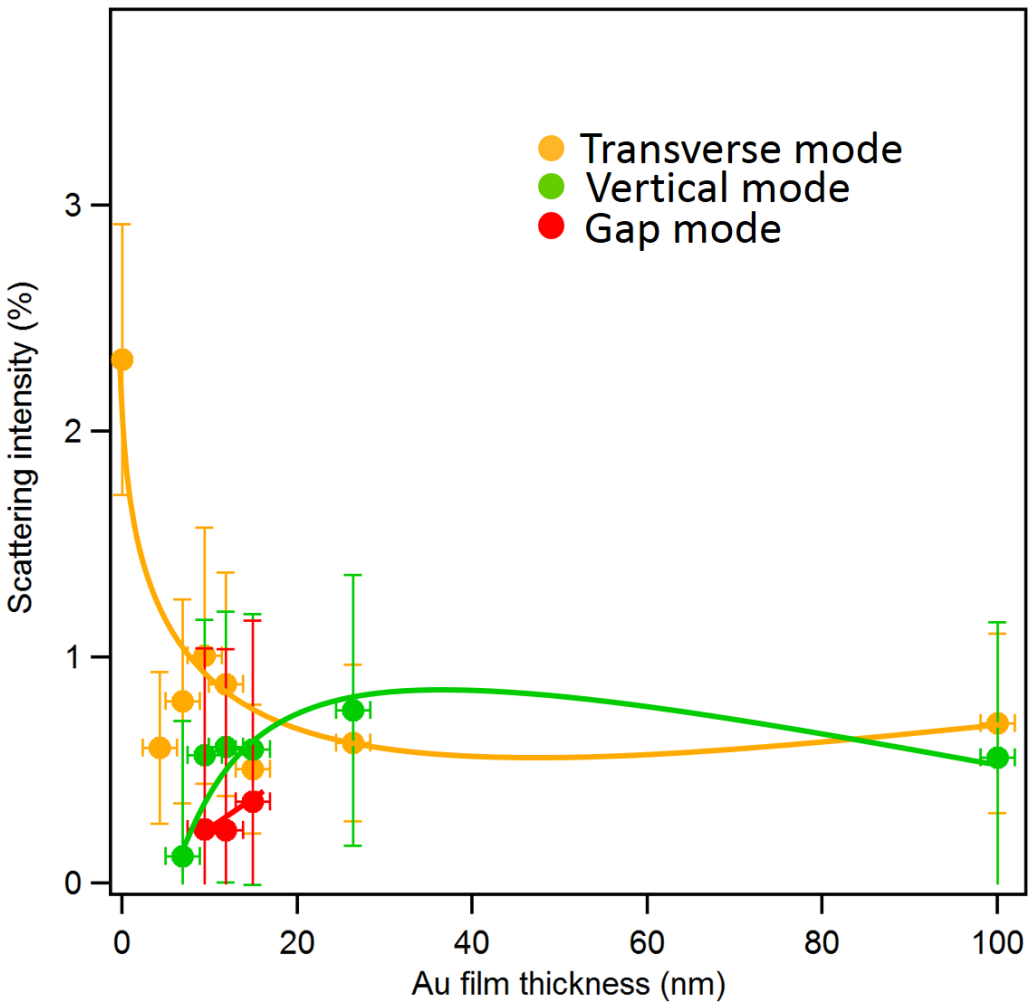

Figure 4.3 Graph showing how the intensities of the (orange) transverse, (green) vertical, and (red) gap modes changes with Au film thickness

increases in intensity, because the induced vertical dipole is aligned in the same direction, causing constructive interference (see figure 2.9b). Similarly, the gap mode increases gradually with film thickness. As the substrate reflectivity increases, stronger image charges form in the gap region, to which the particle charges strongly interact. Since there is such a large amount of charge in the region, a stronger interaction between the charges leads to a large electric field in the region, which also gives rise to field enhancements.

4.3.2 P-type boron-doped silicon substrate

When the gold films are supported by a silicon substrate, a very different relationship is observed from those on SiO_2 (figure 4.4).

Optically, the particles on the 0-10 nm gold samples have distinctive red colours. This is because, unlike SiO_2, silicon has a substantial reflectivity at visible wavelengths (~45%)[31]. And so, it can support strong image charges. In fact, on the bare silicon substrates, the particle displays a doughnut shape, with a void surrounded by a bright spot. This is indicative of a strong vertical dipole, which has weak radiation along the particle's central axis, but strong radiation surrounding the central axis[32] (see figure 2.9b). This is confirmed in the scattering spectra (figure 4.5) which show that the vertical mode dominates over the horizontal and gap modes. As the particle is moved away from the silicon, the particle couples less to its image dipole, and vertical polarisation gets weaker, causing the doughnut shape to disappear and the vertical peak to get weaker. The transverse mode conversely starts to dominate as the particle is moved away from its destructive image dipole, and the particle starts to turn greener optically. The data also shows that the gap plasmon redshifts and grows in intensity as the gold film gets thicker, dominating the spectrum on 50 nm gold. Optically, however, it can only be seen as a red halo around a green/yellow particle.

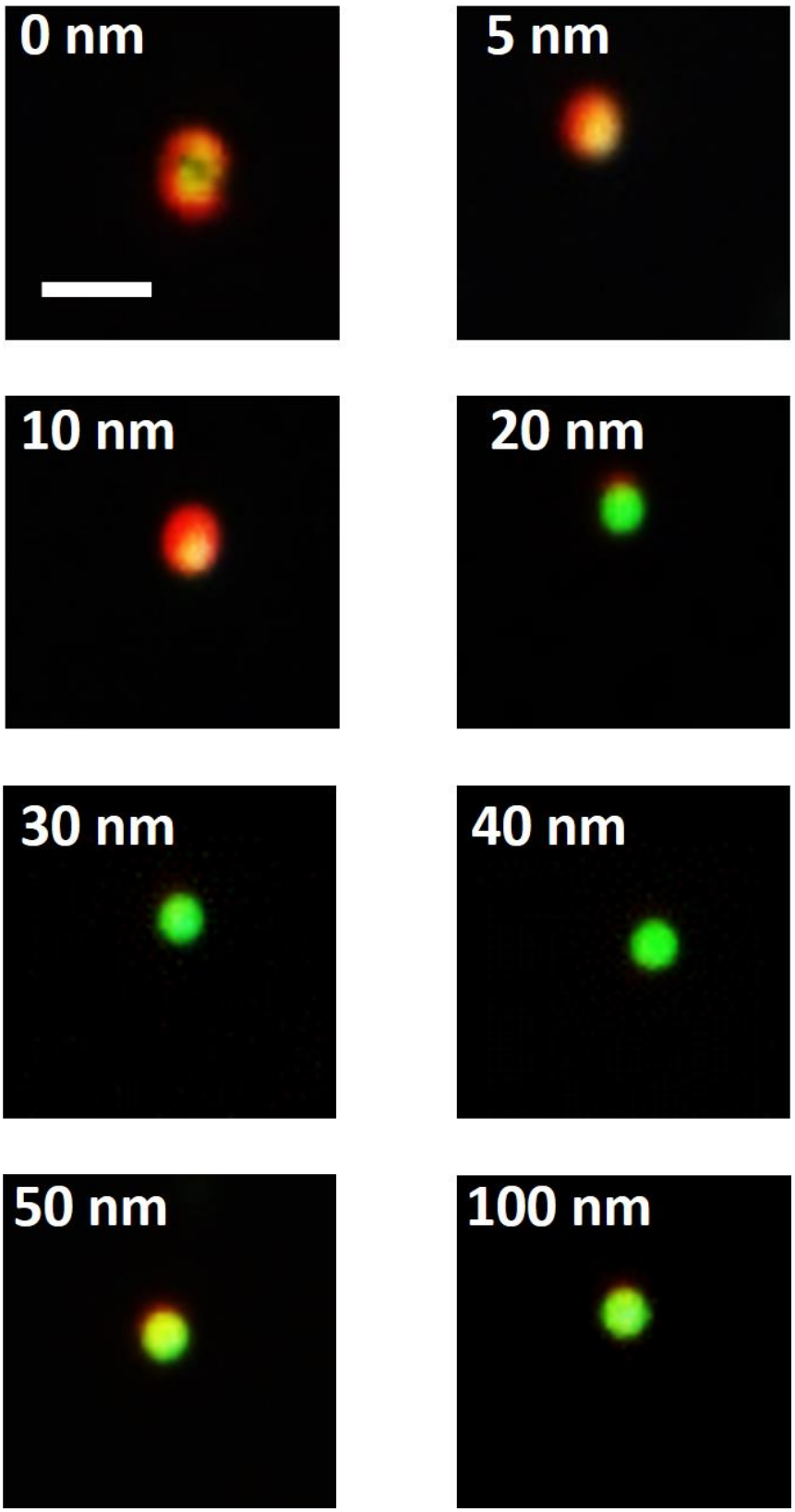

Figure 4.4 Optical dark-field images of Au NPs on Au film of thickness ranging from 0 to 100 nm on Si substrates. Scale bar represents 0.8 μm

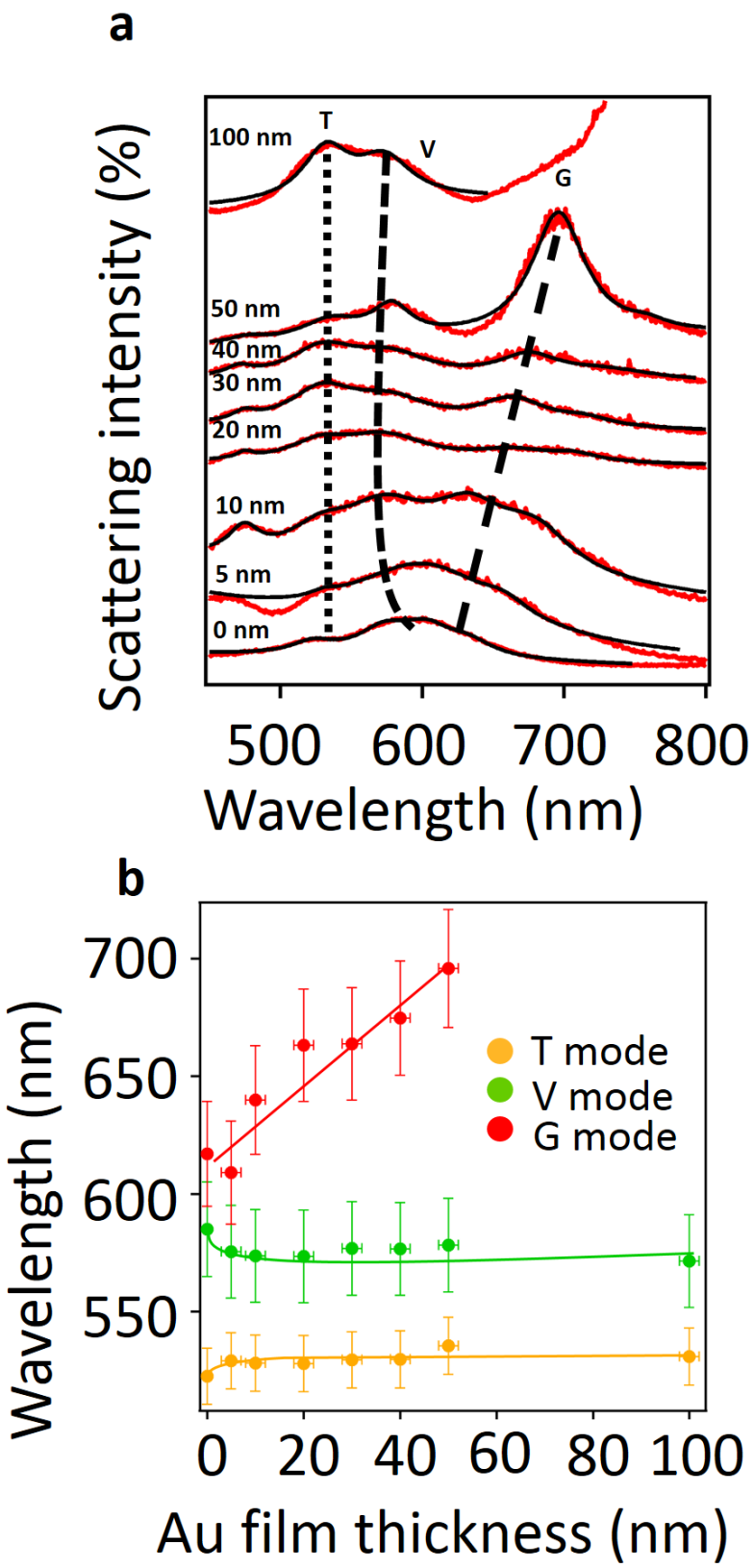

Figure 4.5 (a) Scattering spectra measured from 90 nm Au particles on Au films of 0, 5, 10, 20, 30, 40, 50 and 100 nm on Si. (b) Graph showing how the (orange) transverse, (green) vertical, and (red) gap modes change with increasing Au film thickness

This is due to the sensitivity of the microscope camera[32]. If the quantum efficiency curves are examined (figure 4.6), it can be seen that there is a strong sensitivity in the 500-580 nm green region, while the red sensitivity is restricted in the region of 580-630 nm. In the region around 690 nm, where a strong peak is observed in the scattering spectrum, all colour sensors have very low quantum efficiencies. This means that the strong red scattering is not efficiently collected by the camera. Since the transverse and vertical modes still have a sufficiently strong intensity in the 530-580 nm region (where there is a strong green quantum efficiency), this appears as the dominant colour, with a red halo. This gives the particle a weak doughnut appearance, which indicates the vertical nature of this mode. It should also be taken into consideration that the human eye itself is more sensitive to green than red or blue, thereby giving limitations to how optical examination can be used for plasmonic resonance.

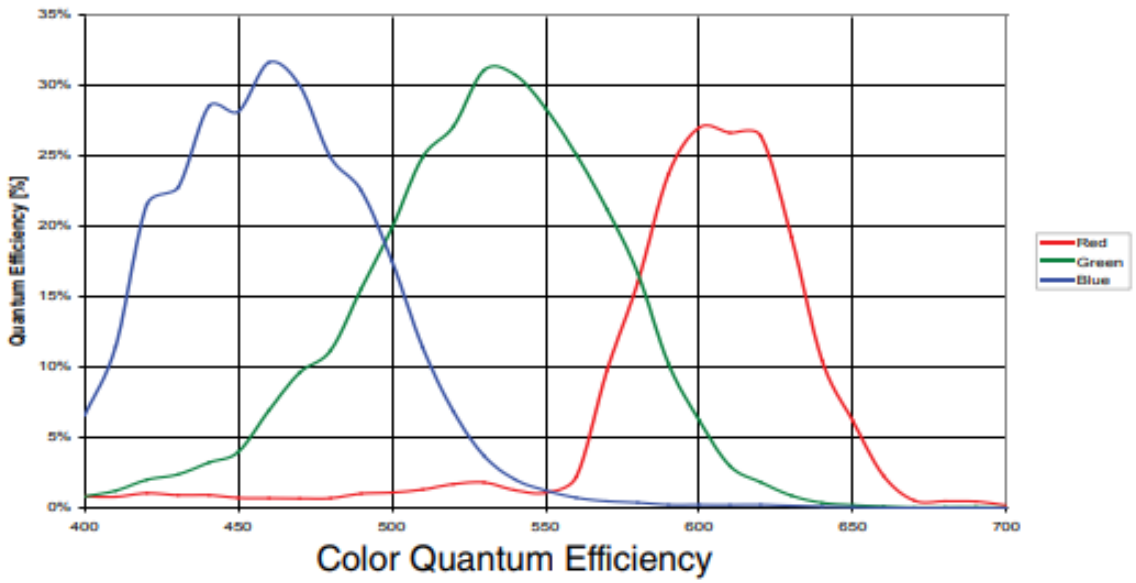

Figure 4.6 Colour quantum efficiency for an Infinity 2 CCD camera[33]

Finally, on 100 nm gold film, the transverse mode increases in intensity with respect to the virtual mode.

Another difference here from the SiO_2 data is that neither the vertical mode nor the transverse mode shift much on the gold films as thickness increases. Initially, the vertical mode blue shifts on the 5 nm Au film, which is consistent with the Au/SiO_2 experiments. On the thicker gold films, the resonant wavelengths are in similar positions to those from 26.4 nm Au/SiO_2 (530 and 575 nm respectively) and do not shift much. This is because at these thicknesses, the gold films can be considered as being bulk, and therefore their reflectivity reaches its peak value and stops increasing with thickness. It is also important to note that the gold films examined here are mostly at intermediate thickness ($\gtrsim$ 15 nm). In this regime, many of the film plasmons have shifted

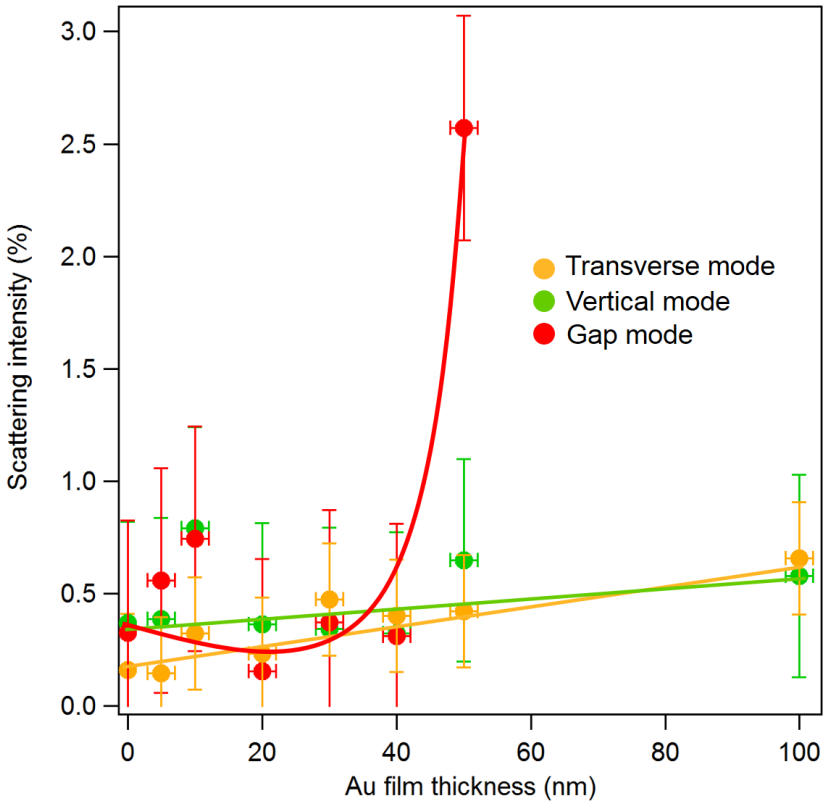

Figure 4.7 Graph showing how the absolute scattering intensities of the (orange) transverse, (green) vertical, (red) and gap modes change with Au film thickness on a Si substrate

away from the resonance of the particle plasmons, resulting in less hybridisation[19]. This prevents any more shift in the transverse and vertical modes.

There is more of a significant change in the intensity of these modes (figure 4.7) due to an increase in the separation between charges in the particle and their image dipoles in the silicon. This initially increases the horizontal dipole mode intensity with respect to the vertical mode up to about 30 nm as the destructive interference with its image charges decreases. But then, as the gold film starts to get thicker, image charges start to form there to which the particle couples instead, causing the vertical mode to grow again.

It is interesting to note how different the scattering spectrum looks for the particles on silicon (figure 4.8), despite it having a similar real part of its

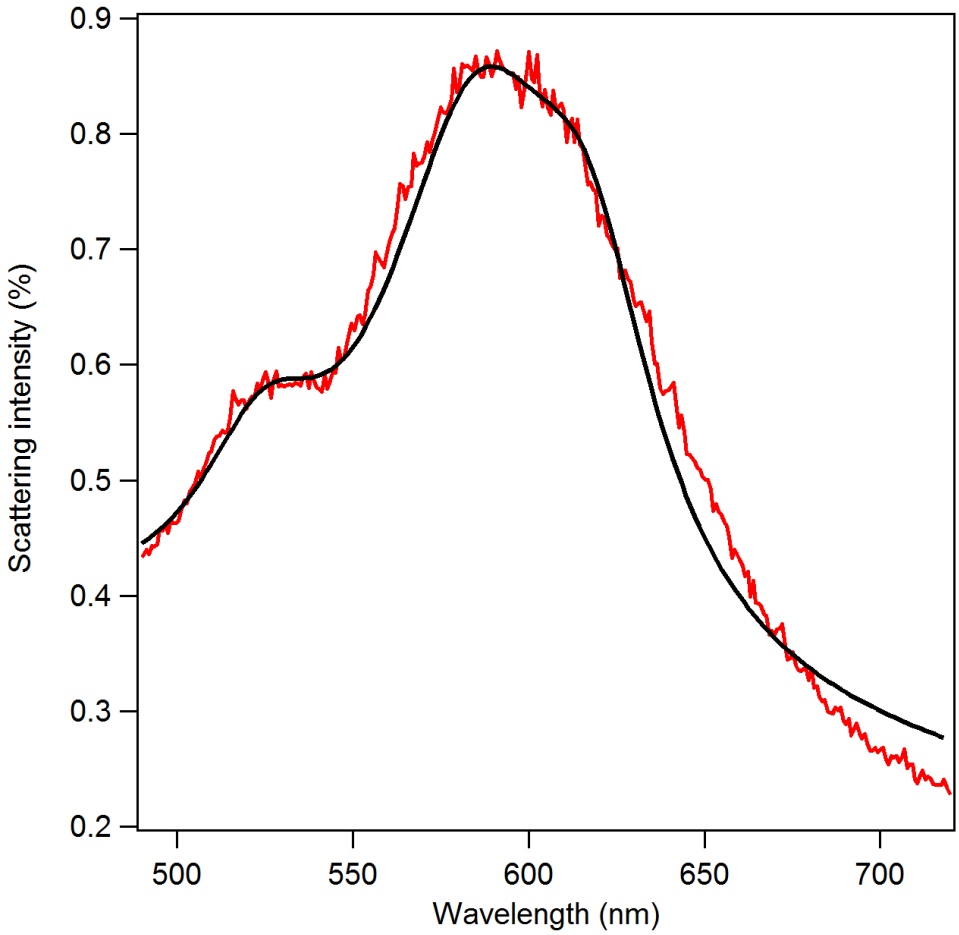

Figure 4.8 Scattering spectrum of a 90 nm Au NP on a bare silicon substrate. Black line represents the Lorentzian fit

permittivity (≈16.1 at its resonant wavelength 570 nm) as bulk gold (≈14.1 at its resonant wavelength 668 nm). A broad peak can be seen at ~600 nm, and Lorentzian fitting (black line in figure 4.8) suggests that it is composed of two peaks; the vertical dipole (~584 nm) and gap modes (~617 nm), with the vertical gap mode dominating. It is also notable that each mode has a larger FWHM (~30 and ~37 nm respectively) than their counterparts on bulk gold (~20 and ~30 nm respectively). The gap mode is also noticeably different. This relates to a difference in the reflectivity of gold and silicon. Although silicon has a reflectivity substantial enough to support vertical image coupling, bulk gold has a much larger value in the wavelength regime of interest (~100% for ≥500 nm)[36]. Since the gap mode relates to the coupling strength between plasmons in different systems[37-39], a redshift in the resonance is observed on thicker gold films as coupling between charges in the gap increases, as with a dipole. The increased coupling and plasmonic nature of the gold film also gives a further enhancement to the gap mode, which results in a much larger intensity on the 50 nm sample.

4.4 Conclusions

The origin of the resonant modes observed in scattering spectra of 90 nm gold particles in the NPoM geometry has been investigated. This was achieved by looking at scattering spectra of particles on gold substrates of increasing thickness, and hence reflectivity. Three modes on thick gold were identified as the transverse dipole, vertical dipole and gap modes. The transverse mode relates mainly to the particle itself. This is apparent because it is visible even on transparent substrates like SiO_2. It therefore only shifts due to weak hybridisation with film plasmons. It does, however, initially decrease significantly in intensity on thick gold samples as a result of destructive interference with its image dipole. Conversely, the vertical dipole requires a substrate that can support strong image charges to which the particle can

couple. It can be seen on bulk Si and thicker gold substrates (≥10 nm). When interaction with the vertical image dipole is strong on highly reflective films, constructive interference leads to very strong modes, while hybridisation with the gold film's bonding plasmons lead to a blueshift with Au film thickness. The gap mode arises because the lightning rod effect means that much of the nanoparticle's charges are located in the gap region. Results show that it also requires large coupling with image charges, and is therefore only visible on very reflective films. It grows in intensity and redshifts as the Au film gets thicker and interactions with charges and image charges in the gap increases, in an analogous way to a dipole.

These results not only provide an important insight into the fundamentals of the NPoM geometry, but provide a new way in which its plasmonic properties can be tuned. These experiments complement previous theoretical work, and are important for applications in which enhancement is necessary such as SERS and TERS.

4.5 References

1. Fan, X., Zheng, W. & Singh, D.J., *Light scattering and surface plasmons on small spherical particles*, Light: Science & Applications 3, number 6 (2014): e179
2. Linden, S., Kuhl, J. & Giessen, H., *Controlling the interaction between light and gold nanoparticles: selective suppression of extinction*, Physical Review Letters 86, no. 20 (2001): 4688
3. Perminov, S.V., Drachev, V.P. & Rautian, S.G., *Optics of metal aggregates with light induced motion*, Optics Express 15, no. 14 (2007): 8639-8648
4. Sigle, D.O. et al., *Ultrathin CdSe in plasmonic nanogaps for enhanced photocatalytic water splitting*, The Journal of Physical Chemistry Letters 6, no. 7 (2015): 1099-1103

5. Cobley, C.M., Skrabalak, S.E., Campbell, D.J. & Xia, Y., *Shape-controlled synthesis of silver nanoparticles for plasmonic and sensing applications*, Plasmonics 4, no. 2 (2009): 171-179
6. Muehlschlegel, P. et al., *Resonant optical antennas*, Science 308, no. 5728 (2005): 1607-1609
7. Stranik, O., McEvoy, H.M., McDonagh, C. & MacCraith, B.D., *Plasmonic enhancement of fluorescence for sensor applications*, Sensors and Actuators B: Chemical 107, no. 1 (2005): 148-153
8. Akimov, Y.A., Ostrikov, K. & Li, E.P., *Surface plasmon enhancement of optical absorption in thin-film silicon solar cells*, Plasmonics 4, no. 2 (2009): 107-113
9. Parker, C.B., Maria, J.P. & Kingon, A.I., *Temperature and thickness dependent permittivity of (Ba, Sr) TiO_3 thin films*, Applied Physics Letters 81, no. 2 (2002): 340-342
10. Yakubovsky, D.I. et al., *Optical constants and structural properties of thin gold films*, Optics Express 25, no. 21 (2017): 25574-25587
11. Atwater, H.A., *The promise of plasmonics*, Scientific American 296, no. 4 (2007): 56-62
12. Jiang, G. et al., *Signal enhancement and tuning of surface plasmon resonance in Au nanoparticle/polyelectrolyte ultrathin films*, The Journal of Physical Chemistry C 111, no. 50 (2007): 18687-18694
13. Hu, M., Ghoshal, A., Marquez, M. & Kik, P.G., *Single particle spectroscopy study of metal-film-induced tuning of silver nanoparticle plasmon resonances*, The Journal of Physical Chemistry C 114, no. 16 (2010): 7509-7514
14. Stuart, H.R. & Hall, D.G., *Enhanced dipole-dipole interaction between elementary radiators near a surface*, Physical Review Letters 80, no. 25 (1998): 5663

15. Uetsuki, K., Verma, P., Nordlander, P. & Kawata, S., *Tunable plasmon resonances in a metallic nanotip-film system*, Nanoscale 4, no. 19 (2012): 5931-5935
16. Hill, R.T. et al., *Leveraging nanoscale plasmonic modes to achieve reproducible enhancement of light*, Nano Letters 10, no. 10 (2010): 4150-4154
17. Oloomi, S.A.A., Saboonchi, A. & Sedaghat, A., *Effects of thin film thickness on emittance, reflectance and transmittance of nano scale multilayers*, International Journal of Physical Sciences 5, no. 5 (2010): 465-469
18. Wang, Y. et al., *Substrate-mediated charge transfer plasmons in simple and complex nanoparticle clusters*, Nanoscale 5, no. 20 (2013): 9897-9901
19. Le, F. et al., *Plasmons in the metallic nanoparticle-film system as a tunable impurity problem*, Nano Letters 5, no. 10 (2005): 2009-2013
20. Miljkovic, V.D., Shegai, T., Käll, M. & Johansson, P., *Mode-specific directional emission from hybridised particle-on-a-film plasmons*, Optics Express 19, no. 14. (2011): 12856-12864
21. Yu, B., Woo, J., Kong, M. & O'Carroll, D.M., *Mode-specific study of nanoparticle-mediated optical interactions in an absorber/metal thin film system*, Nanoscale 7, no. 31 (2015): 13196-13206
22. Chen, H. et al., *Effect of the dielectric properties of substrates on the scattering patterns of gold nanorods*, ACS Nano 5, no. 6 (2011): 4865-4877
23. Lugolole, R. & Obwoyo, S.K., *The effect of thickness of aluminium films on optical reflectance*, Journal of Ceramics 2015 (2015)
24. Swanglap, P. et al., *Seeing double: coupling between substrate image charges and collective plasmon modes in self-assembled nanoparticle superstructures*, ACS Nano 5, no. 6 (2011): 4892-4901
25. Nordlander, P. & Prodan, E., *Plasmon hybridisation in nanoparticles near metallic surfaces*, Nano Letters 4, no. 11 (2004): 2209-2213

26. Knight, M.W. et al., *Substrates matter: influence of an adjacent dielectric on an individual plasmonic nanoparticle*, Nano Letters 9, no. 5 (2009): 2188-2192
27. Lei, D.Y. et al., *Revealing plasmonic gap modes in particle-on-film systems using dark-field spectroscopy*, ACS Nano 6, no. 2 (2012): 1380-1386
28. Downes, A., Salter, D. & Elfick, A., *Finite element simulations of tip-enhanced Raman and fluorescence spectroscopy*, The Journal of Physical Chemistry B 110, no. 13 (2006): 6692-6698
29. Nothingher, I. & Elfick, A., *Effect of sample and substrate electric properties on the electric field enhancement at the apex of SPM nanotips*, The Journal of Physical Chemistry B 109, no. 33 (2005): 15699-15706
30. Chen, S.Y. et al., *Gold nanoparticles on polarisable surfaces as Raman scattering antennas*, ACS Nano 4, no. 11 (2010): 6535-6546
31. Dupré, L. et al., *Ultradense and planarised antireflective vertical silicon nanowire array using a bottom-up technique*, Nanoscale Research Letters 8, no. 1 (2013): 123
32. Mock, J.J. et al., *Distance-dependence plasmon resonant coupling between a gold nanoparticle and gold film*, Nano Letters 8, no. 8 (2008): 2245-2252
33. https://www.lumenera.com/resources/documents/datasheets/microscopy/infinity-2-1-datasheet.pdf
34. Lumdee, C. *Nanoscale control of gap-plasmon enhanced optical processes*, PhD thesis, University of Central Florida (2015)
35. Lumdee, C., Yun, B. & Kik, P.G., *Effect of surface roughness on substrate-tuned gold nanoparticle gap plasmon resonances*, Nanoscale 7, no. 9 (2015): 4255
36. Anghinolfi, L., *Self-Organized Arrays of Gold Nanoparticles: Morphology and Plasmonic Properties*, chapter 5, page 76, Springer-Verlag Berlin Heidelberg (2012)

37. Nicolas, R. et al., *Plasmonic mode interferences and Fano resonances in metal-insulator-metal nanostructured interface*, Scientific Reports 5 (2015): 14419
38. Yuan, B., Zhou, W. & Wang, J., *Novel H-shaped plasmon nanoresonators for efficient dual-band SERS and optical sensing applications*, Journal of Optics 16, no. 10 (2014): 105013
39. Li, G. et al., *Metal-substrate-mediated plasmon hybridisation in a nanoparticle dimer for photoluminescence line-width shrinking and intensity enhancement*, ACS Nano 11, no. 3 (2017): 3067-3080

Chapter 5

Optimising SERS with precisely controlled nanometre-scale gaps

5.1 Introduction

Since its discovery in 1973[1], surface-enhanced Raman scattering (SERS) has become an immensely useful sensing technology, which is widely used for the detection of small amount of substances, such as living cells, environmental pollutants and illegal drugs[2-4]. Intrinsically Raman scattering is a very weak inelastic scattering process. However, the usually weak Raman signals can be enhanced enormously with the aid of noble metal nanostructures, which can harvest the optical energy from the incident electromagnetic fields and concentrate it near the sharp edges or within interstitial nanojunctions, due to surface plasmon resonance effects. If two nanoparticles are placed very close together, plasmons from each nanoparticle will couple together. This results in very strong field enhancement being generated within the gap. When molecules are placed in this small gap where the electric field is very strong (so-called hot spots), the molecule's Raman signals will be extraordinarily enhanced, rendering the detection of small amount of molecules and even single molecules[5,6]. However, despite such extreme sensitivity has been frequently demonstrated in research, so far it is still difficult to control SERS substrates to exhibit optimal and reproducible performance.

As with many plasmonic phenomena, SERS is sensitive to a range of factors, including nanoparticle size, shape, and in particular the interparticle distance[7-9]. The electric field within the gap between two closely-positioned

nanoparticles, such as dimers, increases exponentially with decreasing gap size, until approaching very close distances (below a few nanometers) where nonlocality and quantum tunneling effects start to play significant roles[10-14]. Recently theoretical and experimental investigations suggest that quantum tunneling usually occurs at sub-nanometer scale distances[10-12], which tends to attenuate the local electric field, as a result of reduced charge density on nanoparticle surfaces due to electrons tunneling through the interparticle junction. The onset of nonlocality effect embarks at slightly larger distances around a few nanometers[13,14]. Though the nonlocality effect does not deplete the field enhancement as much as the tunneling effects, the magnitude of the field enhancement is considerably less than that predicted by classical electrodynamics[14]. As a result of combined effects, there exists an optimal interparticle separation at which the field enhancement will be maximum. The magnitude of SERS is known to be approximately proportional to the fourth power of the local field enhancement[15], therefore finding the optimal distance will be crucial for achieving enormous SERS enhancement for developing ultrasensitive molecular sensors. Nanostructures fabricated with conventional lithographic and self-assembly methods are hard to tune the interparticle distance at nanometer scales.

Here the NPoM geometry is used to precisely control interparticle distance, therefore providing maximum field enhancement for optimal SERS performance. This geometry allows a broad variety of nanoparticles and substrate materials to be utilised, enabling a systematic investigation. More importantly, the gap between nanoparticle and substrate can be precisely controlled with spacing layers. Dielectrics and even atomically thin two-dimensional materials have been used as spacers, which demonstrate that such a system is a robust and efficient light concentrator, making it a superior structure for a broad range of plasmonic applications[14,16-22].

In this work, it is demonstrated that a NPoM can be used to achieve optimal SERS by accurately controlling the interparticle spacing. In order to precisely control the interparticle distance, a spacing layer of tantalum pentoxide (Ta_2O_5) is sputtered onto the bare Au film. A variety of Ta_2O_5 films with thickness ranging from 1 to 10 nm were used to tune the interparticle gap at nanometer-scale resolution to find the optimal distance for SERS. Nanostructures with spacing gaps of 1 nm were found to produce maximal SERS. The results are consistent for various molecular species and Raman modes. The experimental data are in good agreement with simulation results based on dimer systems, confirming that the strong enhancement of SERS indeed originates from the particle-image particle coupling. Simulation results indicate that the SERS enhancement of the NPoM system is almost up to 100 millions (10^8) folds, which is extraordinarily strong enabling single molecule detection.

5.2 Materials and methods

The substrates were prepared by depositing a 50 nm gold film onto silicon substrate by magnetron sputtering, which were then sputtered with Ta_2O_5 films of thickness 1, 1.5, 2.5, 5 and 10 nm. 150 nm gold nanoparticle solution (purchased from BBI) was drop-cast onto the samples, allowed to dry, and cleaned with deionized water.

An excitation laser of 633 nm with a power of 0.8 mw was focused on individual Au nanoparticles through a 100x Olympus objective (NA=0.9). SERS spectra were collected through a back-reflection configuration and coupled to a Jobin Yvon HR640 Raman spectrometer. All Raman spectra were normalized to the 520 cm^{-1} Raman mode of silicon, with respect to the excitation laser's power and integration time. To mitigate the effects of the variation in nanoparticle sizes and shapes, the geometries of nanoparticles

were carefully examined with scanning electron microscopy (SEM). Only spherical nanoparticles with diameter in the range of 150±5 nm were selected, and for each separation distance, a total of 15 Raman spectra were taken and averaged.

Dark-field optical scattering spectra were taken using an Olympus microscope (model BX51). A 100x magnification objective with NA = 0.9 was used to collect scattering signals from individual Au nanoparticles. The spectra were taken with a QE65 spectrometer from Ocean Optics.

5.3 Results and discussion

Ta_2O_5 was chosen as it is an inert dielectric and a good insulator with a bandgap larger than 3.8 eV that is well above the excitation wavelengths used in our experiments, therefore avoiding fluorescence signals that otherwise might interfere the experimental results. A range of Ta_2O_5 films of thickness of 1 nm, 1.5 nm, 2.5 nm, 5 nm and 10 nm were sputtered on 50 nm Au films deposited on Si substrates. Gold nanoparticles of 150 nm in diameter were drop-cast on the surface of Ta_2O_5 film to form the nanoparticle-on-surface plasmonic system.

Figure 5.1a shows the measured SERS spectra of Au nanoparticles sitting on Ta_2O_5 films of various thickness, under the excitation of 633 nm laser. The striking features of the SERS spectra in figure 5.2a are the two distinct peaks at 1340 and 1580 cm^{-1}, which are the D- and G- Raman modes of carbon[23], respectively. Strong SERS signals of carbon were often observed on gold and silver nanostructures[24,25], which are from small traces of carbon molecules (or organic molecules) existing in ambient environment that adsorbed on the

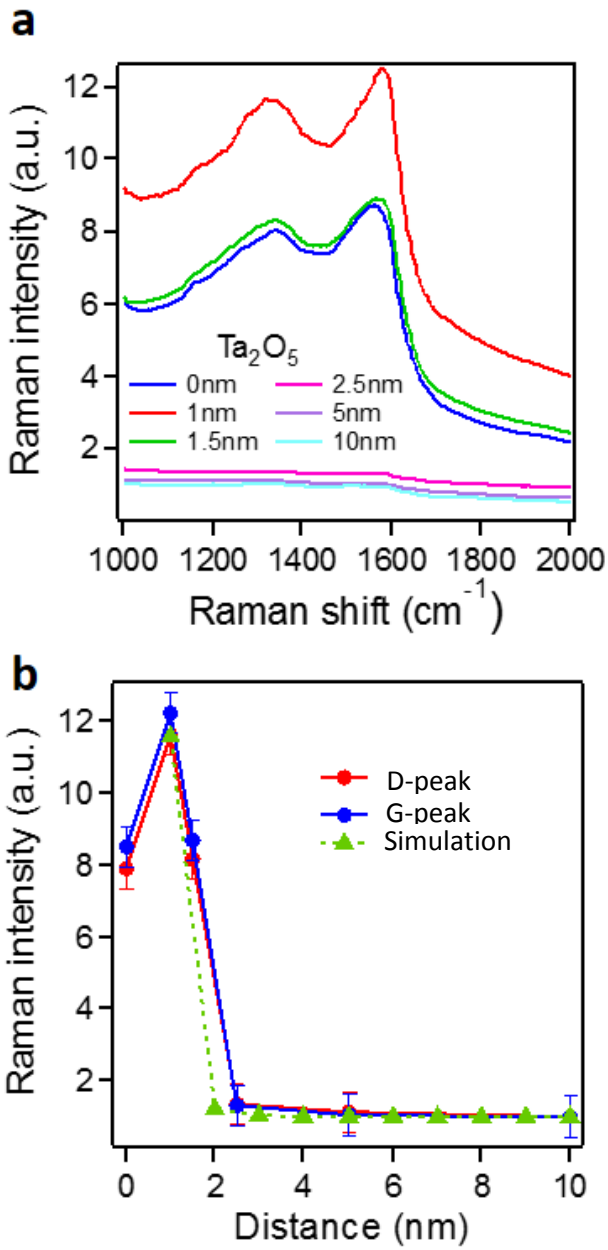

Figure 5.1 (a) Measured SERS spectra from Au nanoparticles on Au films with various Ta_2O_5 spacing layers ranging in thickness from 0-10 nm. (b) The peak intensities of the (red circles) D-peak and (blue circles) G-peaks as a function of the gap distance, and (green triangles) the simulated SERS enhancements within the gaps of an analogue dimer system

surface of metal nanostructures. Here the observed SERS signals of carbon are likely from citrate molecules, which were used as a protection layer on Au nanoparticles to prevent nanoparticles aggregating in solution. Previous

experiments have demonstrated that when laser is irradiating on a nanoparticle, it could cause thermal denaturation of the citrate, forming amorphous carbon structures on the particles[26,27]. Another notable feature in the SERS spectra is that strong SERS signals are sitting on top of a broad continuum of background signals. These are most noticeable in the spectra on 0-1.5 nm Ta_2O_5 in figure 5.1b. Such background signals are frequently observed in SERS experiments, which come from the dissipative and resistive damping of the image molecules on the nanoparticle[28]. As seen from figure 5.1a, the SERS signals are most prominent at small gaps, diminishing rapidly with increasing gap size. No measureable Raman signals were observed from Au nanoparticles on glass and Si substrates. This indicates that the measured SERS signals are only from a small number of molecules in the hot spots between the nanoparticle and the underlying Au substrates, where the plasmonic coupling between the nanoparticle and image particle produces extremely strong optical fields. To show the trend of SERS intensity more clearly, in figure 5.1b the peak intensities of the D- and G- Raman modes are plotted as a function of the gap distance. For simplicity, the overall intensities of the Raman peaks, including the background signals, are plotted. The SERS signals exhibit a nonlinear dependence on the gap distance. They are relatively modest at distances beyond a few nanometers, increasing gradually as the gap approaches from 10 nm to 2.5 nm. The signals then increase rapidly when the gap is in the region around one nanometer. When nanoparticles are directly on top of bare Au substrates, the SERS signals drop considerably. Maximal SERS signals were observed at 1 nm spacing distance.

Similar results were observed on a different molecular species. To demonstrate the applicability and reproducibility of the NPoM SERS system, we utilized the NPoM structure to detect 4-aminothiophenol (4-ATP) molecules. The NPoM structures were immersed in 1 mM solution of 4-ATP

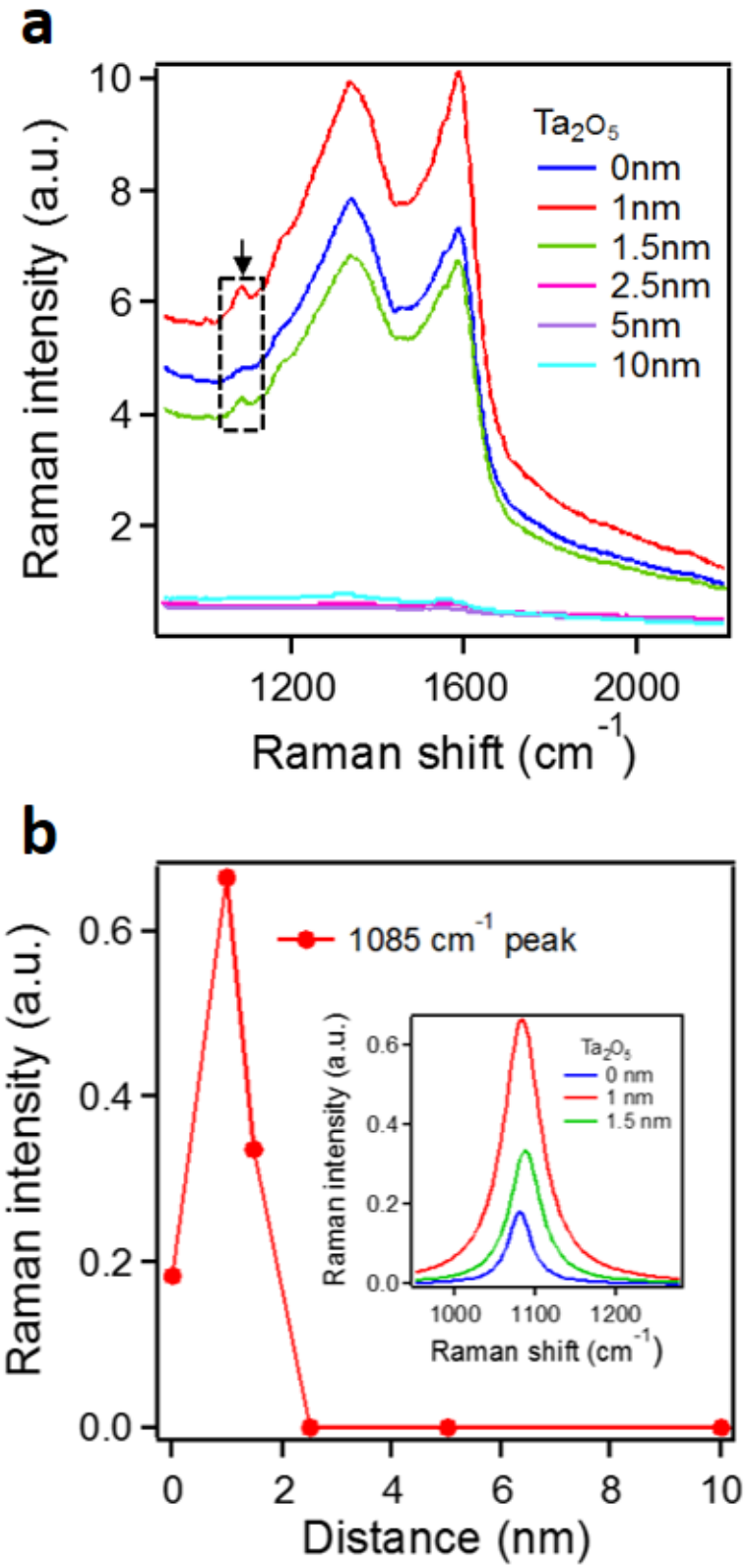

Figure 5.2 (a) Measured SERS spectra of 4-ATP molecules adsorbed on 150 nm Au particles on Au films with various thickness of Ta_2O_5 spacing layers. (b) The intensities of the 1085 cm^{-1} Raman peaks as a function of the gap distance. Inset: the fitted Lorentzian peaks of the 1085 cm^{-1} 4-ATP Raman modes

in ethanol for three hours, then rinsed with deionized water and left dry. In this way, 4-ATP molecules were adsorbed on the surface of Au nanoparticles[17]. The SERS spectra of 4-ATP molecules from NPoM structures of various Ta_2O_5 spacing were shown in figure 5.2. There is a minor peak at ~1085 cm^{-1} (marked by box and arrow), which is the a_1 Raman mode of 4-ATP molecules[17,19]. As the Raman mode of 4-ATP is sitting on top of the strong and broad carbon modes, to obtain more accurate information about the position and intensity of the Raman mode, the Raman spectra are fitted with three Lorentzian-profile peaks. The Raman modes of the 4-ATP molecules extracted from the fitting results are shown in the inset of figure 5.2b. The intensities of the 1085 cm^{-1} Raman mode are plotted in figure 5.2b as a function of the gap distance, which displays a very similar distance dependence to those shown in figure 5.1. Maximal SERS is again achieved with a 1 nm spacing layer of Ta_2O_5. This demonstrates that the results are consistent and reproducible for different Raman modes and molecular species. Previous studies have indicated that the coupling between a metal nanoparticle and a metal surface is essentially analogue to a dimer system, where the nanoparticle couples to its image particle inside the metal substate[16-22]. To test this assumption, theoretical simulations were carried out using commercial COMSOL software for a dimer system mimicking the NPoM structure. The configuration of the dimer system is shown in figure 5.3a, which is comprised of a pair of Au nanospheres of diameter of 150 nm, separated by a small air gap of 1 nm. A beam of plane waves with a TM-polarization is incident at an angle of 64° to the dimer axis, which is corresponding to the numerical aperture (NA=0.9) of a 100× dark-field objective lens used in the experiments. A TM-polarized plane wave is chosen as it provides the necessary field component along the dimer axis to induce a strong coupling between the two nanoparticles. As seen from the calculated field distribution (figure 5.3a), the electromagnetic fields are highly concentrated in the gap between nanoparticles. The magnitude of the

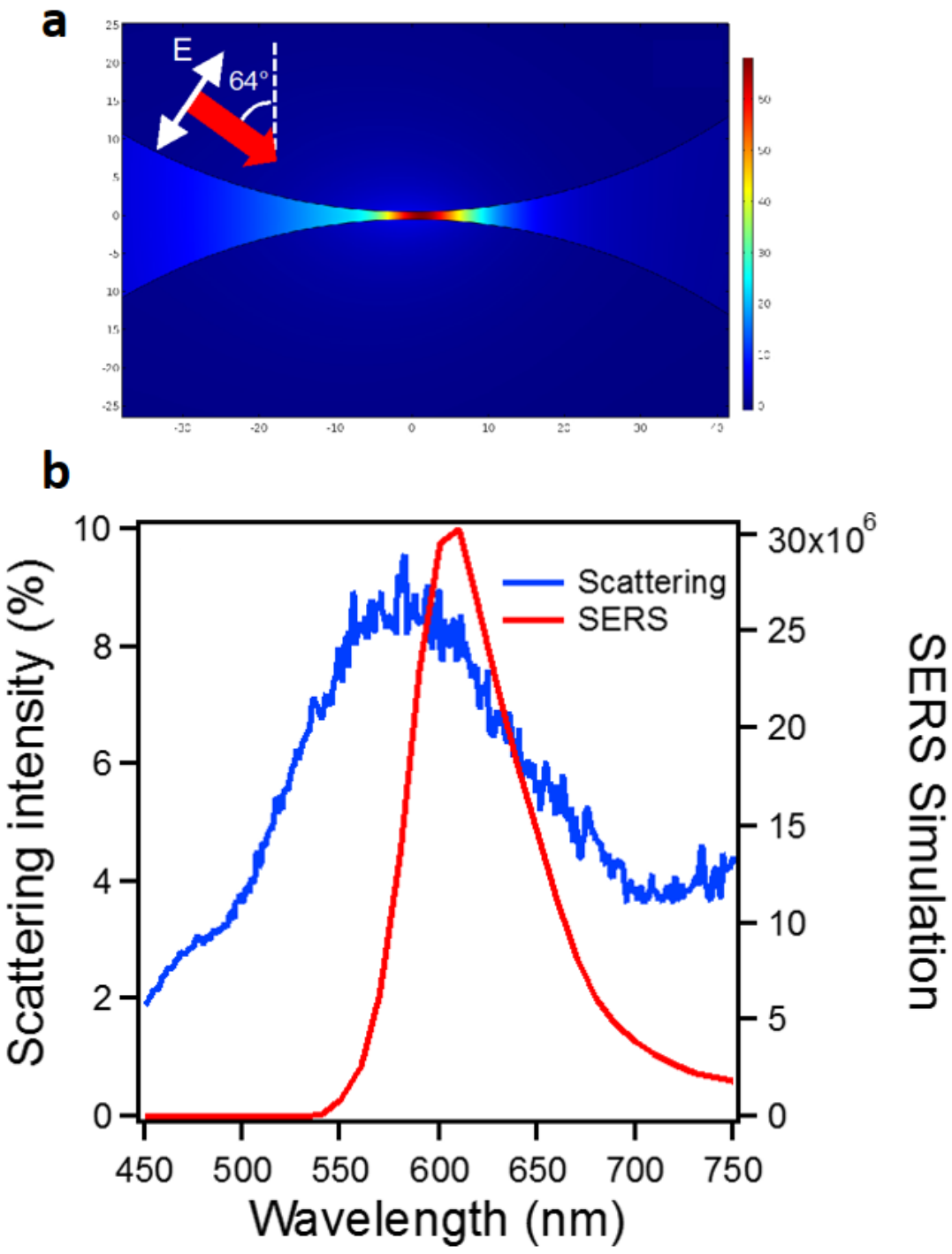

Figure 5.3 Calculated electric field enhancement distribution of a Au dimer system (150 nm in diameter, separated by a 1 nm air gap). The field is highly concentrated within the gap. A plane wave of 633 nm is incident along the direction indicated by the red arrow. The polarization of light is indicated by the double arrow. (b) Calculated SERS enhancement spectrum for the dimer system (red line) and the measured optical scattering spectrum of individual Au particles (150 nm) on Au films separated by 1 nm Ta_2O_5 film (blue line)

enhanced field is about 70 folds as that of the incident field. Figure 5.3b shows the calculated SERS enhancement spectrum (fourth power of the field enhancement, red line) at the middle point of the dimer gap. The spectrum shows the system has a plasmonic resonance at 610 nm, which is quite close to the resonant wavelength (590 nm) of the measured optical dark-field scattering spectrum of a 150 nm Au nanoparticle on top of a Au substrate with 1 nm Ta_2O_5 spacing layer (blue line). The two spectra exhibit similar spectral profiles, apart from the small deviation in the peak wavelength. This is understandable, as the dimer system is a close analogy but not exactly the same structure as the NPoM system used in experiments. From the scattering spectrum, it is seen that 633 nm is slightly off the plasmonic resonance of the system. An excitation wavelength closer to the resonance should produce stronger SERS signals. To test this, a 594 nm laser was also used to measure the SERS. Results exhibited much stronger SERS signals, almost twice that of 633 nm (figure 5.4). Electric fields at the middle points of the gap for a variety of gap separations were simulated with an excitation wavelength of 633 nm. The results (the fourth power of the field enhancement, divided by a factor of 2 million) are shown in figure 5.1b (triangles and dashed line), and match the experimental data extremely well. The good agreement between experimental and simulation results confirms that the coupling between a nanoparticle and a reflective metallic surface indeed can be well mimicked by the coupling between the nanoparticle and the image particle. The enhancement factor increases dramatically at close distances around nanometers, which is the characteristic nature of plasmonic resonance, as charge density piles up significantly across the junction with decreasing gaps. When nanoparticles are directly sitting on top of Au surfaces, electrons can transfer between nanoparticles and substrates, as a result, the charge density is reduced and hence the field enhancement and SERS signals are diminished. With the aid of a 1 nm dielectric spacer, the SERS signals increase significantly. According to

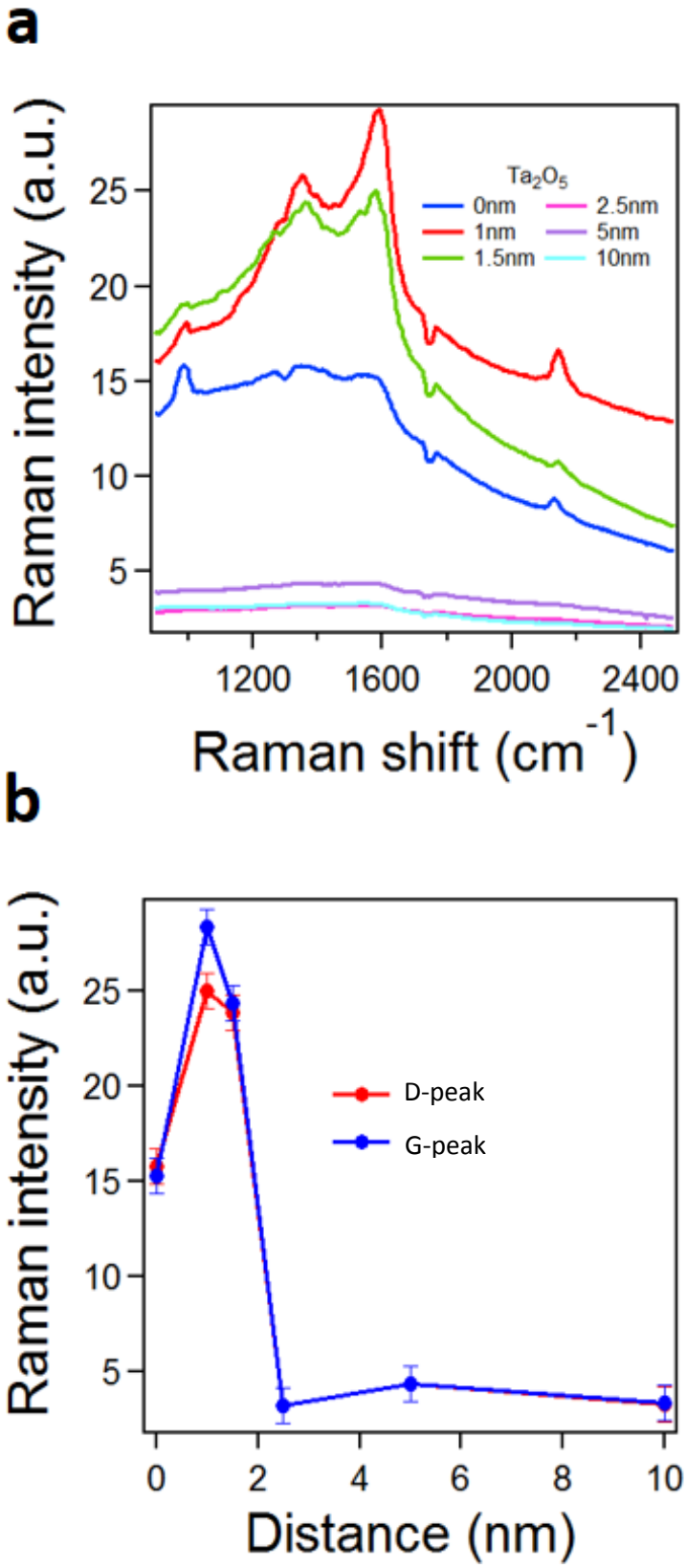

Figure 5.4 Experimental SERS spectra measured from 150 nm Au particles on Au films with various thicknesses of Ta_2O_5 spacing layers taken with a 594 nm laser. (b) Intensities of the (red) D-peak and (blue) G-peaks as a function of the gap distance

the simulation results, the maximal SERS enhancement of the system is about 3×10^7, which is a staggeringly strong enhancement, sufficient for single-molecule SERS detection[30]. Previous studies have demonstrated that the field enhancements of NPoM systems are stronger than that of dimers[17], so the actual SERS enhancement of the NPoM systems could be exceeding 10^8. Unlike dimer systems that are hard to fabricate and difficult to tune the interparticle distance, the NPoM plasmonic system is rigid, robust and reproducible, with precisely controllable interparticle distance. It is envisioned that the enhancement could be further improved by fine tuning the gap using thinner spacing layers, such as atomically thin two-dimensional materials. As such, the NPoM plasmonic system holds great promise for developing reliable ultrasensitive sensors for a broad range of applications.

5.4 Conclusions

In conclusion, it has been demonstrated that with NPoM plasmonic systems, surface-enhanced Raman scattering can be optimized with precisely controlled interparticle distance defined by dielectric spacing layers. Optimal SERS is achieved on NPoM systems with spacing distance around 1 nm. The results are consistently observed with different excitation wavelengths and on different molecules, which clearly show distinct characteristics of surface plasmon resonance. The experimental results are in good agreement with theoretical simulations based on dimer systems, which confirms that the strong SERS enhancement originates from the enhanced electric fields within the gap due to particle-image particle coupling. With optimized field enhancement, the devices will have applications in a broad variety of areas, such as photothermal therapy, nonlinear optical effects, light harvesting in solar cells and ultrasensitive molecular sensing.

5.5 References

1. Fleishmann, M., Hendra, P.J. & McQuillan, A.J., *Raman spectra of pyridine adsorbed at a silver electrode*, Chemical Physics Letters 26, no. 2 (1974): 163-166
2. Sarycheva, A.S., et al., *New nanocomposites for SERS studies of living cells and mitochondria*, Journal of Materials Chemistry B 4, no. 3 (2016): 539-546
3. Song, L., Mao, K., Zhou, X. & Hu, J., *A novel biosensor based on Au@Ag core-shell nanoparticles for SERS detection of arsenic (III)*, Talanta 146 (2016): 285-290
4. Si, K.J., Guo, P., Shi, Q. & Cheng, W., *Self-assembled nanocube-based plasmene nanosheets as soft surface-enhanced Raman scattering substrates toward direct quantitative drug identification on surfaces*, Analytical Chemistry 87, no. 10 (2015): 5263-5269
5. Nie, S. & Emory, S.R., *Probing single molecules and single nanoparticles by surface-enhanced Raman scattering*, Science 275, no. 5303 (1997): 1102-1106
6. Lim, D.K. et al., *Nanogap-engineerable Raman-active nanodumbbells for single-molecule detection*, Nature Materials 9, no. 1 (2010): 60
7. Aioub, M. & El-Sayed, M.A., *A real-time surface enhanced Raman spectroscopy study of plasmonic photothermal cell death using targeted gold nanoparticles*, Journal of the American Chemical Society 138, no. 4 (2016): 1258-1264
8. Soliveri, G. et al., *Microwave-assisted silver nanoparticle film formation for SERS applications*, The Journal of Physical Chemistry C 120, no. 2 (2016): 1237-1244

9. Qian, Z., Li, C., Fakhraai, Z. & Park, S.J., *Unusual weak interparticle distance dependence in Raman enhancement from nanoparticle dimers*, The Journal of Physical Chemistry C 120, no. 3 (2015): 1824-1830
10. Kravtsov, V., Berweger, S., Atkin, J.M. & Raschke, M.B., *Control of plasmon emission and dynamics at the transition from classical to quantum coupling*, Nano Letters 14, no. 9 (2014): 5270-5275
11. Savage, K.J. et al., *Revealing the quantum regime in tunnelling plasmonics*, Nature 491, no. 7425 (2012): 574
12. Esteban, R. et al., *A classical treatment of optical tunneling in plasmonic gaps: extending the quantum corrected model to practical situations*, Faraday Discussions 178 (2015): 151-183
13. Garcia de Abajo, F.J., *Nonlocal effects in the plasmons of strongly interacting nanoparticles, dimers, and waveguides*, The Journal of Physical Chemistry C 112, no. 46 (2008): 17983-17987
14. Ciraci, C. et al., *Probing the ultimate limits of plasmonic enhancement*, Science 337, no. 6098 (2012): 1072-1074
15. Garcia-Vidal, F.J. & Pendry, J.B., *Collective theory for surface enhanced Raman scattering*, Physical Review Letters 77, no. 6 (1996): 1163
16. Aravind, P.K. & Metiu, H., *The effects of the interaction between resonances in the electromagnetic response of a sphere-plane structure; applications to surface enhanced spectroscopy*, Surface Science 124, no. 2-3 (1983): 506-528
17. Huang, F.M. et al., *Dressing plasmons in particle-in-cavity architectures*, Nano Letters 11, no. 3 (2011): 1221-1226
18. Mertens, J. et al., *Controlling subnanometre gaps in plasmonic dimers using graphene*, Nano Letters 13, no. 11 (2013): 5033-5038
19. Mubeen, S. et al., *Plasmonic properties of gold nanoparticles separated from a gold mirror by an ultrathin oxide*, Nano Letters 12, no. 4 (2012): 2088-2094

20. Lei, D.Y. et al., *Revealing plasmonic gap modes in particle-on-film systems using dark-field spectroscopy*, ACS Nano 6, no. 2 (2012): 1380-1386
21. Yamamoto, N., Ohtani, S. & Garcia de Abajo, F.J., *Gap and Mie plasmons in individual silver nanospheres near a silver surface*, Nano Letters 11, no. 1 (2010): 91-95
22. Le, F. et al., *Plasmons in the metallic nanoparticle-film system as a tunable impurity problem*, Nano Letters 5, no. 10 (2005): 2009-2013
23. Ferrari, A.C. & Robertson, J., *Raman spectroscopy of amorphous, nanostructured, diamond-like carbon, and nanodiamond*, Philosophical Transactions of the Royal Society of London A: Mathematical, Physical and Engineering Sciences 362, no. 1824 (2004): 2477-2512
24. Wang, H. et al., *Carboxyl and negative charge-functionalised superparamagnetic nanochains with amorphous carbon shell and magnetic core: synthesis and their application in removal of heavy metal ions*, Nanoscale 3, no. 11 (2011): 4600-4603
25. Richards, D., Milner, R.G., Huang, F. & Festy, F., *Tip-enhanced Raman microscopy: practicalities and limitations*, Journal of Raman Spectroscopy 34, no. 9 (2003): 663-667
26. Mak, S.W.J., *Raman characterization of colloidal nanoparticles using hollow-core photonic crystal fibers*, PhD thesis, University of Toronto, 2011
27. Qian, X.M. & Nie, S.M., *Single-molecule and single-nanoparticle SERS: from fundamental mechanisms to biomedical applications*, Chemical Society Reviews 37, no. 5 (2008): 912-920
28. Barnett, S.M., Harris, N. & Baumberg, J.J., *Molecules in the mirror: how SERS backgrounds arise from the quantum method of images*, Physical Chemistry Chemical Physics 16, no, 14 (2014): 6544-6549
29. Hu, X., Wang, T., Wang, L. & Dong, S., *Surface-enhanced Raman scattering of 4-aminothiophenol self-assembled monolayers in sandwich structure with*

nanoparticle shape dependence: off-surface plasmon resonance condition, The Journal of Physical Chemistry C 111, no. 19 (2007): 6962-6969

30. Lee, H.M., Jin, S.M., Kim, H.M. & Suh, Y.D., *Single-molecule surface-enhanced Raman spectroscopy: a perspective on the current status*, Physical Chemistry Chemical Physics 15, no. 15 (2013): 5276-5287

Chapter 6

Characterising graphene flakes on bulk gold through optical contrast spectroscopy

6.1 Introduction

A key step in design of new technology has been the discovery[1] and integration of graphene into devices. Because of its unique electronic properties, such as having a zero band gap around which electrons behave as massless Dirac-fermions[2,3], and having the lowest resistivity[4,5] (10^{-6} Ω.m) of any material at room temperature make graphene one of the most attractive materials to use in such industries as energy, photonics and electronics[6,7,].

However, the substrate which supports graphene has a large effect on its properties. This includes doping its electronic structures, altering its conductivities and shifting its Raman and fluorescent resonances[8-10]. Gold is very often used[11-13] because it is chemically stable with good electrical and plasmonic properties. Graphene, like other 2D materials, can also be integrated with the NPoM geometry as a spacing layer[14-16] since it is atomically flat and electrically insulating in the out-of-plane direction. It is of particular interest because graphene can reliably achieve sub-nanometre spacing layers, wherein strongly enhanced fields are generated. By altering the thickness of the graphene spacing layer, the enhancement and plasmonic resonance are tuned[17]. It is therefore very important to accurately characterise a graphene flake's thickness on gold substrates, so that these properties can be investigated and utilised.

Typically, AFM[18-20] and Raman scattering spectroscopy[21-23] have been used for this purpose. However, these techniques have several disadvantages. For example, to take a sufficiently detailed image with AFM can take several hours. The tip, which must be brought close to the flake's surface, can also easily damage it.

Raman spectroscopy, on the other hand, is faster, and can probe a flake's thickness non-destructively based on the ratio of the intensities of the G and 2D peaks, as well as the shape and wavenumber of the 2D peak[24-26]. However, this method can be affected by elements of the flake's environment, such as temperature[27], doping[28] and strain[28]. This can lead to ambiguous results of a flake's true thickness.

One other alternative method is to use optical contrast spectroscopy. Like Raman, it is a fast and non-invasive. However, it is much less affected by the aforementioned factors. Therefore, it is being used more frequently by researchers working with graphene and other 2D materials[29-32].

Although this technique has previously been investigated on SiO_2 substrates[33], it has not been examined much for metallic substrates. A previous theoretical study also examined the contrast spectra of graphene on very thin gold using simulations based on Fresnel equations at normal incidence[34]. For this chapter, contrast spectra were measured from few-layered (1-5 layers) of graphene on bulk gold, which is so thick that underlying films have no impact on the reflectance of light or contrast. Results are compared to a modified model which takes into account contributions from different incident angles and polarisations. This is important because the experiment uses a high numerical aperture lens, which contains a large cone of incident angles. Results were then compared to AFM and Raman measurements. It was observed that the optical contrast spectra from freshly-prepared samples matched the predicted results from the theoretical model very well, while samples that had be exposed to ambient conditions saw an increase in their contrast. This

technique could therefore be exploited as a miniaturised and highly sensitive optical sensor.

6.2 Sample characterisation

Flakes were found using a 100x objective lens (numerical aperture 0.9) in bright-field mode with an optical microscope. Reflected light was collected through a coupled optical spectrometer, from which it was inputted into the equation:

$$C = 1 - \frac{R_{Gr}}{R_{Au}} \tag{6.1}$$

where C is the optical contrast, R_{Au} is the reflectance of light on the bare gold substrate and R_{Gr} is the reflectance of light on the gold substrate covered with a graphene flake. The contrast is positive (negative) when the addition of a graphene flake reduces (increases) the reflectance of light on the substrate.
Raman measurements were carried out with a 532 nm laser with a power of 1 mW. AFM measurements were carried out in tapping mode on a Digital Instruments, Nanoscope IIIa. Images were processed[35] using WSxM 4.0, and step heights analysed with Nanoscope Analysis 1.5.

6.3 Results and discussion

6.3.1 Optical contrast spectroscopy

After graphene was exfoliated onto the 100 nm bulk gold substrates, flakes of varying thickness were observed at 100x magnification. Their thickness was initially estimated based on how their contrast looked by eye. By this method, thicker flakes (≳3L) are clearly visible (figure 5.1a-b), while thinner layers are much harder to see. One way to slightly improve the contrast is to use a 490

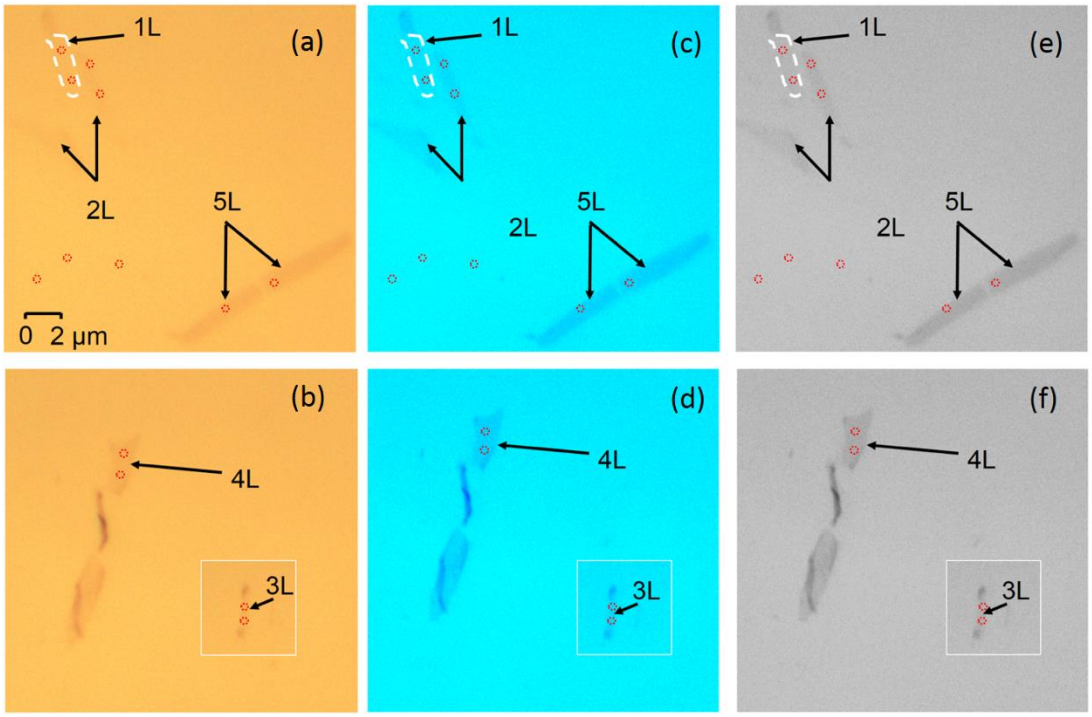

Figure 6.1 (a-b) Bright-field images of 1-5 layered graphene flakes without an optical filter, (c-d) with a 490 nm optical filter (10 nm bandwidth), and (e-f) grayscale images of (c-d). The contrast in (e) is enhanced by two times for a better view of the monolayer film. The inset of the 3L film was taken at a different location on the sample and superimposed here. Red dashed circles represent locations from where reflection measurements were taken

nm (10 nm bandpass width) band filter in front of the light source (figure 6.1c-d), and even more so if the subsequent image is converted into grayscale (figure 6.1e-f). Before measurements were taken from the flakes, simulations were carried out to estimate the expected contrast for increasingly thick graphene flakes on bulk gold substrates. Whereas previous experiments have used simple Fresnel reflection equations at normal incidence[33,34,36], these experiments use simulations that take into account contributions from different incident angles. This is important because for high magnification lenses, changing incident angles and polarisations have more of an impact, which therefore alters the reflection. This is illustrated in figure 6.2, where

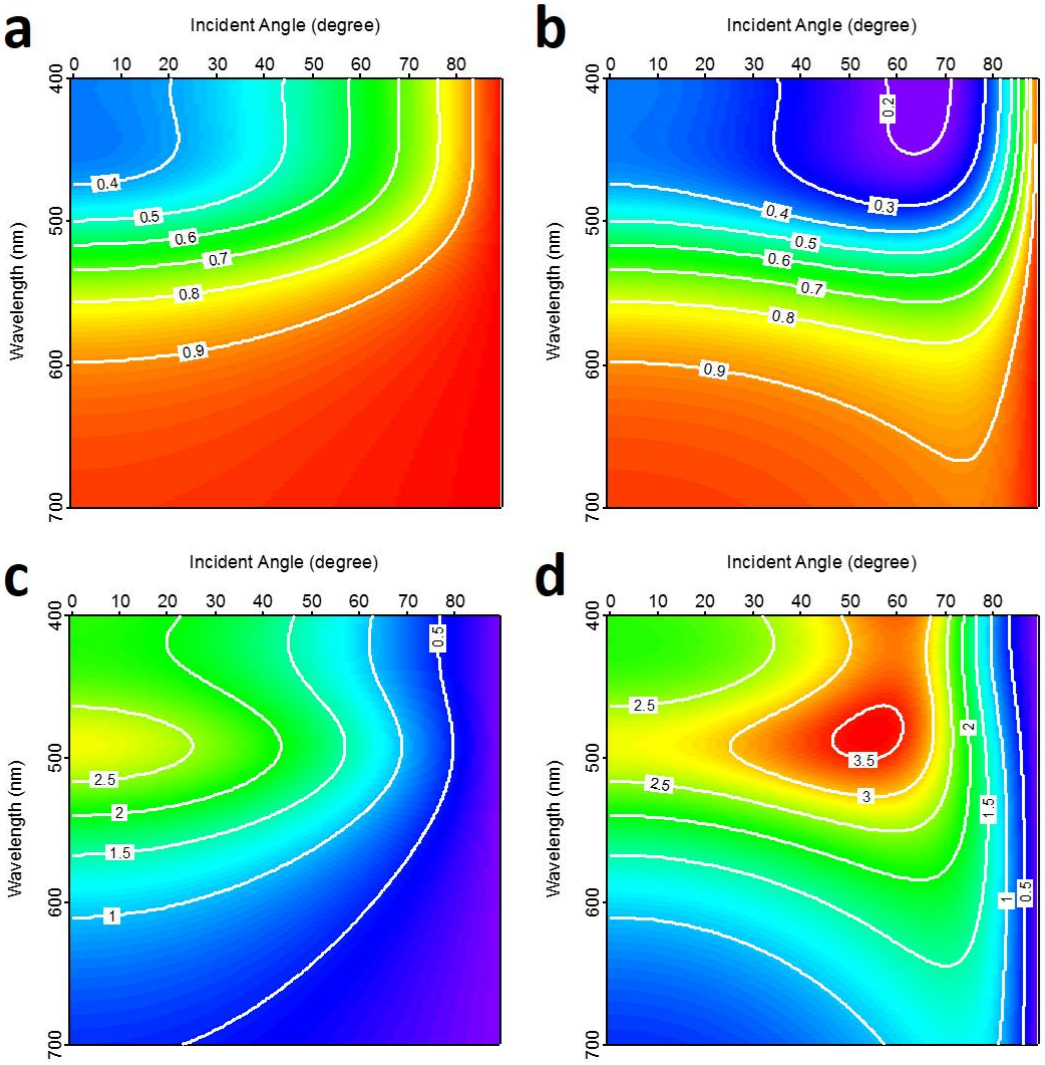

Figure 6.2 Calculated optical contrast and reflectivity of monolayer graphene on 100 nm Au, as functions of the incident angle and wavelength of light. (a-b) Reflectance, (c-d) contrast. The left and right panels are for TE- and TM- polarisations, respectively, presented with the same colour scale. Refractive index of graphene n_G = 2.6-1.3i; thickness 0.335 nm

optical contrast and reflectance were calculated at varying angles and polarisations. This was based on the transfer matrix method[37]. The reflectance is almost constant up to 20°, but changes markedly with increasing incident angles (figure 6.2a-b). As a result, the contrast is inhomogeneous across incident angles and polarisations (figure 6.2c-d). Furthermore, the amount of light varies with incident angles. A high numerical aperture lens has a large

incident cone with a spanning angle of θ_0 ($\sin\theta_0$ = NA, e.g. NA = 0.9, θ_0 = 64°). As a result, the contribution of different incident angles and polarisations is averaged to get more accurate data for the reflection and contrast spectra, such that:

$$\boldsymbol{R_{av} = \frac{1}{2}(\overline{R}_{TE} + \overline{R}_{TM})} \tag{6.2}$$

where

$$\boldsymbol{\overline{R}_{TE,TM} = \frac{2\int_0^{\theta_0} R^{TE,TM}(\theta)\tan\theta(\sec\theta)^2 d\theta}{(\tan\theta_0)^2}} \tag{6.3}$$

where $\boldsymbol{\overline{R}_{TE,TM}}$ is the reflectance averaged over incident angle and $\boldsymbol{R^{TE,TM}(\theta)}$ is the reflectance at an incident angle of θ for TE and TM polarisations respectively (see chapter 3 for more details). The contrast spectra are then calculated using equation 6.1.

The thickness of the graphene is given as d = 0.335N nm, where N is the number of layers. The refractive index of graphene is taken as the same as that of graphite (2.6 – 1.3i). Although it is not a strictly accurate assumption, since graphene's refractive index varies with wavelength, previous experiments have shown good agreement between experimental and simulated optical contrasts in the wavelength regime of interest[34,36]. The refractive index of gold was taken from literature[38].

Reflection spectra were then measured both from bare gold substrates and the graphene flakes so that the contrast spectra can be produced (indicated by red dashed circles in figure 6.2). The measured results are compared to the simulated results in figure 6.3a. A clear peak is seen at around 500 nm. It increases with the number of layers, but it does not shift much. This explains why the 490 nm filter gives better contrast in the optical images. Excellent

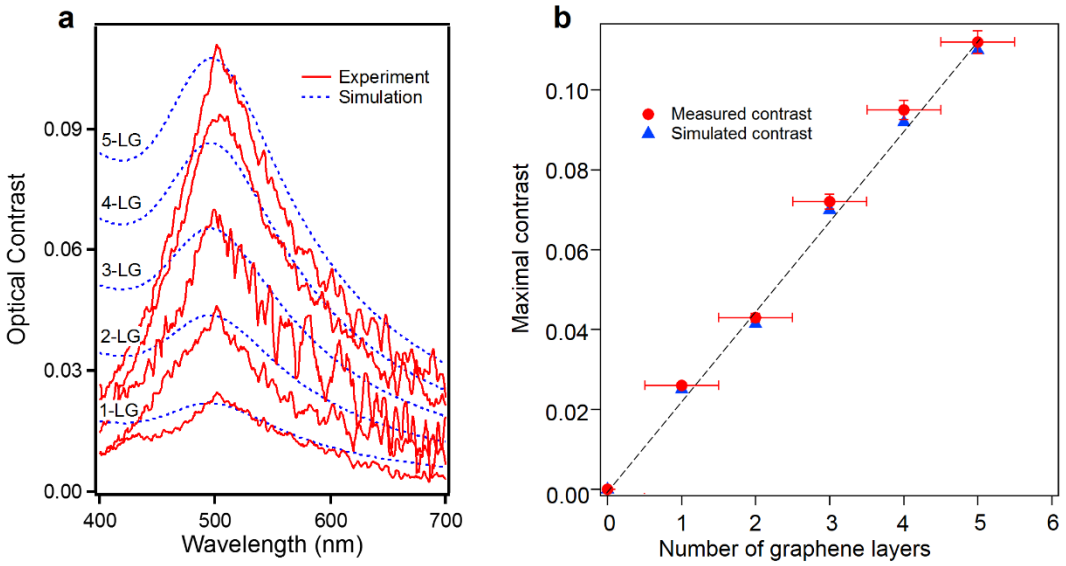

Figure 6.3 (a) Measured (red) and simulated (blue) contrast spectra taken from 1-5 layers of clean graphene. (b) Graph showing how the maximum contrast changes with the number of layers

agreement is seen with the simulated results, especially in the long wavelength region (λ>500 nm). The data shows a linear relationship between the maximum intensity and the number of layers. Furthermore, when the fitting line is extrapolated, it passes through the graph's origin, thus proving the validity of the model and the high quality of the graphene flakes. However, it is noticeable that the modelled data is much less accurate in the short wavelength region. This is because the assumption that graphene's refractive index is fixed is not correct. It varies with wavelength, and this dependence is especially pronounced for short wavelengths[39,40]. It is also not necessarily true that there are equal contributions from TE and TM light polarisations. For example, the various optical components used in the experiments such as beamsplitters and optical fibres may not function with equal efficiencies for the two polarisations. Since the reflectivity of TE and TM light deviates strongly in the short wavelength region, small imbalances

between the polarisations will have a big impact on the reflectivity and therefore the contrast.

6.3.2 Raman and AFM characterisation

In order to compare the effectiveness of the optical contrast method, the thickness of the flakes was also taken using the conventional techniques of Raman spectroscopy and AFM (figure 6.4).

Raman spectroscopy (figure 6.4c-d) shows that the G peak increases in intensity in relation to the 2D peak, which consequently increases the G:2D intensity ratio linearly with film thickness. It can also be seen that the 2D peak changes in shape with film thickness, as a result of double resonance which links photon wave vectors with the electronic band structure[41,42]. Although these characteristics are generally consistent with previous experiments[42,43], it is important to note that the G:2D intensity ratio is larger than expected. This is probably due to doping from the substrate, which can result in a decrease in the 2D peak's intensity[30,44], and hence demonstrates one of the limitations of Raman spectroscopy in characterising thickness of graphene flakes on gold substrates.

Results from AFM tapping mode measurements (figure 6.4a-b) give step profiles of 0.62 ± 0.02, 0.76 ± 0.03, 1.17 ± 0.05 and 1.55 ± 0.05 nm for one, two, three and five layers respectively. Within the experimental uncertainties, there is quite good agreement for the heights of two, three and five layer flakes. Although the height of the monolayer is larger than expected, this is not unusual for AFM measurements. This is because monolayer graphene is not very robust. If the substrate being used has a large thickness, the monolayer will behave like a tissue and follow the morphology of the roughness, thereby giving the flake a deceptively large thickness[45,46].

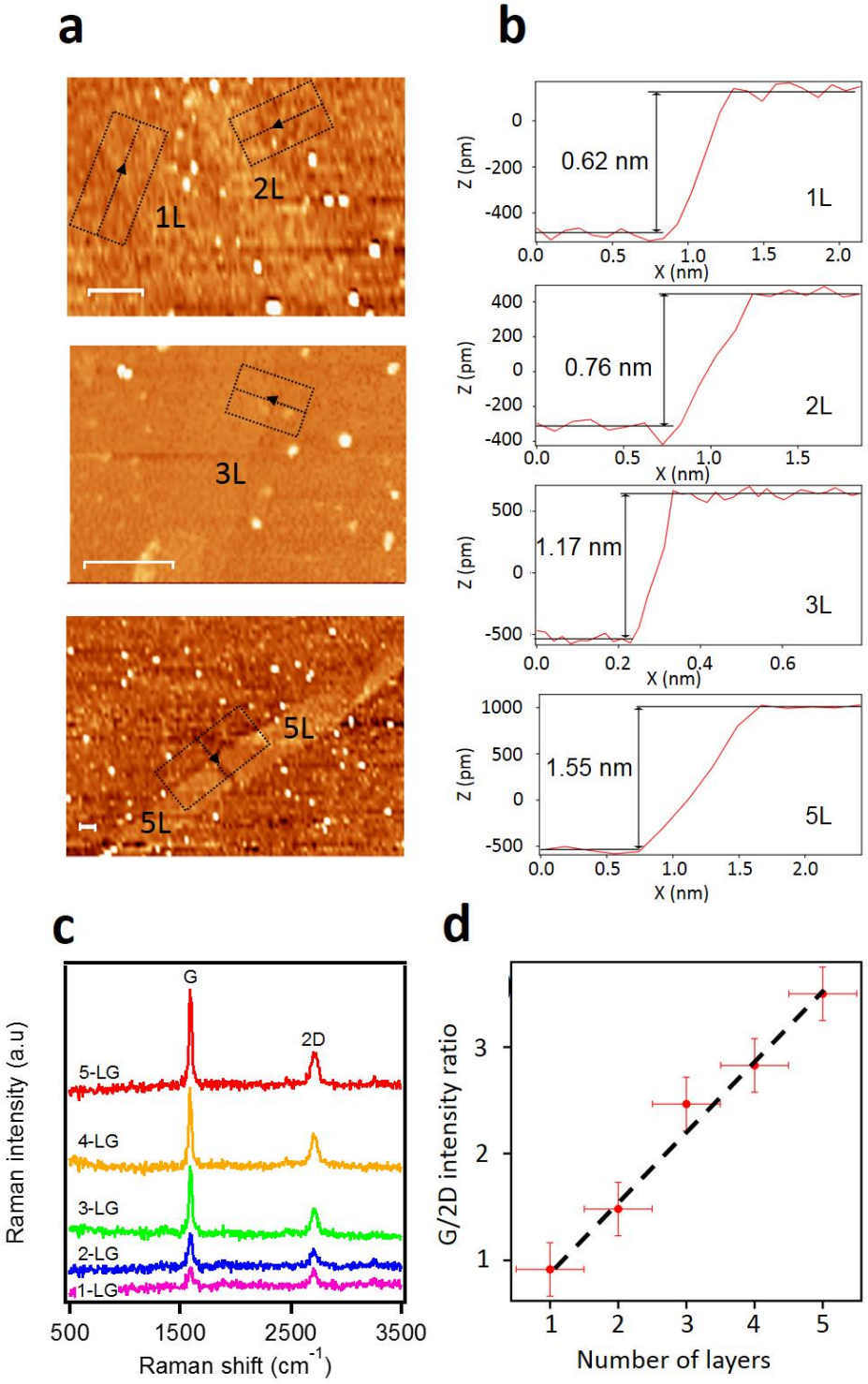

Figure 6.4 (a) AFM images and (b) smoothed step profiles of graphene flakes shown in figure 6.1. Height profiles are averaged within the boxes marked in the AFM images. Arrows indicate the directions of the height profiles. All scale bars correspond to 1 μm. (c) Raman spectra measured from 1-5 layers of graphene excited by a 532 nm laser. (d) Graph showing the ratio of the normalised intensity of the G and 2D peaks as a function of number of layers

As the thickness increases, the flake gets sturdier and so the AFM is able to measure its height more accurately.

So, although Raman and AFM measurements have limitations, the results broadly agree with the results from the optical contrast spectroscopy study.

6.3.3 Molecule adsorption detection

Results have demonstrated the linear dependence of the contrast for graphene flakes with their thickness. This is impressive given that each additional sheet is only a single layer of carbon atoms. Such sensitivity means that optical contrast spectroscopy could be used as a way to detect whether the flakes have been contaminated by molecules being adsorbed to the graphene's surface. This is a big problem for scientists who work with graphene in a laboratory environment where many airborne molecules (such as alkanes, alkenes, aromatics, alcohol and water) can potentially adsorb to the flake[47].

In order to examine if this can be a practical application, simulations were carried out to see how adsorption of airborne molecules would impact the optical contrast of a monolayer graphene flake on a bulk gold substrate (figure 6.5). The simulations take the molecule to be amorphous carbon since they are a large source of airborne molecules.

Results from the simulation show that the contrast increases as the amorphous carbon increases, as would be expected. As with the results of graphene flake thickness, the trend here is linear (c = 3.9t + 2.17, where t is the carbon thickness). But it can also be seen that the peak wavelength slightly blue shifts on thicker films, following an exponential decay ($\lambda = 485 + 9.78e^{-2.2t}$). From these results, the sensitivity can be estimated. From the noise and experimental uncertainties in the optical contrast spectroscopy (figure 6.3), the detection limit is estimated to be about 0.5%. This is equivalent to an average

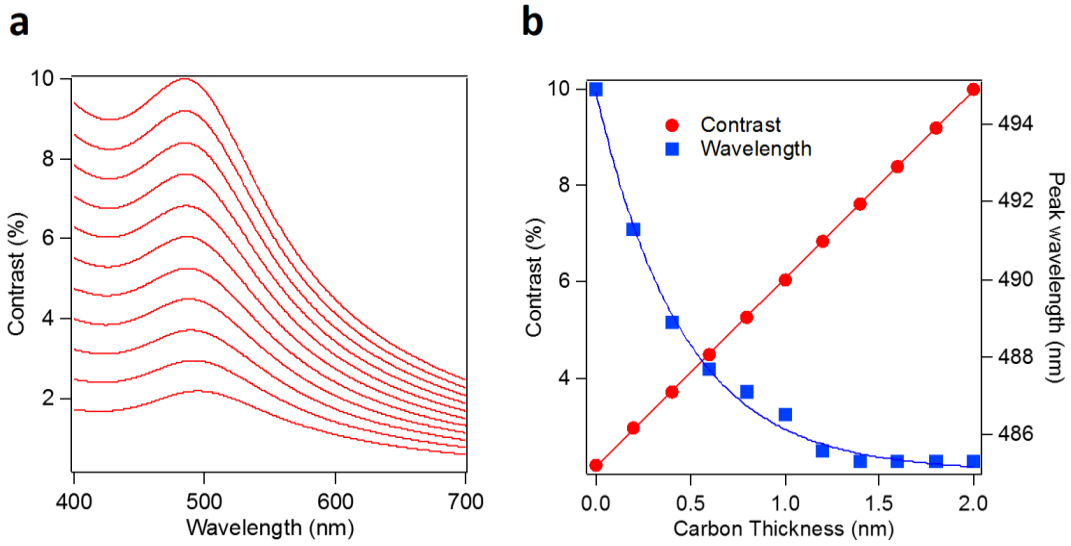

Figure 6.5 (a) Simulated contrast spectra of 0-2 nm (from bottom to top, 0.2 increment) amorphous carbon films adsorbed onto the graphene monolayer on a 100 nm bulk gold substrate. (b) Graph showing how the monolayer's contrast spectrum changes in peak wavelength and intensity as a function of the thickness of the amorphous carbon. The refractive index for amorphous carbon is taken from ref. 48

coverage of 0.13 nm amorphous carbon, which is about a third of a graphene monolayer.

This phenomenon was also examined experimentally. The samples containing the clean graphene which were previously examined were stored in unsealed plastic boxes in ambient conditions (after having been kept in nitrogen-filled desiccators during the initial experiments). This allowed the flakes to interact with the air without being covered by dust. The contrast was then measured after 2, 7, and 21 days of exposure to ambient conditions.

Results show in figure 6.6a that the contrast increases to be considerably higher than the clean samples. This is especially noticeable when the contrast increments for the different time intervals (i.e. 0-2 days, 2-7 days, and 7-21 days) are examined (figure 6.6b).

The increased contrast is mainly the result of physisorption of hydrocarbon molecules, which graphene and other 2D materials have been shown to adsorb

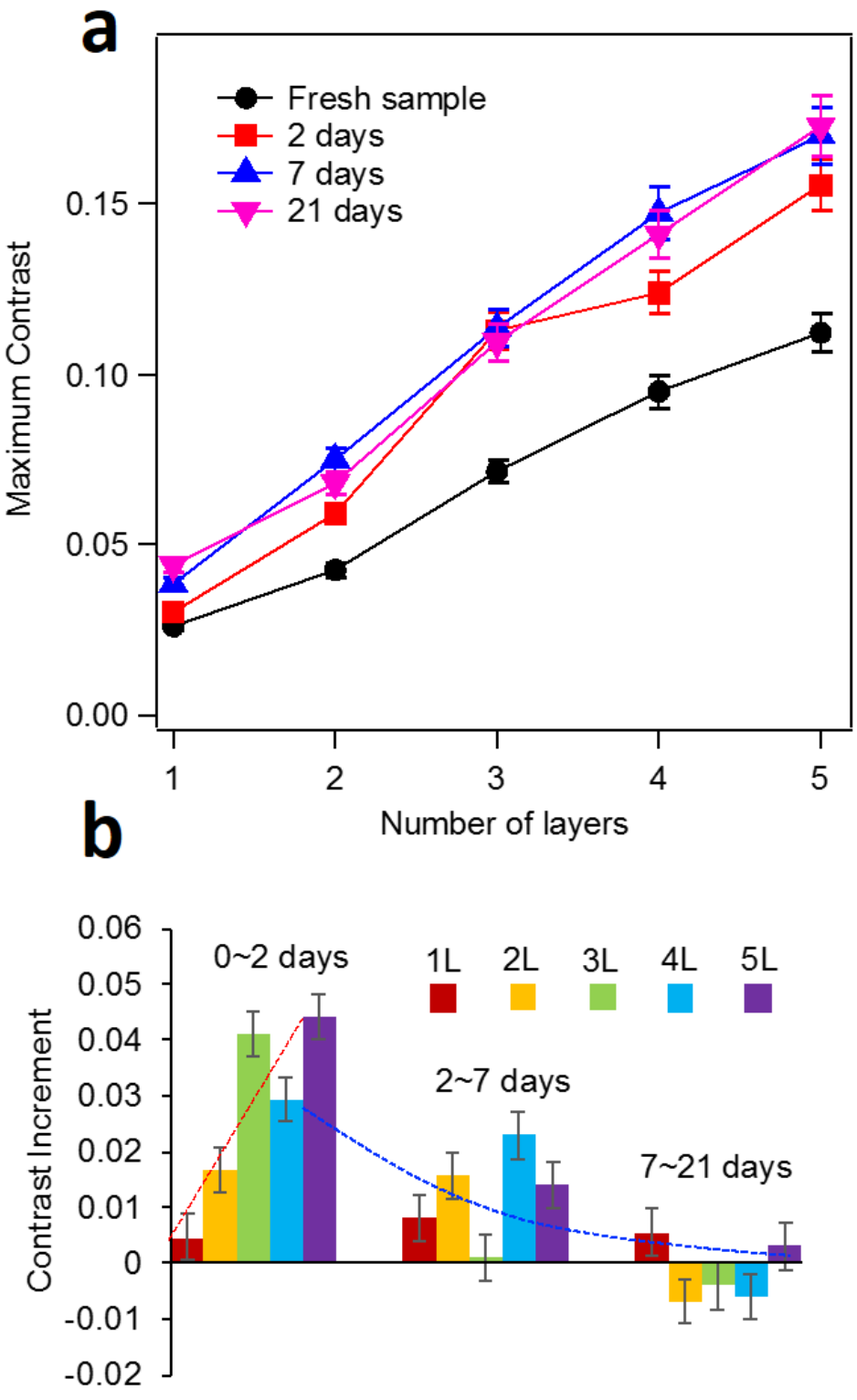

Figure 6.6 (a) Measured maximum optical contrast of freshly prepared graphene flakes before and after they were exposed to ambient conditions for 2, 7 and 21 days. (b) Increments of the optical contrast of the optical contrast of graphene flakes after exposure to the air. Dashed lines are for guidance. Standard errors are presented

in ambient environments[47,49-55]. This arises due to weak adhesion from Van der Waals forces. There is a large increase in the contrast intensity in the first two days. The increment then starts to rapidly slow down after about a week. This is consistent with previous wettability studies, which show an initial increase in the increase of the water contact angle, followed by a decline in the growth process[47,51,52]. The physisorption rate decreases rapidly with time exposed to air, and the increases seen in the 7-21 day period are below the system's detection limit.

It is also interesting to note that there is not uniform for flakes of different thickness. Figure 6.6b shows that thicker flakes acquire larger increments of contrast, which suggests thicker flakes adsorb more contamination than thin flakes. If there was uniform physisorption, the growth in the contrast would also be similar. Although there is a slight discrepancy in the trilayer sample (probably as a result drifting during the experiment), if it were in the expected range (given by the dashed box), it would be more in line with the trend of the other flakes.

Molecules can attach to 2D materials through strong electrostatic π-π interactions, which have been shown to be stronger in monolayers[54]. Previous studies have shown that Van der Waals forces increase with graphene film thickness and dominate the interactions, leading to more physisorption[47,53].

It has therefore been shown that the contrast of graphene is extremely sensitive to any molecular contamination. This is vital since graphene is used for such a wide variety of applications. One drawback however is that the contrast of monolayers on bulk gold is very small (~2.2%). This can be improved though if the graphene is deposited on other substrates such as 90 nm SiO_2/Si. This not only has increased contrast of the graphene monolayer (~12%)[33], but could also improve the geometry's sensitivity to detect amorphous carbon films as thin as 0.028 nm (assuming that the detection limit remains as 0.5%). This is because SiO_2/Si has a contrast gradient of 17.7%/nm

for amorphous carbon on monolayer graphene. When graphene has previously been used for sensing technology, it has required intricate techniques which rely on changes in the flake's electrical conductance or Forster energy transfer in the fluorescence[56,57]. Conversely, optical contrast spectroscopy is fast, easy, non-invasive, and can be miniaturised. This makes it an exciting new paradigm for sensors.

6.4 Conclusions

In conclusion, high-resolution contrast spectroscopy has been used to characterise the thickness of graphene flakes on bulk gold using a 100x magnification lens. This is an important development because graphene is frequently used in research and for other applications, and pristine flakes are required. Because of the large reflectivity of gold substrates, the contrast of monolayer graphene flakes is ~2.5%, much less than on SiO_2/Si substrates (~12%). Experimental results agree very well with simulations, which are based on a more detailed model that takes into account contributions from different light polarisations and a large range of incident angles. These contributions are important when a high numerical aperture lens is used. This chapter has also demonstrated that optical contrast spectroscopy can be exploited to detect adsorption of sub-atomic contamination molecules, thus opening up possibilities of developing miniaturised molecular sensors.

6.5 References

1. Novoselov, K.S. et al., *Electric field effect in atomically thin carbon films*, Science 306, no. 5696 (2004): 666-669
2. Giovannetti, G. et al., *Doping graphene with metal contacts*, Physical Review Letters 101, no. 2 (2008): 026803

3. Cooper, D.R. et al., *Experimental review of graphene*, ISRN Condensed Matter Physics 2012 (2012): 501686
4. Berger, C. et al., *Electronic confinement and coherence in patterned epitaxial graphene*, Science 312, no. 5777 (2006): 1191-1196
5. Berger, C. et al., *Ultrathin epitaxial graphite: 2D electron gas properties and a route toward graphene-based nanoelectronics*, The Journal of Physical Chemistry B 108, no. 52 (2004): 19912-19916
6. Bonaccorso, F., Sun, Z., Hasan, T. & Ferrari, A.C., *Graphene photonics and optoelectronics*, Nature Photonics 4, no. 9 (2010): 611-622
7. Bao, Q. & Loh, K.P., *Graphene photonics, plasmonics, and broadband optoelectronic devices*, ACS Nano 6, no. 5 (2012): 3677-3694
8. Wang, Q.H. et al., *Understanding and controlling the substrate effect on graphene electron-transfer chemistry via reactivity imprint lithography*, Nature Chemistry 4, no. 9 (2012): 724-732
9. Ni, Z.H. et al., *Raman spectroscopy of epitaxial graphene on a SiC substrate*, Physical Review B 77, no. 11 (2008): 115416
10. Xu, Y. et al., *Introducing electronic changes in graphene through silicon (100) substrate modification*, Nano Letters 11, no. 7 (2011): 2735-2742
11. Wu, L., Chu, H.S., Koh, W.S. & Li, E.P., *Highly sensitive graphene biosensors based on surface plasmon resonance*, Optics Express 18, no. 14 (2010): 14395-14400
12. Cai, J. et al., *Atomically precise bottom-up fabrication of graphene nanoribbons*, Nature 466, no. 7305 (2010): 470-473
13. Cai, Y., Zhu, J & Liu, Q.H., *Tunable enhanced optical absorption of graphene using plasmonic perfect absorbers*, Applied Physics Letters 106, no. 4 (2015): 043105
14. Mertens, J. et al., *Controlling subnanometre gaps in plasmonic dimers using graphene*, Nano Letters 13, no. 11 (2013): 5033-5038

15. Sigle, D.O. et al., *Monitoring morphological changes in 2D monolayer semiconductors using atom-thick plasmonic nanocavities*, ACS Nano 9, no. 1 (2014): 825-830
16. Sigle, D.O. et al., *Ultrathin CdSe in plasmonic nanogaps for enhanced photocatalytic water splitting*, The Journal of Physical Chemistry Letters 6, no. 7 (2015): 1099-1103
17. Chikkaraddy, R. et al., *Single-molecule strong coupling at room temperature in plasmonic nanocavities*, Nature 535, no. 7610 (2016): 127
18. Wu, Z.S. et al., *Synthesis of high-quality graphene with a pre-determined number of layers*, Carbon 47, no. 2 (2009): 493-499
19. Emtsev, K.V. et al., *Towards wafer-size graphene layers by atmospheric pressure graphitization of silicon carbide*, Nature Materials 8, no. 3 (2009): 203
20. Pu, N.W. et al., *Production of few-layer graphene by supercritical CO2 exfoliation of graphite*, Material Letters 63, no. 23 (2009): 1987-1989
21. Bae, S. et al., *Roll-to-roll production of 30-inch graphene films for transparent electrodes*, Nature Nanotechology 5, no. 8 (2010): 574-578
22. Jiao, L. et al., *Narrow graphene nanoribbons from carbon nanotubes*, Nature 458, no. 7240 (2009): 877
23. Hao, Y. et al., *Probing layer number and stacking order of few-layer graphene by Raman spectroscopy*, Small 6, no. 2 (2010): 195-200
24. Ferrari, A.C. et al., *Raman spectrum of graphene and graphene layers*, Physical Review Letters 97, no. 18 (2006): 187401
25. Yoon, D. et al., *Variations in the Raman spectrum as a function of the number of graphene layers*, Journal of the Korean Physical Society 55, no. 3 (2009): 1299-1303
26. Graf, D. et al., *Spatially resolved Raman spectroscopy of single- and few-layer graphene*, Nano Letters 7, no. 2 (2007): 238-242

27. Calizo, I. et al., *Variable temperature Raman microscopy as a nanometrology tool for graphene layers and graphene-based devices*, Applied Physics Letters 91, no. 7 (2007): 071913
28. Mohiuddin, T.M.G. et al., *Uniaxial strain in graphene by Raman spectroscopy: G peak splitting, Grüneisen parameters and sample orientation*, Physical Review B 79, no. 20 (2009): 205433
29. Stampfer, C. et al., *Raman imaging of doping domains in graphene on SiO_2*, Applied Physics Letters 91, no. 24 (2007): 241907
30. Lenski, D.R. & Fuhrer, M.S., *Raman and optical characterisation of multilayer turbostratic graphene grown via chemical vapour deposition*, Journal of Applied Physics 110, no. 1 (2011): 013720
31. Gorbachev, R.V. et al., *Hunting for monolayer boron nitride: optical and Raman signatures*, Small 7, no. 4 (2011): 465-468
32. Splendiani, A. et al., *Emerging photoluminescence in monolayer MoS_2*, Nano Letters 10, no. 4 (2010): 1271-1275
33. Ni, Z.H. et al., *Graphene thickness determination using reflection and contrast spectroscopy*, Nano Letters 7, no. 9 (2007): 2758-2763
34. Wlasny, I., Dabrowski, P. & Klusek, Z., *Optical contrast of single- and multi-layer graphene deposited on a gold substrate*, arXiv, (2011): 1102.4953
35. Horcas, I. et al., *WSxM: a software for scanning probe microscopy and a tool for nanotechnology*, Review of Scientific Instruments 78, no. 1 (2007): 013705
36. Blake, P. et al., *Making graphene visible*, Applied Physics Letters 91, no. 6 (2007): 063124
37. Born, M. & Wolf, E. *Principles of Optics* (7th ed.), page 54, 1999, Cambridge University Press, Cambridge
38. Rakic, A.D., Djurisic, A.B., Elazar, J.M. & Majewski, M.L., *Optical properties of metallic films for vertical-cavity optoelectronic devices*, Applied Optics 37, no. 22 (1998): 5271-5283

39. Wang, X., Chen, Y.P. & Nolte, D.D., *Strong anomalous optical dispersion of graphene: complex refractive index measured by Picometrology*, Optics Express 16, no. 26 (2008): 22105-22112
40. Falkovsky, L.A., *Optical properties of graphene*, Journal of Physics: Conference Series 129, no. 1 (2008): 012004
41. Ferrari, A.C. et al., *Raman spectrum of graphene and graphene layers*, Physical Review Letters 97, no. 18 (2006): 187401
42. Luo, Z. et al., *Thickness-dependent reversible hydrogenation of graphene layers*, ACS Nano 3, no. 7 (2009): 1781-1788
43. Wei, D. et al., *Synthesis of N-doped graphene by chemical vapour deposition and its electronic properties*, Nano Letters 9, no. 5 (2009): 1752-1758
44. Lee, J., Shim, S., Kim, B. & Shin, H.S., *Surface-enhanced Raman scattering of single- and few-layer graphene by the deposition of gold nanoparticles*, Chemistry— European Journal 17, no. 8 (2011): 2381-2387
45. Hawaldar, R. et al., *Large-area high-throughput synthesis of monolayer graphene sheet by hot filament thermal chemical vapor deposition*, Scientific Reports 2 (2012): 682
46. Lui, C.H. et al., *Ultraflat graphene*, Nature 462, no. 7271 (2009): 339
47. Li, Z. et al., *Effect of airborne contaminants on the wettability of supported graphene and graphite*, Nature Materials 12, no. 10 (2013): 925-931
48. Duley, W.W., *Refractive indices for amorphous carbon*, The Astrophysical Journal 287 (1984): 694-696
49. Velický, M. et al., *Electron transfer kinetics on mono- and multilayer graphene*, ACS Nano 8, no. 10 (2014): 10089-10100
50. Velický, M. et al., *Electron transfer kinetics on natural crystals of MoS2 and graphite*, Physical Chemistry Chemical Physics 17, no. 27 (2015): 17844-17853
51. Lai, C.Y. et al., *A nanoscopic approach to studying evolution in graphene wettability*, Carbon 80 (2014): 784-792

52. Aria, A.I. et al., *Time evolution of the wettability of supported graphene under ambient air exposure*, The Journal of Physical Chemistry C 120, no. 4 (2016): 2215-2224
53. Shih, C.J. et al., *Breakdown in the wetting transparency of graphene*, Physical Review Letters 109, no. 17 (2012): 176101
54. Cai, Q. et al., *Molecule-induced conformational change in boron nitride nanosheets with enhanced surface adsorption*, Advanced Functional Materials 26, no. 45 (2016): 8202-8210
55. Cai, Q. et al., *Boron nitride nanosheet-veiled gold nanoparticles for surface-enhanced Raman scattering*, ACS Applied Materials & Interfaces 8, no. 24 (2016): 15630-15636
56. Malic, Appel, Hofmann & Rubio, *Forster-induced energy transfer in functionalised graphene*, The Journal of Physical Chemistry C 118, no. 17 (2014): 9283-9289
57. Neri, *Thin 2D: the new dimensionality in gas sensing*, Chemosensors 5, no. 3 (2017): 21

Chapter 7

Tuning strong coupling of plexcitons at room temperature

7.1 Introduction

One of the advantages of using plasmonic technology is that it can be combined with molecular adsorbates to design components on the nanoscale, such as molecular circuits[1], active plasmonic devices[2,3], or optoelectronics[4]. Often, molecules are attached to nanoparticles to dramatically increase their Raman cross-section[5-7], to enhance or quench their fluorescence[8-10]. However, the molecule itself can also alter the plasmonic resonance of the nanoparticle[11], which is useful in developing molecular sensors[12-14].

Excitonic resonance is one of the most interesting characteristics of organic molecules[15]. These arise when incident radiation excites electrons in the molecule to a higher energy level, leaving behind a positively charged hole. A bound state forms between the two charged particles, which is a neutral quasiparticle known as an exciton[16-18]. When molecules are attached to plasmonic nanoparticles, these excitons can interact with the plasmons through an exchange of energy if there is an overlap between their resonances. As the interaction grows, the two enter a regime of strong coupling, where the energy transfer between the two is greater than the losses of the system, and hybridisation between the two creates states which are part matter and part light called plexcitons[19-21]. Such nanoparticle-molecule structures have unique properties which neither component possesses by itself. Normally, extremely low temperatures[22-24] are required to reduce losses in the system in order to

observe this phenomenon. The problem with this is that the properties of the particle or molecule can be compromised under such conditions. Therefore, it is more desirable to obtain strong coupling under ambient conditions. One way to achieve this is to confine the molecule inside a nanometre-sized plasmonic cavity. This is because the coupling strength scales inversely with the square root of the cavity volume, $g \propto \frac{1}{\sqrt{V}}$. Therefore, nanoparticle dimers with subnanometre gap sizes are ideal, since incident light is focused to such a small volume that the interaction time is increased dramatically. Furthermore, in such a small gap, the plasmonic hotspot is intense enough to enhance the molecule's fluorescence such that strong coupling can be achieved. This plasmonic geometry has previously been exploited to observe strong coupling at room temperature with J-aggregates in ambient conditions[25-27], as well as with other dye molecules[28-30].

In order to optimise the performance of strongly coupled nanophotonic devices, it is often necessary to tune the coupling strength[31,32]. This can either be achieved by using molecules with an excitonic resonance to match that of the plasmons[25,33], or by tuning the plasmonic resonance of the nanoparticle to match the molecule's excitonic resonance[34-36]. This can be difficult, however, because many factors in the environment affect not only the plasmonic resonance, but also the polarisation direction of the molecule. Therefore, much care must be taken to ensure that strong coupling can be actively tuned without being lost.

In this chapter, gold nanoparticles are deposited on top of monolayer graphene on a bulk gold substrate, forming the NPoM geometry, which has been used in plexcitonic strong coupling experiments[37,38]. It is ideal for this type of experiment because a NPoM with a subnanometre gap has been shown to have extremely strong enhancing effect that it overcomes[39] quenching effects that normally occur when a fluorescent molecule is near a plasmonic

particle, where the molecule is coupled to non-radiative higher order plasmonic modes that dissipate its energy[40]. It is also demonstrated that the NPoM is able to use the highly confined and strongly enhanced electric field inside its gap as a nanoscale heating source. This consequently carbonises hydrocarbon molecules attached to the particle, thereby facilitating the growth of single nanoscale graphene quantum dots (GQDs), to which the plasmons in the particle strongly couple. These are nanometre-sized fragments of graphene which have non-zero bandgaps[41], unlike their macro-sized counterparts. They are also very useful for use in bio-imaging[42] because they are non-toxic and have excellent photo-stability. By using the NPoM, GQDs can be reliably grown in a way that is less vigorous and contaminating than wet chemical methods. The GQDs are characterised using Raman spectroscopy and photoluminescence spectra, which show characteristic features in good agreement with literature[43,44].

Strong coupling between the plasmons of the particle and excitons of the GQDs is observed on optical scattering spectra. A graphene spacing layer ensures a robust sub-nanometre gap[45], which is important because the enhancing field increases exponentially with decreasing gap size[46,47]. It is also demonstrated that the coupling strength can be tuned through laser irradiation, which may give rise to tunable room-temperature optical devices based on single GQDs. Experimental results agree well with simulations.

7.2 Experimental

7.2.1 Sample preparation

Graphene and MoS_2 flakes were mechanically exfoliated onto a freshly sputtered 100 nm gold substrate. The thickness of the flakes was characterised through tapping mode AFM (figure 7.1) and Raman spectroscopy, using 532 and 633 nm lasers of 1 mW.

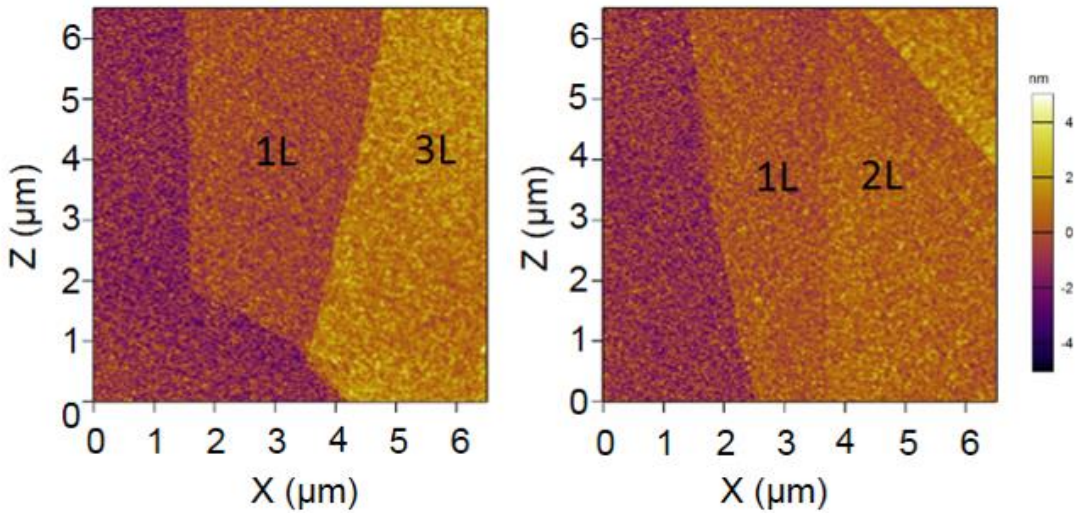

Figure 7.1 Tapping mode AFM images taken of graphene on bulk gold substrates. Images courtesy of Dr. Lu Hua Li's group in Deakin University, Australia

A 10 μL drop of spherical 90 nm gold nanoparticle solution (diluted by ten times in deionised water) was drop cast on top of the flakes. The sample was then rinsed in deionised water and dried with compressed gas.

7.2.2 Photoluminescence

In order to identify the source of excitons, fluorescence measurements were taken both on the nanoparticles and the substrates using lasers of wavelength 532, 543 and 594 nm, with powers 1 mW, 25 μW and 28 μW respectively. The fluorescence was analysed with a QE65 Ocean Optics optical spectrometer, coupled to the microscope with a 100 μm fibre optic cable.

7.3 Results

In addition to the AFM measurements taken on the graphene spacing layers discussed in section 7.2.1, Raman spectra were also taken to help verify their thickness (see figure 6.4c). These spectra clearly show distinct G-peaks (at ~1585 cm^{-1}) and 2D peaks (at ~2703 cm^{-1}), which is consistent with previous

studies[48,49]. Conversely, a strong D-peak is seen when Raman is measured from individual particles at ~1314 cm^{-1}, while the G-peak shifts slightly to ~1589 cm^{-1} and no 2D peak is visible (figure 7.2a). This suggests that the Raman measured from the particles does not originate from the underlying graphene spacing layer. This is also supported by examining the FWHM of the peaks. From the spectrum measured from a particle on monolayer graphene, the G-peak has a FWHM of ~64 cm^{-1}. This is wider than the peak from bare graphene on bulk gold substrates (~48 cm^{-1}). The presence of the D-peak indicates disorder in the carbon system, while its width is inversely related to the crystal size[50]. In this case, the D-peak are very narrow, suggesting that the carbon structures inside the gap have little disorder. This is in contrast to Raman measured from particles on monolayer MoS_2 (figure 7.2b), whose peaks are very broad. Narrow D-peaks like those in figure 7.2a are typical of Raman from GQDs[43,51,52] as a result of their nanometre-sized crystal structure. Photoluminescence spectra were also measured from nanoparticles on monolayer graphene to help confirm that the carbon source is GQDs. Although photoluminescence normally does not depend on wavelength of the excitation source, this is not the case for GQDs. Previous studies have shown that they redshift with excitation wavelength[43,51,53]. It is believed that this behaviour results from defects on the GQD's surface, which create additional energy bands to which electrons jump before recombining with its hole[54]. The photoluminescence spectra measured with 532, 543 and 594 nm lasers are shown in figure 7.3a (normalised with respect to the laser power). Although it is expected that intensity of the photoluminescence of the GQDs should decrease with increasing excitation wavelength, the 543 nm spectrum here is especially strong. This results from the resonant absorption $S_0 \rightarrow S_3$ transition[55]. The spectra show three peaks (figure 7.3b), which correspond to

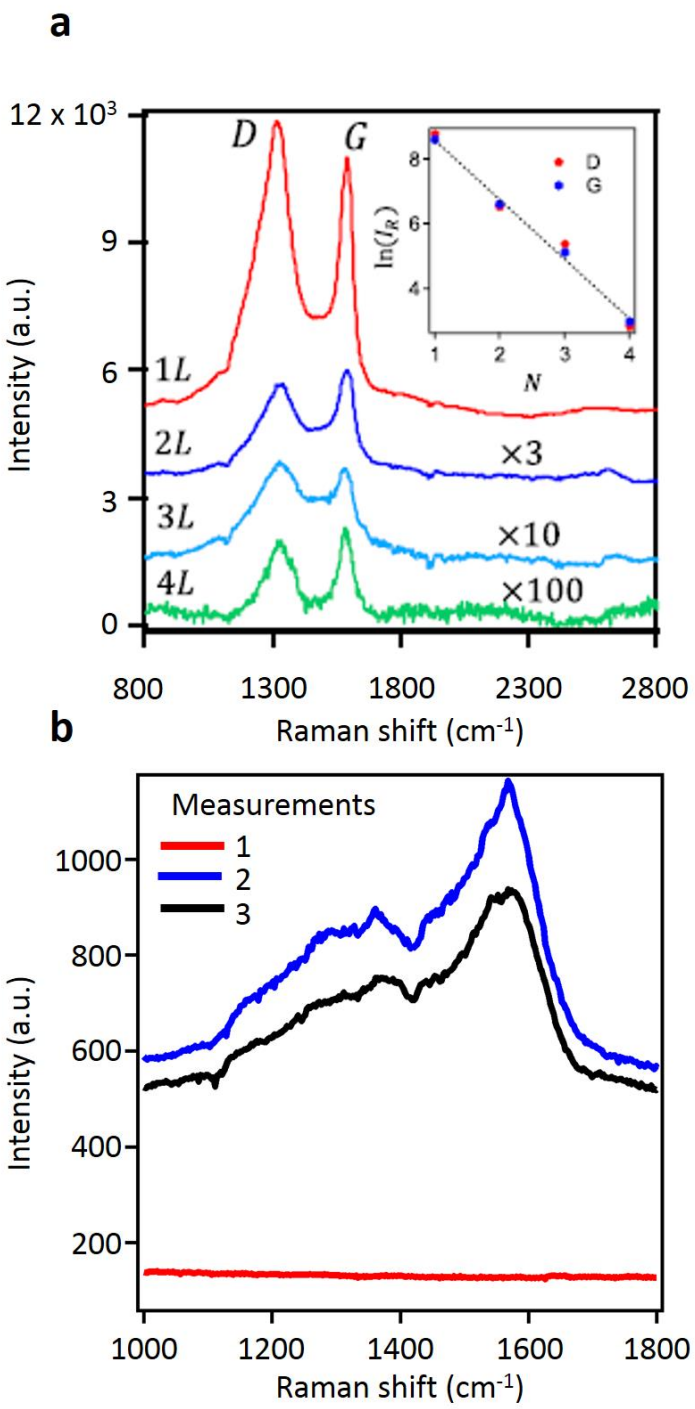

Figure 7.2 (a) SERS measured from Au NPs on 1-4L graphene films on a bulk Au substrate. Spectra taken from 2-4L are multiplied by factors shown on the graph. Inset shows Raman intensity against number of layers plotted in the natural log scale for (red pentagons) D-peaks and (blue hexagons) G-peaks. (b) Successively measured from a Au NP on monolayer MoS_2 spacing layer. No Raman signals were detected on (red) the first measurement, but strong D-peaks and G-peaks appear in subsequent measurements (blue and black). Raman was measured with 633 nm laser of 0.93 mW

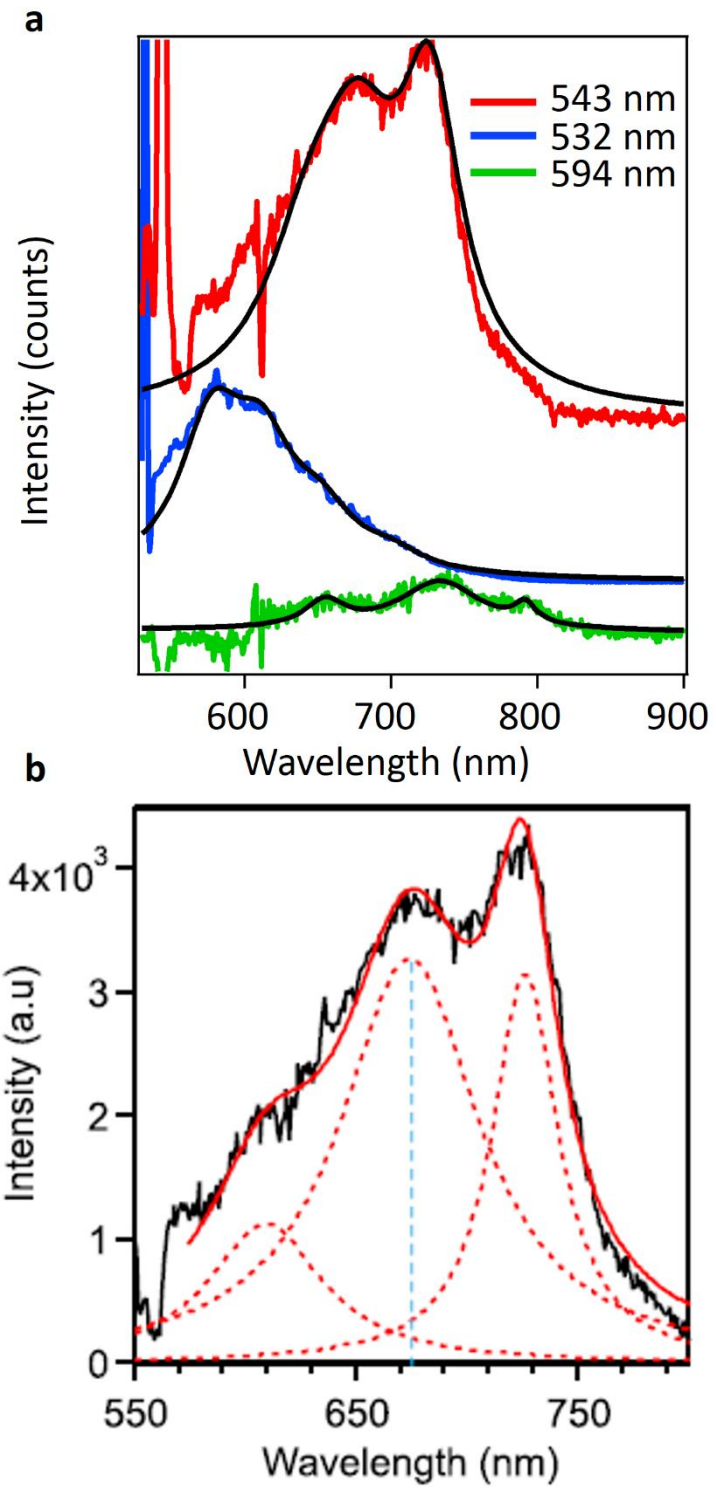

Figure 7.3 (a) Photoluminescence spectra measured from a Au NP on monolayer graphene excited at (red) 543 nm, (blue) 532 nm and (green) 594 nm. This demonstrates the wavelength dependent behaviour of the GQDs. Data has been normalised with respect to laser power and offset for clarity. Fitted data is shown in black. (b) Measured photoluminescence of the Au NP with the 543 nm laser composed of three emission modes (dashed lines)

the triplet electronic states of individual GQDs[44]. The peak at 674 nm is a fluorescent mode, while the longer wavelength mode at 727 nm is a phosphorescent mode[44]. The fluorescent mode's resonance wavelength overlaps with the plasmonic mode in the nanoparticle on monolayer graphene, and therefore leading to strong coupling, as will be demonstrated later on. Although strong coupling between excitons and plasmons usually requires low temperatures in a microcavity for a high enough Q-factor, the sub-nanometric volume inside the plasmonic gap provide enough enhancement to observe it at room temperature[37-39]. The strong coupling is evident from the scattering spectra. Optically, particles on monolayer graphene appear red, whereas those on bare gold appear green (figure 7.4a).

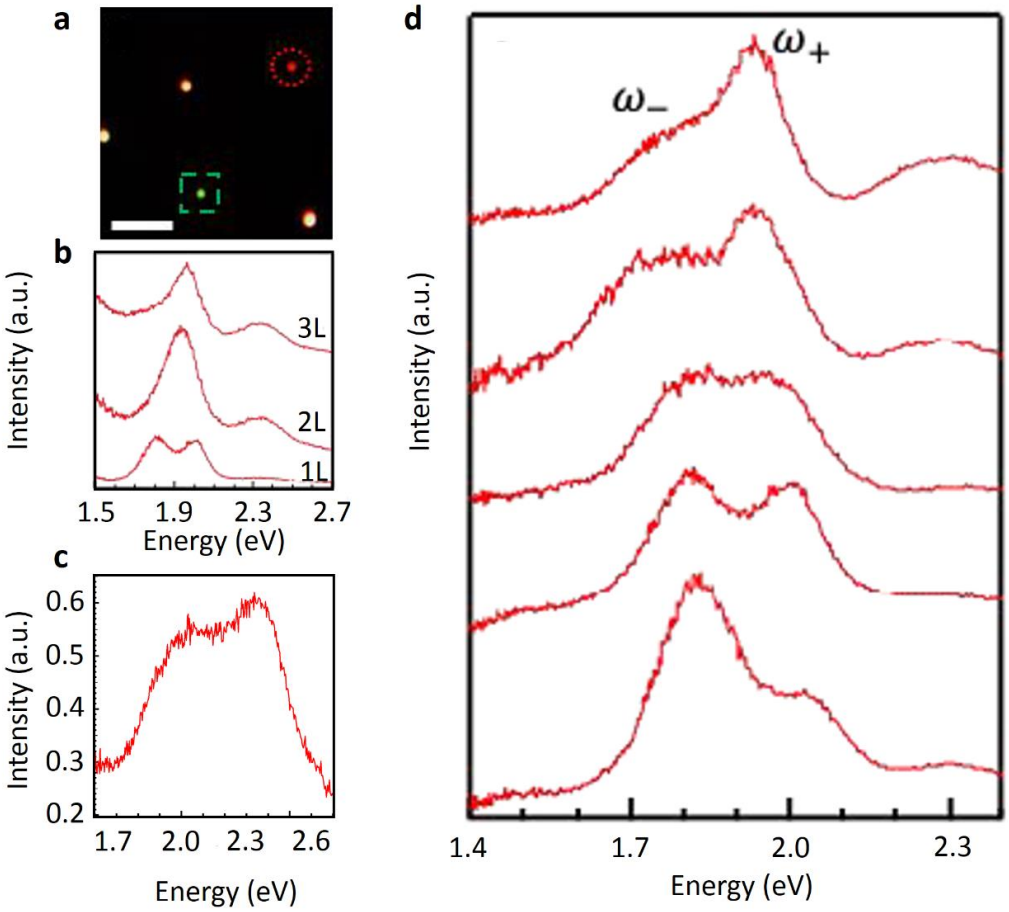

Figure 7.4 (a) Dark-field optical images of Au NPs on (red circle) monolayer graphene and (green square) on bare Au. Scale bar represents 2 μm. (b) Scattering spectra from Au NPs on 1-3L graphene. (c) Scattering spectra from Au NP on monolayer MoS_2. (d) Scattering spectra from various Au NPs on monolayer graphene

Although particles on graphene still show the high energy transverse peak at ~2.3 eV, the spectra also show distinct double peaks between 1.8 and 2.0 eV. Interestingly, these double peaks only appear on monolayer graphene, but not on either thicker layers (figure 7.4b) or on monolayer MoS_2 (figure 7.4c). This is because the enhancement decreases due to a larger gap size. The double peak feature is, however, consistent for particles on monolayer graphene (figure 7.4d).

It was further found that the double-peak feature can be tuned through laser irradiation. This was investigated by irradiating a particle with a low powered 532 nm laser (75 μm, focused with a 100x magnification objective lens, NA=0.9) for 10 seconds, after which the scattering was re-measured (with the laser turned off). The initial double peaks merge into one after only 90 seconds (figure 7.5a).

Strong coupling between plasmons and excitons can be modelled as a semi-classical coupled oscillator, where the frequency of the two splitting modes is given by:

$$\omega_{\pm} = \frac{(\omega_{sp}+\omega_0)}{2} \pm \sqrt{g^2 + \frac{\delta^2}{4}} \tag{7.1}$$

where $\delta = \omega_{sp} - \omega_0$, ω_{sp} and ω_0 are the energies of the plasmonic mode and emitter respectively, g is the coupling strength, which (as discussed earlier) is inversely proportional to the square root of the cavity volume.

The Rabi splitting energy, Ω, is given by the difference between the upper (ω_+) and lower branches (ω_-), such that:

$$\Omega \equiv \omega_+ - \omega_- = 2\sqrt{g^2 + \frac{\delta^2}{4}} \tag{7.2}$$

By fitting the spectra with Lorentzian, information can be obtained about the energies of the resonant peaks. Fittings give a value for the plasmonic mode

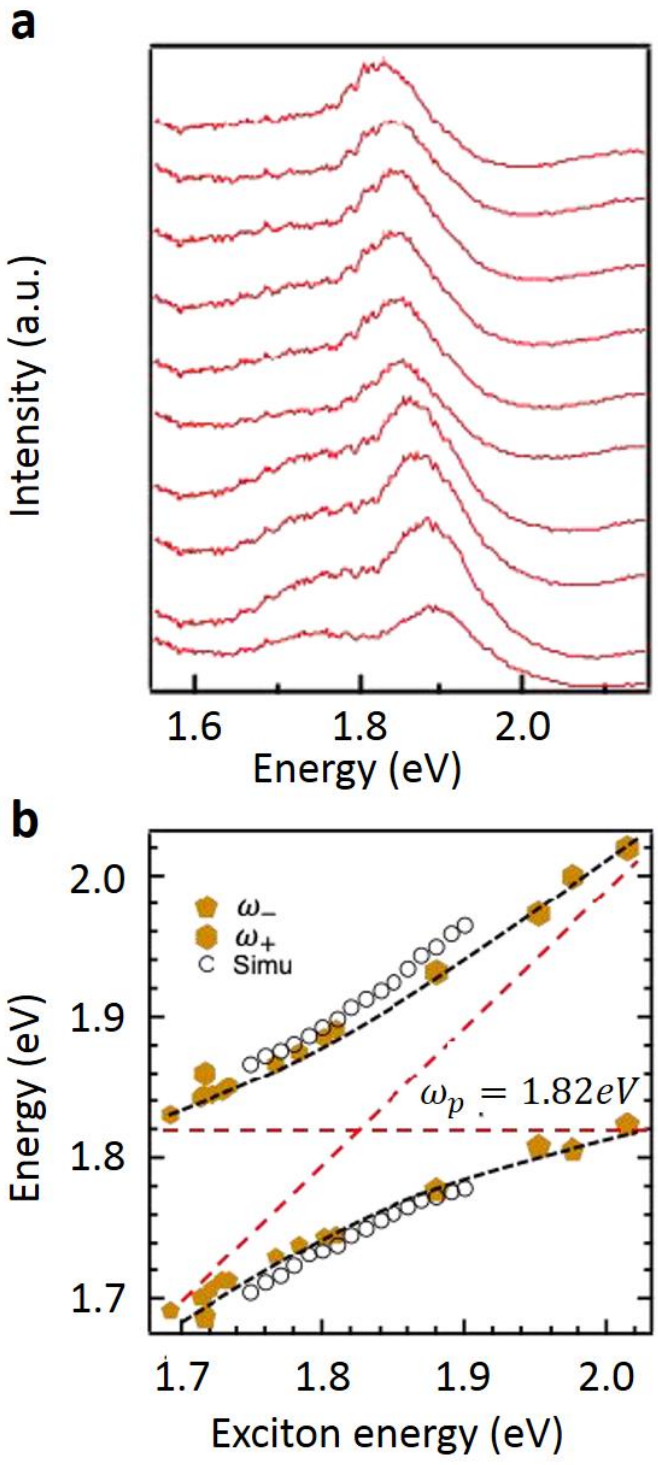

Figure 7.5 (a) Scattering spectra from a Au NP on monolayer graphene, irradiated by a 532 nm laser (75 μW) for ten second intervals starting from 0 seconds at the bottom and 90 seconds at the top. (b) Dispersion diagram showing the dependence of the energy of the split peaks (ω_+ and ω_-) on the exciton energy. Filled symbols represent measured data from the NP in (a) and 7.4d, while the empty circles represent simulated data

as 1.82 ± 0.1 eV. When the results of the double peaks are plotted, an anti-crossing relation between the two modes, which is typical of strong coupling (figure 7.5b). Rabi splitting energy here ranges from ~140 meV under resonant conditions (when $\omega_0 = \omega_{sp}$ = 1.82 eV, giving $\delta = 0$). These are comparable to other plexciton experiments[25,26,37]. In order for strong coupling to occur, the condition $\Omega > \frac{\gamma_{SP}+\gamma_0}{2}$, where γ_{sp} and γ_0 are the decay rates of the plasmon and exciton respectively. Since $\gamma_{SP} + \gamma_0 = \gamma_+ + \gamma_-$ (where γ_+ and γ_- are the FWHM of the two splitting modes ω_+ and ω_- respectively)[56], the experimental results give $\frac{\gamma_+ + \gamma_-}{2} \approx$ 130 meV, thus fulfilling the condition.

It is known that hydrocarbon molecules commonly adsorb to the surface of gold both in ambient[48] and vacuum conditions[57]. When these molecules are subjected to intense electric fields or increased temperatures, they can be carbonised into carbon nanostructures, or even crystallised GQDs or graphene if the field is especially strong such as in the gap of a NPoM structure[55,58,59]. In this experiment, carbonisation happens almost instantly during the Raman measurements as a result of strong field enhancements. This allows the carbon signal to appear in the Raman spectra taken from particles on monolayer graphene from the first measurements. This is in contrast to when spectra were taken from particles on monolayer MoS_2. Because there is a much smaller enhancement field for NPoMs on MoS_2, there is often no carbon signal observed on the first measurement, and it does not appear until subsequent measurements (figure 7.2b). This confirms that crystallised carbon structures only form under the influence of an extremely high electric field inside the nanogap, and not as a result of underlying graphene or any pre-existing carbon structure on the particle. Simulations in figure 7.6a show that the field is tightly concentrated and strongly enhanced in the gap. At its centre, it is approximately 320 fold more than that of the incident field (figure 7.6b). Simulated scattering spectra of a particle on monolayer graphene where

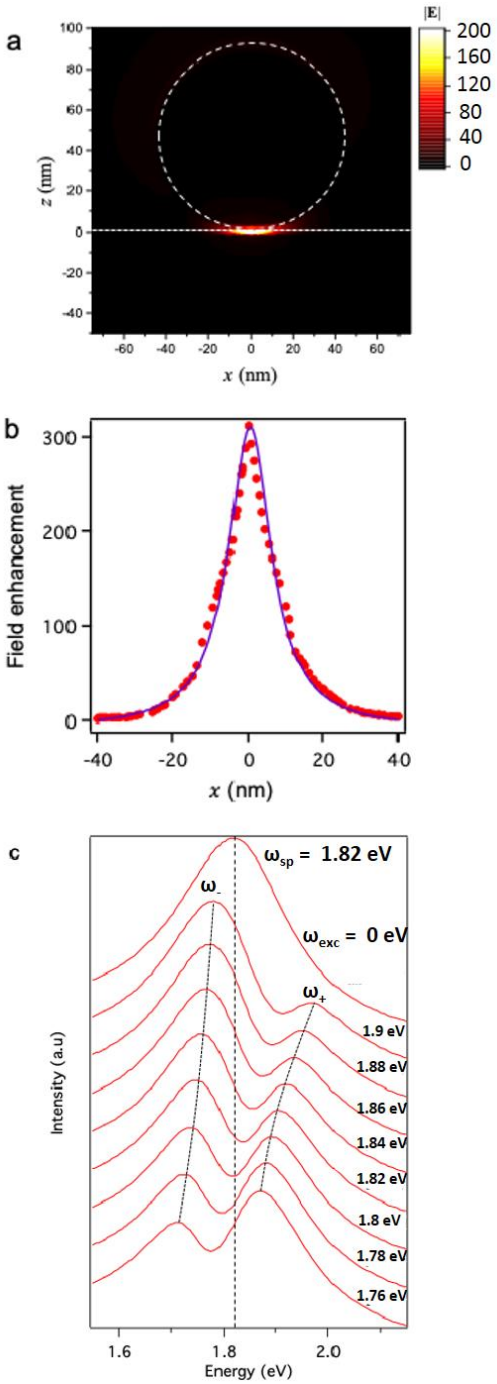

Figure 7.6 (a) Simulated near-field distribution inside the NPoM gap, excited by a 685 nm laser. The NP's shape is indicated by the white dashed line. (b) The profile of the enhancing field inside the nanogap. This is fitted with a Lorentzian profile (solid line). (c) Scattering spectra of NP on monolayer graphene as a function of exciton energy. The top spectrum represents no coupling ($\omega_{exc} = 0$) at the top, indicating a plasmonic mode of 1.82 eV (shown by the dashed line). Dashed lines represent the split peaks which result from strong coupling. The energies of the modes are shown in 7.5b. Courtesy of Dr. Tserkezis

plasmons in the particle are coupled to excitons of varying strength are shown in figure 7.6c. Data from the simulations are shown alongside the experimental data, and it can be seen that there is excellent agreement between the two in both cases. From the Raman spectra, it is possible to estimate the size of the GQDs, based on the intensity ratio of the D-peak and G-peak[60]. From Raman spectra of particles on monolayer graphene, a ratio can be seen of $\frac{I_D}{I_G} \approx 1.2$. This corresponds to a crystallite size of GQD of ~ 4 ± 1 nm[60], a value that is close to theoretical calculations[42]. The GQD form oxygen functional groups at the edge, causing a redshift in the photoluminescence energy[41,42]. After the irradiation, the metastable high energy oxidation states reverts to its initial low energy state through a slow reduction process at room temperature. This results in the scattering spectrum slowly recovering over tens of hours (figure 7.7).

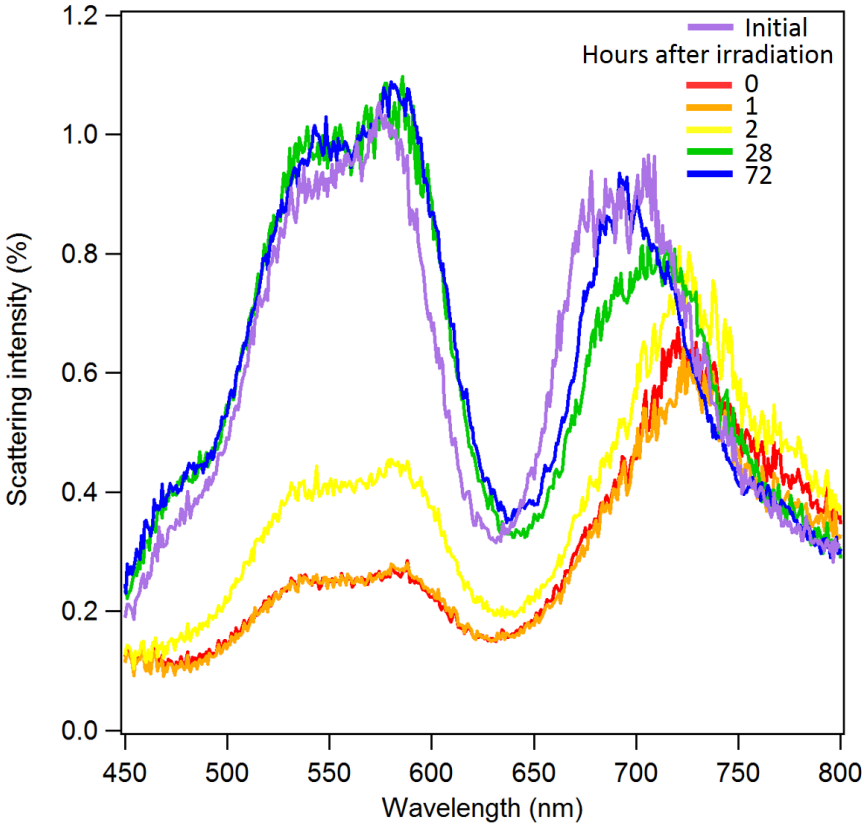

Figure 7.7 Scattering spectra of a NP on monolayer graphene measured (purple) before laser irradiation, (red) directly after, (orange) 1 hour, (yellow) 2 hours, (green) 28 hours, and (blue) 72 hours after laser irradiation

7.4 Conclusions

It has been shown that the NPoM geometry can be used to grow graphene quantum dots within its plasmonic nanocavity. This is facilitated by intense optical near fields inside the gap. This opens up a new pathway to manufacture individual GQDs, and will empower their research and applications, so that their intrinsic properties can be systematically investigated. The strong enhancing field also induces strong coupling between plasmons in the particle and excitons in the GQDs. This is indicated by the split double peaks in the optical scattering spectra, as well as the characteristic anti-crossing behaviour. It has also been shown that the strong coupling can be tuned through laser irradiation, which may give rise to the development of tunable quantum optical devices at room temperature.

7.5 References

1. Banerjee, P. et al., *Plasmon-induced electrical conduction in molecular devices*, ACS Nano 4, no. 2 (2010): 1019-1025
2. Andrew, P. & Barnes, W.L., *Energy transfer across a metal film mediated by surface plasmon polaritons*, Science 306, no. 5698 (2004): 1002-1005
3. Wurtz, G.A., et al., *Molecular plasmonics with tunable exciton-plasmon coupling strength in J-aggregate hybridised Au nanorod assemblies*, Nano Letters 7, no. 5 (2007): 1297-1303
4. Galperin, M. & Nitzan, A., *Molecular optoelectronics: the interaction of molecular conduction junctions with light*, Physical Chemistry Chemical Physics 14, no. 26 (2012): 9421-9438
5. Jiang, T., Wang, X., Zhou, J. & Jin, H., *The construction of silver aggregate with inbuilt Raman molecule and gold nanowire forest in SERS-based immunoassay for cancer biomarker detection*, Sensors and Actuators B: Chemical 258 (2018): 105-114

6. Zhu, T. et al., *A novel SERS nanoprobe based on the use of core-shell nanoparticles with embedded reporter molecule to detect E. coli O157: H7 with high sensitivity*, Microchimica Acta 185, no. 1 (2018): 30
7. Zhang, L. et al., *Cellulose nanofiber textured SERS substrate*, Colloids and Surfaces A: Physicochemical and Engineering Aspects 468 (2015): 309-314
8. Ray, K., Badugu, R. & Lakowicz, J.R., *Metal-enhanced fluorescence from CdTe nanocrystals: a single molecule fluorescence study*, Journal of the American Chemical Society 128, no. 28 (2006): 8998-8999
9. Lakowicz, J.R., *Plasmonics in biology and plasmon-controlled fluorescence*, Plasmonics 1, no. 1 (2006): 5-33
10. Bharadwaj, P., Anger, P. & Novotny, L., *Nanoplasmonic enhancement of single-molecule fluorescence*, Nanotechnology 18, no. 4 (2006): 044017
11. Zhang, W., Huang, L., Santschi, C. & Martin, O.J.F., *Trapping and sensing 10 nm metal nanoparticles using plasmonic dipole antennas*, Nano Letters 10, no. 3 (2010): 1006-1011
12. Zhao, J., Sherry, L.J., Schatz, G.C. & Van Duyne, R.P., *Molecular plasmonics: Chromophore-plasmon coupling and single-particle nanosensors*, IEEE Journal of Selected Topics in Quantum Electronics 14, no. 6 (2008): 1418-1429
13. Joshi, G.K. et al., *Ultrasensitive photoreversible molecular sensors of azobenzene-functionalized plasmonic nanoantennas*, Nano Letters 14, no. 2 (2014): 532-540
14. Tao, Y. et al., *Gold nanoshells with gain-assisted silica core for ultra-sensitive bio-molecular sensors*, Optics Communications 349 (2015): 193-197
15. Wu, N., Feist, J. & Garcia-Vidal, F.J., *When polarons meet polaritons: Exciton-vibration interactions in organic molecules strongly coupled to confined light fields*, Physical Review B 94, no. 19 (2016): 195409

16. Elliott, R.J., *Intensity of optical absorption by excitons*, Physical Review 108, no. 6 (1957): 1384
17. Brus, L.E., *Electron-electron and electron-hole interactions in small semiconductor crystallites: The size dependence of the lowest excited electronic state*, The Journal of Chemical Physics 80, no. 9 (1984): 4403-4409
18. Levinson, Y.B. & Rashba, E.I., *Electron-phonon and exciton-phonon bound states*, Reports on Progress in Physics 36, no. 12 (1973): 1499
19. Fofang, N.T. et al., *Plexciton dyanmics: exciton-plasmon coupling in a J-aggregate-Au nanoshell complex provides a mechanism for nonlinearity*, Nano Letters 11, no. 4 (2011): 1556-1560
20. Yuen-Zhou, J. et al., *Plexciton Dirac points and topological modes*, Nature Communications 7 (2016): 11783
21. Ozel, T. et al., *Observation of selective plasmon-exciton coupling in nonradiative energy transfer: donor-selective versus acceptor-selective plexcitons*, Nano Letters 13, no. 7 (2013): 3065-3072
22. Peter, E. et al., *Exciton-photon strong-coupling regime for a single quantum dot embedded in a microcavity*, Physical Review Letters 95, no. 6 (2005): 067401
23. Regal, C.A., Teufel, J.D. & Lehnert, K.W., *Measuring nanomechanical motion with a microwave cavity interferometer*, Nature Physics 4, no. 7 (2008): 555
24. Faraon, A. et al., *Coherent generation of non-classical light on a chip via photon-induced tunnelling and blockade*, Nature Physics 4, no. 11 (2008): 859
25. Schlather, A.E. et al., *Near-field mediated plexcitonic coupling and giant Rabi splitting in individual metallic dimers*, Nano Letters 13, no. 7 (2013): 3281-3286
26. Fedele, S. et al., *Strong coupling in molecular exciton-plasmon Au nanorod array systems*, Applied Physics Letters 108, no. 5 (2016): 053102

27. Fofang, N.T. et al., *Plexcitonic nanoparticles: plasmon-exciton coupling in nanoshell- J-aggregate complexes*, Nano Letters 8, no. 10 (2008): 3481-3487
28. Vakevainen, A.I. et al., *Plasmonic surface lattice resonances at the strong coupling regime*, Nano Letters 14, no. 4 (2013): 1721-1727
29. Shi, L. et al., *Spatial coherence properties of organic molecules coupled to plasmonic surface lattice resonances in the weak and strong coupling regimes*, Physical Review Letters 112, no. 15 (2014): 153002
30. Cade, N.I., Ritman-Meer, T. & Richards, D., *Strong coupling of localised plasmons and molecular excitons in nanostructured silver films*, Physical Review B 79, no. 24 (2009): 241404
31. Liu, J.Q. et al., *Tunable plasmonic dispersion and strong coupling in graphene ribbon and double layer sheets structure*, Plasmonics 12, no. 2 (2017): 309-314
32. Jun, Y.C. et al., *Epsilon-near-zero strong coupling in metamaterial-semiconductor hybrid structures*, Nano Letters 13, no. 11 (2013): 5391-5396
33. Valmorra, F. et al., *Strong coupling between surface plasmon polariton and laser dye rhodamine 800*, Applied Physics Letters 99, no. 5 (2011): 051110
34. Nagasawa, F., Takase, M. & Murakoshi, K., *Raman enhancement via polariton states produced by strong coupling between a localised surface plasmon and dye excitons at metal nanogaps*, The Journal of Physical Chemistry Letters 5, no. 1 (2013): 14-19
35. Chantharasupawong, P., Tetard, L. & Thomas, J., *Coupling enhancement and giant Rabi-splitting in large arrays of tunable plexcitonic substrates*, The Journal of Physical Chemistry C 118, no. 41 (2014): 23954-23962
36. Srinivasan, V., Manne, A.K., Patnaik, S.G. & Ramamurthy, S.S., *Cellphone monitoring of multi-qubit emission enhancements from Pd-carbon plasmonic nanocavities in tunable coupling regimes with attomolar sensitivity*, ACS Applied Materials & Interfaces 8, no. 35 (2016): 23281-23288

37. Chikkaraddy, R. et al., *Single-molecule strong coupling at room temperature in plasmonic nanocavities*, Nature 535, no. 7610 (2016): 127

38. Kleemann, M.E. et al., *Strong-coupling of WSe_2 in ultra-compact plasmonic nanocavities at room temperature*, Nature Communications 8, no. 1 (2017): 1296

39. Kongsuwan, N. et al., *Suppressed quenching and strong coupling-enhanced of Purcell-enhanced single-molecule emission in plasmonic nanocavities*, ACS Photonics 5, no. 1 (2017): 186-191

40. Dulkeith, E. et al., *Fluorescence quenching of dye molecules near gold nanoparticles: radiative and nonradiative effects*, Physical Review Letters 89, no. 20 (2002): 203002

41. Bacon, M., Bradley, S.J. & Nann, T., *Graphene quantum dots*, Particle & Particle Systems Characterisation 31, no. 4 (2014): 415-428

42. Li, X. et al., *Carbon and graphene quantum dots for optoelectronic and energy devices: a review*, Advanced Functional Materials 25, no. 31 (2015): 4929-4947

43. Peng, J. et al., *Graphene quantum dots derived from carbon fibers*, Nano Letters 12, no. 2 (2012): 844-849

44. Sk, M.A. et al., *Revealing the tunable photoluminescence properties of graphene quantum dots*, Journal of Materials Chemistry C 2, no. 34 (2014): 6954-6960

45. Muszynski, R., Seger, B. & Kamat, P.V., *Decorating graphene sheets with gold nanoparticles*, The Journal of Physical Chemistry C 112, no. 14 (2008): 5263-5266

46. Huang, F.M. et al., *Dressing plasmons in particle-in-cavity architectures*, Nano Letters 11, no. 3 (2011): 1221-1226

47. Ciraci, C. et al., *Probing the ultimate limits of plasmonic enhancement*, Science 337, no. 6098 (2012): 1072-1074

48. Katzen, J. et al., *A rigorous and accurate contrast spectroscopy for ultimate thickness determination of micrometre-sized graphene on gold and molecular sensing*, ACS Applied Material and Interfaces 10 (2018): 22520-22528
49. Velický, M. et al., *Optimising the visibility of graphene and graphene oxide on gold with multilayer heterostructures*, Nanotechnology 29, no. 27 (2018): 275205
50. Chu, P.K. & Li, L., *Characterisation of amorphous and nanocrystalline carbon films*, Materials Chemistry and Physics 96, no. 2-3 (2006): 253-277
51. Pan, D., Zhang, J., Li, Z. & Wu, M., *Hydrothermal route for cutting graphene sheets into blue-luminescent graphene quantum dots*, Advanced Materials 22, no. 6 (2010): 734-738
52. Gan, Z., Xu, H. & Hao, Y., *Mechanism for excitation-dependent photoluminescence from graphene quantum dots and other graphene oxide derivates: consensus, debates and challenges*, Nanoscale 8, no. 15 (2016): 7794-7807
53. Mueller, M.L., Yan, X., McGuire J.A. & Li, L.S., *Triplet states and electronic relaxation in photoexcited graphene quantum dots*, Nano Letters 10, no. 7 (2010): 2679-2682
54. Zhu, S. et al., *Strongly green-photoluminescent graphene quantum dots for bioimaging applications*, Chemical Communications 47, no. 24 (2011): 6858-6860
55. Kim, J. & Suh, J.S., *Size-controllable and low-cost fabrication of graphene quantum dots using thermal plasma jet*, ACS Nano 8, no. 5 (2014): 4190-4196
56. Tormä, P. & Barnes W.L., *Strong coupling between surface plasmon polaritons and emitters: a review*, Reports on Progress in Physics 78, no. 1 (2014): 013901

57. Velický, M. et al., *Mechanism of gold-assisted exfoliation of centimetre-sized transition-metal dichalcogenide monolayers*, ACS Nano 12, no. 10 (2018): 10463-10472

58. Rodríguez-Manzo, J.A., Pham-Huu, C. & Banhart, F., *Graphene growth by a metal-catalysed solid-state transformation of amorphous carbon*, ACS Nano 5, no. 2 (2011): 1529-1534

59. Zheng, M. et al., *Metal-catalysed crystallisation of amorphous carbon to graphene*, Applied Physics Letters 96, no. 6 (2010): 063110

Tuinstra, F. & Koenig, J.L, *Raman spectrum of graphite*, The Journal of Physical Chemistry 53, no. 3 (1970): 1126-1130

Chapter 8
Conclusion and future prospects

In this thesis, a comprehensive investigation into the fundamentals of the plasmonics of a gold nanosphere coupled to a reflective substrate has been carried out using optical dark-field scattering. By examining particles coupled to substrates of different optical and reflective properties, the origin of each of the resonant modes has been identified, thus giving more information about the physics of a particle coupling to a substrate. These results are consistent with previous theoretical results of nanoparticles, and provide a useful continuation of experimental work using nanotips. Since the NPoM geometry is now commonly used, it is important that its fundamentals be understood so that it can be utilised to its full potential. It has been demonstrated that the resonant modes can be tuned in both wavelength and intensity in a simple and consistent way. This is especially important for the gap plasmon, where the enhancing hotspot is located. The ability of a plasmonic particle to focus light to a gap, and the ability to tune the field inside the gap (and hence the enhancement) means that the NPoM can be integrated into a range of optical devices to improve their efficiencies.

The NPoM's potential has also been demonstrated in achieving strong coupling between plasmons and excitons. In subnanometre gaps, the NPoM's enhancement is strong enough to overcome quenching effects of a molecule's fluorescence which normally occurs near a nanoparticle by coupling the fluorescence to radiative higher-order modes. In larger spacings, the enhancement quickly decreases, the fluorescence is quenched, and strong coupling is lost. Such an observation is important should this technology be

developed in the future. Furthermore, the ability to actively tune the coupling strength at optical wavelengths was demonstrated, by using a low-powered laser to gradually photobleach the molecules and supress their fluorescence. This will be very useful in the advancement of plasmonic-molecule hybridised devices, but has not been reported in previous literature. This study only examined strong coupling with carbon molecules, but by making small changes to the nanoparticle's local environment, the gap plasmon could potentially be tuned to match the excitonic resonance of other molecules without compromising the strong coupling with the plasmons. This may lead to the development of new plexcitonic devices with interesting properties specific to their molecules. Moreover, it would be interesting to carry out further detailed studies into how the gap plasmon can grow the carbon molecules. One first step would be to work out the temperature inside the gap. This could be achieved by measuring surface-enhanced Raman scattering background for a nanoparticle on a non-conductive substrate at a known temperature.

This thesis has also developed a more accurate method for characterising the thickness of graphene flakes though contrast spectra, which are then compared to simulations. It is hoped that this method can be developed into an atomic molecule detector. In order to do this, the next step would be to add known amounts of a particular molecule into the environment of a clean piece of graphene, in order to carry out a systematic analysis. It could also be extended to characterise other 2D material flakes such as hexagonal boron nitride, MoS_2, or graphene oxide.

It should be noted that this thesis focused on the scattering properties of gold nanospheres. However, in the future it would also be interesting to examine how its other optical processes such as absorption are affected under similar conditions, so that it can be integrated into applications such as solar panels,

plasmonic circuits, and nanolasers. It would also be interesting to carry out a similar study using other commonly shaped nanoparticles, such as nanorods or nanoshells, to better understand how their optical properties change, as well as other plasmonic materials such as silver or copper.

List of publications

- Katzen, J., Velický, M., Huang, Y., Drakeley, S., Hendren, W., Bowman, R.M., Cai, Q., Chen, Y., Li, L.H. & Huang, F., *A rigorous and accurate contrast spectroscopy for ultimate thickness determination of micrometre-sized graphene on gold molecular sensing*, ACS Applied Materials and Interfaces (2018): 1-9
- Velický, M., Hendren, W., Donnelly, G.E., Katzen, J., Bowman, R.M. & Huang, F., *Optimising the visibility of graphene and graphene oxide on gold with multilayer heterostructures*, Nanotechnolgy 29, no. 27 (2018): 275205
- Katzen, J., Velický, M., Drakeley, S., Hendren, W., Bowman, R.M., Cai, Q., Chen, Y., Li, L.H., Tserkezis, C. & Huang, F., *Single graphene quntum dot fabrication and strong coupling in plasmonic nanocavities*, in progress
- Katzen, J., Ali, A., Velický, M., Hendren, W., Bowman, R.M. & Huang, F., *A systematic analysis of the generation of plasmonic resonance in a sphere-on-mirror geometry*, in progress
- Katzen, J., Tserkezis, C., Cai, Q., Chen, Y., Li, L.H., Yi, G.R., Santos, E.J. & Huang, F., *Fabricating and strongly coupling graphene quantum dots in plasmonic nanocavities*, Poster to be presented at: SPP9 2019 May 26-31 Copenhagen
- Katzen, J., Velický, M., Drakeley, S., Hendren, W., Cai,, Q., Chen, Y., Li, L.H. Yi, G.R. & Huang, F., *Plasmonic coupling of nanoparticles in the subnanometre regime*, Poster presented at: Photonics Ireland 2017 Sep 13-15 Galway
- Katzen, J., Murphy, A. Pollard, R. & Huang, F., *Optimal and reproducible surface-enhanced Raman scattering with precisely controlled nanoscale gaps*, Poster presented at: 7th International Conference on Metamaterials, Photonic Crystals and Plasmonsics 2016 Jul 25-28 Malaga